PHOSPHORUS-DEFECT INTERACTIONS DURING THERMAL ANNEALING OF ION IMPLANTED SILICON

By

PATRICK HENRY KEYS

A DISSERTATION PRESENTED TO THE GRADUATE SCHOOL
OF THE UNIVERSITY OF FLORIDA IN PARTIAL FULFILLMENT
OF THE REQUIREMENTS FOR THE DEGREE OF
DOCTOR OF PHILOSOPHY

UNIVERSITY OF FLORIDA

2001

ACKNOWLEDGMENTS

I wish to express my sincerest gratitude to my committee chairman, Prof. Kevin S. Jones, for his guidance, encouragement, and research expertise. I am also largely indebted to my committee cochairman, Prof. Mark E. Law, for his invaluable advice in the modeling and semiconductor processing fields. Without him, there would be no FLOOPS and no contract for this research. Together, Drs. Jones and Law display a synergy that makes being a student enjoyable and rewarding. In the SWAMP Center they have created a relaxed working environment that instills confidence in their students and allows one the freedom and flexibility to be creative. I could not have chosen a more appropriate research team to work in when I arrived at the University of Florida. I would also like to thank Profs. Abernathy, Nishida, and DeHoff for their participation on my supervisory committee.

This work was made possible by the financial support of the Semiconductor Research Corporation and the industrial support of several semiconductor manufacturers. I am especially indebted to Paul Packan and Eb Andiheh of Intel Corporation for providing the CVD grown boron spike material and performing several of the phosphorus implants. I would also like to thank Craig Jasper of Motorola and Lennie Rubin of Eaton for providing material and implants used in the well experiments. I am also indebted to Conor Rafferty and his fellow researchers at Lucent as well as Martin Giles and the TCAD Department at Intel for the invaluable experience I gained during my summer internships.

Of course, this work would not have been possible without the help of numerous people in the SWAMP Center, past and present. I would especially like to thank Viswanath Krishnamoorthy (a.k.a. Wish), Sushil Bharatan, and Rich Brindos for taking interest in my research and providing many useful discussions. My office mates Josh Glassberg, Heather Banisaukus, Erica Heitman, Mark Clark, Ibo, Ljubo, Chris Cramarce, Andres Geuteres, and Michelle Griglione also deserve a special thanks for making my time enjoyable and tolerating me for many hours on end.

I would like to thank Brent Gila and Jim "Hacksaw" Stevens for the extensive time and effort they put into fielding intramural flag football and softball teams. I thank my many teammates for the enjoyable hours of "noncompetitive" sports out on the playing field. Similarly, I must thank the Gator Athletic Association for filling the void of a full-blown sports junkie going through the withdrawals of leaving the New York sports scene.

Finally, I would be vastly incomplete without the love of my family and longtime friends, making this experience meaningless. I am truly indebted to my parents, brothers, sister, and their families. I could not have asked for a better environment to grow up in. It is amazing to know the strength a person can derive from the support of those who love him. This holds true for my many friends with whom I may be separated by distance but not in heart. Thanks to all the people I shared good times with in Ramsey, Scranton, and now Gainesville I have invaluable memories that will stay with me forever. I look forward to many more to come.

TABLE OF CONTENTS

page

LIST OF TABLES

LIST OF FIGURES

Abstract of Dissertation Presented to the Graduate School
of the University of Florida in Partial Fulfillment of the
Requirements for the Degree of Doctor of Philosophy

PHOSPHORUS-DEFECT INTERACTIONS DURING THERMAL ANNEALING OF ION IMPLANTED SILICON

By

Patrick Henry Keys

May, 2001

Chairman: Kevin S. Jones, Ph.D.
Cochairman: Mark E. Law, Ph.D.
Major Department: Department of Materials Science and Engineering

Ion implantation of dopant atoms into silicon generates nonequilibrium levels of crystal defects that can lead to the detrimental effects of transient enhanced diffusion (TED), incomplete dopant activation, and p-n junction leakage. In order to control these effects, it is vital to have a clear understanding of dopant-defect interactions and develop models that account for these interactions. This research focuses on experimentally investigating and modeling the clustering of phosphorus dopant atoms with silicon interstitials.

Damage recovery of 40keV Si^+ implants in phosphorus doped wells is experimentally analyzed. The effects of background phosphorus concentration, self-implant dose, and anneal temperature are investigated. Phosphorus concentrations ranging from $2.0x10^{17}$ to $4.0x10^{19}$ cm^{-3} and Si^+ doses ranging from $5.0x10^{13}$ cm^{-2} to $2.0x10^{14}$ cm^{-2} are studied during 650 - 800˚C anneals. A dramatic reduction in the

number of interstitials bound in {311} defects with increasing phosphorus background concentration is observed. It is suggested that the reduction of interstitials in {311} defects at high phosphorus concentrations is due to the formation of phosphorus-interstitial clusters (PICs). The critical concentration for clustering (approximately $1.0x10^{19}$ cm^{-3} at 750˚C) is strongly temperature dependent and in close agreement with the kink concentration of phosphorus diffusion.

Information gained from these "well experiments" is applied to the study of direct phosphorus implantation. An experimental study is conducted on 40keV phosphorus implanted to a dose of $1.0x10^{14}$ cm^{-2} during 650 - 800˚C anneals. Electrically inactive PICs are shown to form at concentrations below the solid solubility limit due to high interstitial supersaturations. Data useful for developing a model to accurately predict phosphorus diffusion under nonequilibrium conditions are extracted from the experimental results.

A cluster-mediated diffusion model is developed using the Florida Object Oriented Process Simulator (FLOOPS). The nucleation of defects is controlled by the diffusion-limited competition for excess interstitials between PICs and {311} clusters. The release of interstitials is driven by cluster dissolution. Modeling results show a strong correlation to those experimentally observed over a wide temporal and thermal domain using a single set of parameters. Improvements in process simulator accuracy are demonstrated with respect to dopant activation, TED, and dose loss.

CHAPTER 1
MOTIVATION

This thesis examines the interactions between phosphorus dopant atoms and silicon interstitial defects during the annealing of nonamorphizing ion implants. In this chapter, the motivation for studying and modeling the interaction will be given, and the scope and organization of this thesis will be presented.

Semiconductor Devices and the MOSFET

Since the 1960's, the semiconductor industry has been rapidly growing at an astonishing economic rate. For the most part, this juggernaut has relied on solid-state transistor devices, such as the Metal-Oxide-Semiconductor Field Effect Transistor (MOSFET). Reduction of the physical device dimensions can vastly improve performance and increase computational ability. The planar MOSFET as shown in Figure 1 has proven to be a robust design, capable of scaling to submicron dimensions.

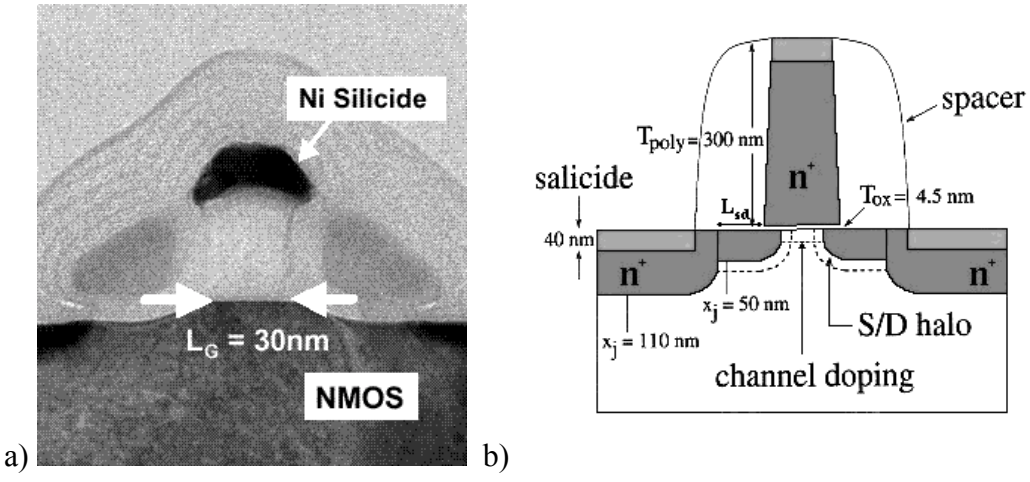

Figure 1. Cross sections of submicron n-channel MOSFETs: a) TEM of 30nm research-grade transistor [Cha00], b) schematic of "well tempered" NMOS shows doping [Ant99].

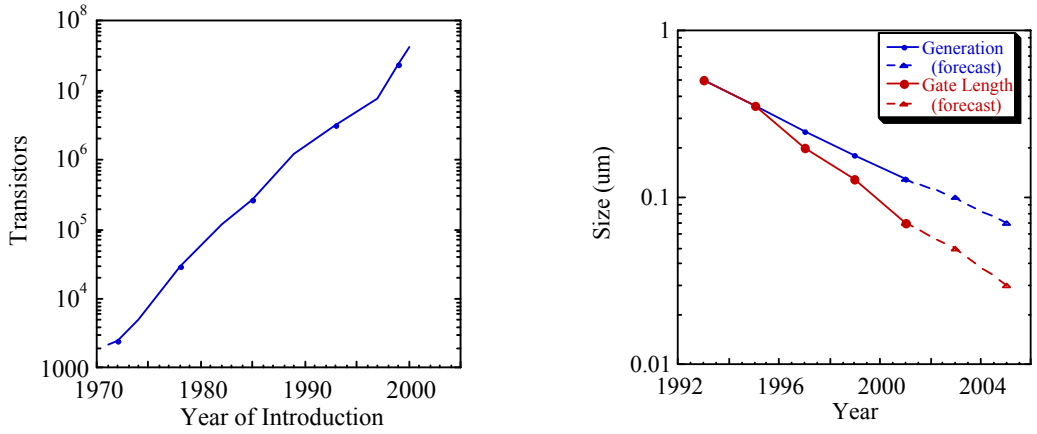

a) b)

Figure 2. Moore's law describes transistor scaling trend over the years: a) transistors per chip, b) feature size

The scaling trend is most commonly put into context using Moore's law (the silicon industry learns how to reduce the size of a transistor on a silicon chip by a factor of two every three years or fewer) [Moo65, Moo75], graphically represented in Figure 2. This has been driven by the computational demand for high speed and low power microprocessors. However, the benefits of device scaling come at the cost of increased processing complexity.

Junction Engineering

State-of-the-art integrated circuits are fabricated through the repeated use of a sequence of physical processes that consist of (1) growing, depositing, patterning and etching a variety of materials; (2) implanting desirable chemical species to serve as electrical donors or acceptors; and (3) thermal annealing in a variety of ambient environments. The electrical behavior of the resulting devices is highly dependent on the

quality and thickness of the deposited or grown materials, the quality of the silicon which has been processed, and the location and concentration of the dopant atoms in the silicon crystal lattice. Introduction of dopants (arsenic or phosphorus for n-type doping and boron for p-type doping) through the use of ion implantation has proven to be an extremely viable method of creating doped semiconductor regions such as the MOSFET source, channel and drain. This non-conservative processing step has the unfortunate disadvantage of disrupting the equilibrium crystalline order of the silicon, necessitating the use of subsequent thermal processing to restore crystallinity and enable dopants to occupy electrically active lattice sites. Reactions that occur during the post-implant anneal step make the formation of shallow junctions a difficult task.

The use of shallow junctions and well engineering to improve short channel effects is clearly exemplified in Figure 3. As gate length (L_{gate}) is scaled, off-state leakage current increases due to the lateral encroachment of the depletion region. By

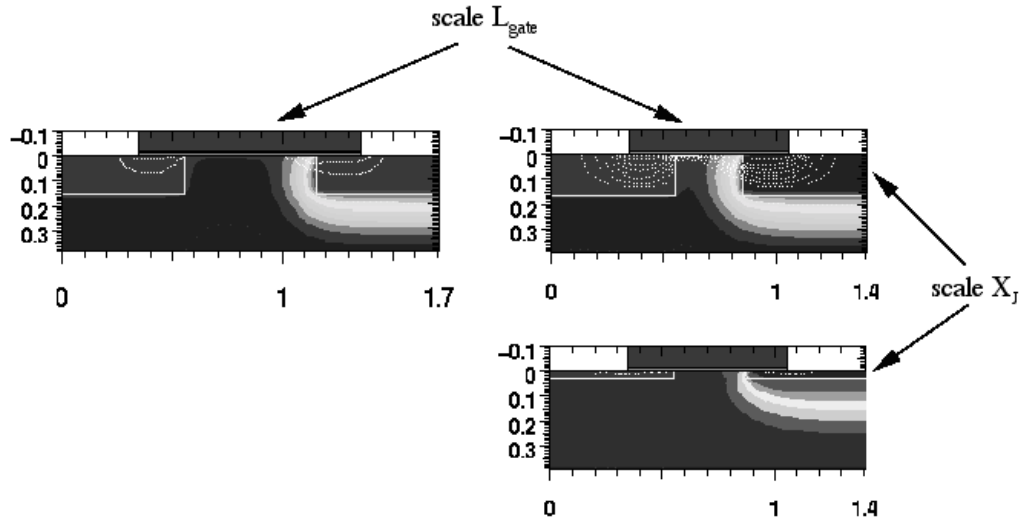

Figure 3. Simulated MOSFET device showing effect of scaling gate length (L_{gate}) on the depletion region. Junction depth (X_J) is scaled to reduce lateral encroachment of depletion region; source/drain doping is increased to reduce resistances

scaling junction depths (X_J), charge sharing is reduced resulting in improved off-state characteristics. At the same time, the source / drain extension (SDE) doping must be increased to minimize resistances. Figure 4 shows the attainable sheet resistances (R_s) as a function of X_J and the requirements for future MOSFET generations prescribed in the International Technology Roadmap for Semiconductors (ITRS) [SIA00].

Dopant activation, enhanced diffusion, and extended defect formation represent critical issues which are gaining significant importance as factors that may limit junction scaling [SIA00]. For example, incomplete dopant activation results in higher than expected source and drain resistances. Enhanced diffusion can cause dopants from the source and drain to redistribute underneath the gate. This moves the position of the

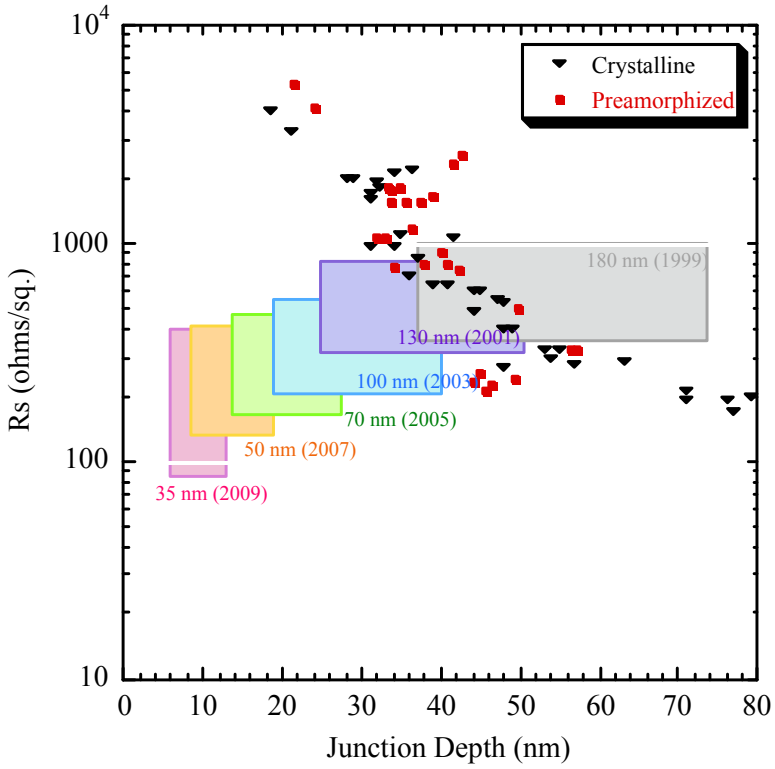

Figure 4. Sheet resistance vs. junction depth projections from SIA roadmap and experimentally reported values.

electrical junction and limits the minimum size of the transistor that can be fabricated. Extended defects can getter metal impurities and introduce scattering sights, reducing carrier mobility if located entirely within the same electrical region [Buc72], or can lead to current leakage if located in the space charge region of a p-n junction [Ash77, Bul79]. Due to the inherent complexity of the implant damage recovery process, the current understanding of these physical processes is incomplete. As will be shown, it is clear that all three of these issues are strongly affected by the interaction of dopant atoms and point defects created during the implantation process.

Processing Physics

As the electrical properties of integrated circuits are defined by the dimensions, concentrations, and junctions of doped regions created during "front-end" processing, it is vital to have a clear understanding of how processing conditions affect the material parameters and doping profiles. Processing physics is the study, understanding, and modeling of the complex chemical, physical, mechanical, optical, and electrical processes which are required for the fabrication of semiconductor devices.

Empirical Modeling

Process simulation is used to shorten the development cycle of new technology generations, improve existing processes, and to identify future technology roadblocks. Because of the high cost of fabrication, a simulation tool which reduces the number of experimental iterations required to perfect the fabrication process is extremely valuable. If the physics of a certain processing step is not intrinsically understood, empirical and phenomenological modeling is unavoidable and often produces satisfactory results in a limited range. These models are only accurate as long as the processing sequence which

is being simulated is very similar to the experiments on which the model was based. However, empirical models usually require less computing power and result in faster simulation times due to the reduced complexity.

Physics-Based Modeling

A second category of programs attempts to use the underlying physics as a basis for the simulations. By relying on physically based models, the simulator is better equipped to investigate processing variations that are outside the range of experimental observation. It is hoped that the models which are based on the underlying physics of the various processes can be used to predict the results of new and untried process sequences. In addition to accurately designing next generation devices, this provides the means to prophesize processing limitations which may introduce future technology roadblocks, such as gate dielectric thickness, threshold voltage control, device isolation, and shallow junction formation.

Scope and Organization

This research investigates the interaction of phosphorus dopant atoms with silicon interstitials through experimental observation and computer simulation. Experimental data indicating the preferred thermodynamic equilibrium states and the dominant reaction kinetics are extracted for use in simulations. Results are analyzed using FLOOPS to correlate with physical-based diffusion models. In doing so, FLOOPS is used as a tool to identify the physical origins of the observed phenomena and improvements to the models are incorporated when necessary.

This work is divided into separate and distinct experimental investigations and Technology Computer Aided Design (TCAD) modeling chapters. Chapter 3 consists of

experimental investigations focusing on the effect of silicon implant damage recovery in a phosphorus-doped background. Chapter 4 is an experimental investigation of defects and diffusion resulting from direct phosphorus implants. Chapter 5 describes the Si cluster mediated diffusion models used and the dose loss and PIC models developed based on the experimental observations. Chapter 6 provides a concluding discussion addressing significant results with respect to the current understanding of ion implantation technologies and presents potential areas of future study.

CHAPTER 2
BACKGROUND AND RESEARCH FOCUS

In this chapter, the influence of interstitial defects on TED, dose loss and dopant clustering will be reviewed. First equilibrium point defects and diffusion will be discussed. Next, studies in primary implant damage and the resulting secondary defects will be revisited. Research by other investigators linking the secondary defects to TED and dopant clustering will be reviewed. Finally, the research approach used to experimentally study and model phosphorus-defect interactions will be introduced.

Equilibrium Point Defects and Diffusion

Point defects in crystalline materials are imperfections that involve a few atoms at most. They occur in all classes of materials and can have a profound impact on the material's properties. Atoms missing from normally occupied lattice sites are vacancies, while host atoms located anywhere in a crystal except at a lattice site are interstitials. Impurities are atoms of a different atomic number than those atoms composing the system. Impurities can be introduced intentionally (dopants) or can unintentionally be incorporated (contaminants) during processing.

The Gibb's free energy, G, is a balance between two factors, enthalpy (internal energy) and entropy (a measure of statistical randomness). G increases with either an increase in internal energy or a decrease in entropy. The atomic configuration that results in a minimization of G is the thermodynamically favored state. All point defects move atoms in their immediate vicinity from their equilibrium positions, increasing the internal energy of the crystal due to changes in bond lengths (strain energy). However, this is

balanced by the decrease in free energy associated with the increased entropy of a crystal with point defects present. Thus, thermodynamic arguments mandate the presence of point defects and suggest that it is impossible to create a stable crystal without them.

The equilibrium concentrations of point defects in semiconductors are thermodynamically defined functions of temperature, their respective concentrations being proportional to $\exp(-W/k_BT)$, where W is the defect formation energy. These equilibrium concentrations can also be affected by other factors such as stress, impurity trapping, electron concentration, and material processing history. Direct measurement of the equilibrium point defect populations and their migration parameters is not possible. Defect parameters can be estimated from ab-initio calculations or by studying diffusion behaviors [Fra84, Hu97, Tan85, Wat97, Zhu97]. Surface and bulk processes used to make IC's can have a dramatic effect on the point defect populations leading to nonequilibrium concentrations as will be described shortly. During thermal processing, point defects influence dopant diffusion, redistribution of the dopant atoms in the silicon lattice through the process of mass transport along a concentration gradient.

Fickian Diffusion

In its simplest form, the diffusion process can be described on a macroscopic level using Fick's Laws. Fick's first law states that the mass flux per unit area of a diffusing species under steady state conditions is proportional to the concentration gradient, mathematically given as

$$J = -D\left(\frac{\partial C(x)}{\partial x}\right)_t \qquad (1)$$

J is the flux [atoms/(cm^2 sec)], D is an Arrhenius constant called the diffusion coefficient (cm^2/sec), C is the concentration of the diffusing species (atoms/cm^3), x is the gradient

direction, and t is time. This can be extended using Fick's second law to describe a system in which C is time dependent,

$$\frac{\partial C(x,t)}{\partial t} = \frac{\partial}{\partial x}\left(D\frac{\partial C(x,t)}{\partial x}\right) = D\frac{\partial^2 C(x,t)}{\partial x^2} \qquad (2)$$

assuming that D is independent of time and space. D is macroscopically modeled using the Arrhenius equation (see Appendix A)

$$D(T) = D_0 e^{\left(-E_A/kT\right)} \ [\mathrm{cm}^2/\mathrm{sec}] \qquad (3)$$

where T is the temperature (˚K), D_0 is the pre-exponential constant (same units as D), k is the Boltzmann constant ($8.617\text{x}10^{-5}$ eV/˚K) , and E_A is the activation energy (in eV) for the diffusing species. Diffusivities calculated in this simple manner have been shown to match experimental measurements best when the dopant concentration is low.

Concentration Dependent Diffusion

The previous model is valid if the diffusivity is constant at a given temperature. This situation works when the doping concentration is lower than the intrinsic carrier concentration, n_i, at the diffusion temperature approximated by the equation [Mor54]

$$n_i \approx 3.87\times 10^{16} T^{3/2} e^{\left(-0.605+\Delta E_g/kT\right)} \ [\mathrm{cm}^{-3}] \qquad (4)$$

where ΔE_g is the energy-gap lowering. It is observed that under conditions of high dopant concentration, D becomes a function of concentration, $D=D(C,T)$. When the total impurity concentration (diffusion plus substrate background) exceeds n_i the extrinsic diffusion coefficient, D_E, can be used. D_E depends on the ratio of the extrinsic to intrinsic carrier concentrations (n/n_i) and is attributed to different charge states of the diffusing species

$$D_E = D_i + D^-\left(\frac{n}{n_i}\right) + D^{2-}\left(\frac{n}{n_i}\right)^2 + D^+\left(\frac{p}{n_i}\right) \qquad (5)$$

Table 1. Concentration dependent diffusivity parameters used in FLOOPS

Dopant	$D_0^=$ (cm^2/sec)	$E_A^=$ (eV)	D_0^- (cm^2/sec)	E_A^- (eV)	D_{i0} (cm^2/sec)	E_{iA} (eV)	D_0^+ (cm^2/sec)	E_A^+ (eV)
As			12.8	4.08	0.066	3.45		
B					0.929	3.56	0.771	3.56
P	0.0245	3.23	6.38	4.05	5.6	3.71		
Sb			15.0	4.08	0.214	3.65		

where each diffusivity component has a pre-exponential factor and activation energy of diffusion such that

$$D_i = D_{i0} e^{\left(-E_{A_i}/kT\right)} \ [\mathrm{cm}^2/\mathrm{sec}] \qquad (6)$$

Concentration dependent diffusivities lead to faster diffusion at higher concentrations, thus resulting in more abrupt, box-like profiles. Default pre-exponential and energy values of common dopants used in FLOOPS are given in Table 1.

Atomistic Diffusion

Experimental studies found that these phenomenological models for diffusion were inadequate for explaining the diffusion behavior of dopants in silicon under varying processing environments, such as oxidation [Dob71, Mas73] and ion implantation [Mic89]. This is because Fickian diffusion considers only the temperature dependence of the diffusivity and not the dependence of diffusivity on point defect populations. Physically, atoms can migrate through covalently bonded silicon via interaction with self-interstitials, and vacancies [Nic89]. Vacancy-assisted diffusion occurs when a substitutional dopant atom exchanges position with a nearest neighbor lattice site that is vacant. Interstitially-assisted diffusion can occur by two mechanisms, kick-out and interstitialcy exchange. The interstitial kick-out mechanism occurs when a substitutional dopant atom is replaced by a self-interstitial and diffuses as a pure interstitial before returning to a substitutional site either by reverse kick-out or by recombination with a

vacancy. The interstitialcy mechanism occurs when a dopant and a self-interstitial occupy a single lattice site, forming a pair. In this case the dopant diffuses by translating positions with nearest neighbors through bond exchange without displacing the silicon atoms from their lattice sites. Usually, no distinction is made between the interstitial kick-out mechanism and the interstitialcy mechanism as they are both mathematically equivalent.

The interaction of the vacancy and interstitial defects with dopant atoms determines the dopant diffusivities. The point defect interactions with dopant atoms may be represented by chemical reactions of the following type:

$$A + X \Leftrightarrow A_X \tag{7}$$

where A is the dopant atom in the immobile substitutional site, X is the point defect, and A_X is the mobile dopant species. Ignoring charge states for the moment, the concentrations of dopants and defects can be accounted for by using a set of continuity equations

$$\frac{\partial C_A}{\partial t} = R(C_A, C_I) + R(C_A, C_V) \tag{8}$$

$$\frac{\partial C_{A_X}}{\partial t} = \nabla d_{A_X} \nabla C_{A_X} - R(C_A, C_X) \tag{9}$$

$$\frac{\partial C_X}{\partial t} = \nabla d_X \nabla C_X + R(C_A, C_X) \tag{10}$$

where d is diffusivity, and R represents reactions of dopants and defects such as recombination and precipitation. This is commonly referred to as a five stream diffusion model as it results in a total of five equations, including two for each defect type (I and V), and could be expanded to incorporate higher order complexes, and reactions.

Additionally, this set of equations can be expanded to account for differences in the charge states of each species, leading to added complexity.

The atomistic diffusivity is often expressed as

$$D_A = \left(D_{AI} + D_{AV}\right)\left(f_i \frac{C_I}{C_I^*} + \left(1 - f_i\right)\frac{C_V}{C_V^*} \right) \ [\mathrm{cm}^2/\mathrm{sec}] \qquad (11)$$

where, D_{AI} and D_{AV} are the interstitial and vacancy related diffusivity components, C_I, C_I^*, C_V, and C_V^* are the interstitial, equilibrium interstitial, vacancy, and equilibrium vacancy concentrations, respectively. f_i is a measure of the fraction of interstitialcy diffusion exhibited by that particular diffusing species, (f_i =1.0 for P, f_i ≈0.9 for B, f_i ≈0.5 for As, and f_i =0.0 for Sb) [Hu97]. In this case the diffusivity is affected by nonequilibrium concentrations of point defects, weighted by the preferred diffusion mechanism of the dopant. Due to complexity, atomistic diffusion models are often solved for using computer programs capable of converging partial differential equations.

Diffusion in FLOOPS

The Florida Object Oriented Process Simulator (FLOOPS) has been developed to model important physical processes such as thermal oxidation of silicon and dopant diffusion using physically-based models [Law96a]. Results from process simulators can be input to device simulators such as PISCES and FLOODS. FLOOPS uses local point defect concentrations to determine dopant diffusivities. In order to keep track of the spatial distribution of point defects, FLOOPS solves the diffusion equations for dopant atoms as well as the equivalent equations for point defects. Since vacancies and interstitials can interact, the equations describing their motion are coupled. The Alagator commands allow the user to control and set up scripts for creating models for diffusion. This is utilized to model the observed cluster reactions.

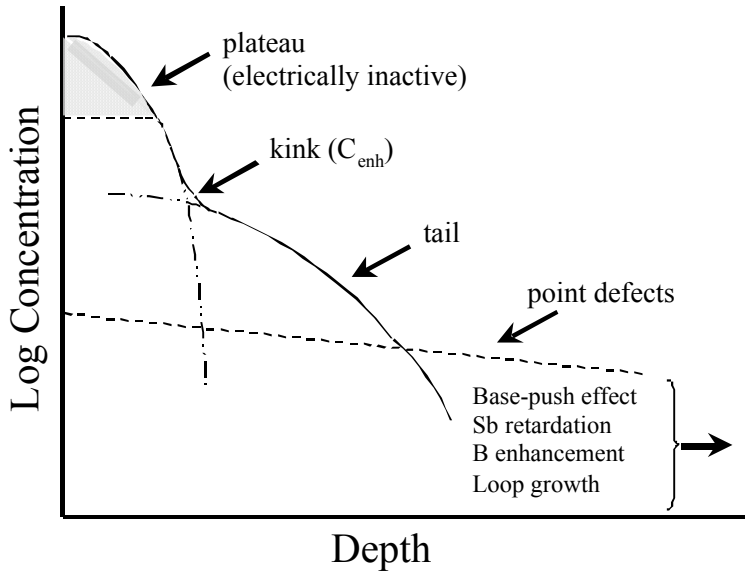

Figure 5. Anomalous phosphorus diffusion displays a characteristic "kink and tail" profile.

Anomalous Dopant Diffusion

In addition to the previously described diffusion models, some dopants display anomalous diffusion characteristics. Under certain conditions, phosphorus has been shown to exhibit a "kink and tail," characterized by a plateau region near the surface followed by an inflection and a gradually sloped tail. This is schematically represented in Figure 5. Experiments on high surface concentration phosphorus and boron diffusions in silicon show an enhanced diffusivity in the tail region [Sch72, Fai77]. This phenomenon is very pronounced in the case of phosphorus, but is somewhat less pronounced in the case of boron. The electrically inactive plateau region near the surface has been attributed to SiP precipitation [Mas77], usually occuring at relatively high phosphorus concentrations (3.5×10^{20} cm^{-3} at 1000˚C).

Figure 6 is a plot of the phosphorus kink concentration gathered from several different experimental studies [Sch72, Mas77, Oeh84, Ang87, and Fai90]. These studies include solid source in-diffusion, ion implantation, oxidation enhanced diffusion, and

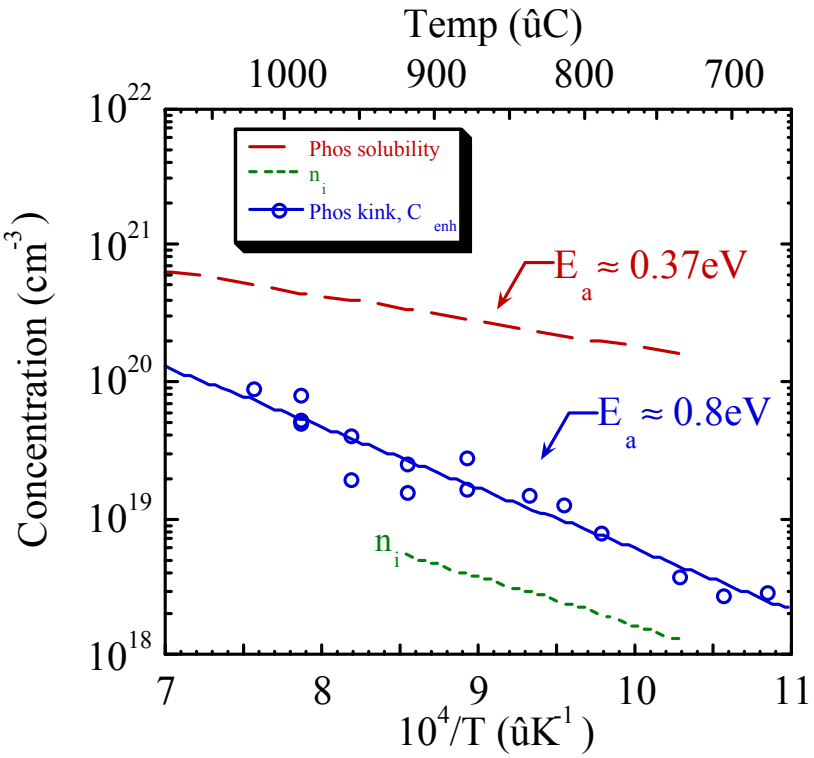

Figure 6. Phosphorus kink concentration reported by various researchers over a wide temperature range [Sch72, Mas77, Oeh84, Ang87, and Fai90].

include both RTA and furnace anneals. The concentration at which the kink occurs is independent of processing methods, only being influenced by processing temperature. This demonstrates that the kink behavior is an intrinsic property of the material system. The deviation in data at higher temperatures is slightly larger than at lower temperatures due to issues related to processing time and temperature control. A best fit to the data is obtained using the Arrhenius formula (see Appendix A)

$$C_{enh} = 1.65 \times 10^{23} e^{\left(\frac{-E_A}{k_B T}\right)} \ [\text{cm}^{-3}] \qquad (12)$$

where k_B is the Boltzmann constant (8.617x10^{-5} eV/°K) and E_A = 0.88 eV. The phosphorus solubility [Nob82, Sol98] and the intrinsic carrier concentration, n_I, [Mor54] are also plotted for comparison.

Several models have been proposed to explain the anomalous diffusion of phosphorus in silicon. Some of the early phosphorus diffusion models in silicon were based on the formation of phosphorus-vacancy pairs or E-centers and included a quasivacancy formation energy [Fai77, Yos79]. This contradicts experimental results showing phosphorus motion occurs predominantly by interstitial diffusion [Har83, Nis86]. Mathiot and Pfister [Mat84] proposed a percolation model, and Dunham [Dun92] assumed that the pair diffusivity depends on the square of the active donor density. Uematsu [Uem97] attributes the kink and tail profiles to a changeover from the vacancy contribution to the kick-out contribution. Without further experimental evidence, the true origin of anomalous kink and tail diffusion is still the subject of debate.

Ion Implant Damage

The use of ion beams to modify selected materials has become a commonly used technique to alter a material's properties, whether it involves the removal (etching) of material or addition (implantation) of material. Theoretical and experimental observations of the penetration and stopping of energetic ions in matter have existed for nearly a hundred years, tracing back to the likes of Curie, Bohr, J. J. Thompson, and Rutherford [Cur00, Tho12, Boh13, Rut11]. In 1952, Ohl at Bell Laboratories first discovered the usefulness of ion implantation in semiconductors by irradiated point contact diodes with helium, achieving a reduction of the reverse current [Ohl52]. Soon after, the use of ion implantation as a technique to dope semiconductors was patented [Sho54], in which it was pointed out that subsequent annealing is necessary for recrystallization of the semiconductor lattice. Ion implantation is now a widely developed processing step used repeatedly in the fabrication of a single integrated circuit. It is commonly used during CMOS transistor processing of the poly gate, SDE, LDD,

source, drain, threshold adjust, HALO, tub formation, anti-punchthrough, and retrograde well formation. It also has many miscellaneous uses such as backside damage generation (gettering), enhanced etching (damage SiO_2 and Si_3N_4), photoresist hardening to improve etch resistance, buried insulator formation (SIMOX), and ion beam mixing (silicidation reactions).

Primary and Secondary Damage

Damage due to ion implantation can be separated into two distinct categories: primary damage occurring from bombardment of the implanted ions and secondary damage which results in extended defects during subsequent thermal processing. During ion implantation, energetic ions come to rest in the target material through energy transfer via electronic screening and nuclear collisions. Lattice displacements occur when the energy transferred during nuclear collisions exceeds the displacement energy, approximately 15 eV for Si. Displacements can be due to the implanted ion as well as recoils, resulting in a damage cascade in the form of interstitial and vacancy point defects. For every interstitial created from a displacement, an equivalent vacancy is created. This creation of an interstitial and vacancy is referred to as a Frenkel pair. Similarly, a vacancy and interstitial can migrate and combine, annihilating each other. This is referred to as I-V recombination. Not all Frenkel pairs will recombine during the implant process, thus resulting in primary implant damage. If a significant damage density occurs (i.e. – due to heavy mass ions or large doses) portions of the material can be amorphized as shown in Figure 7. As a rule of thumb, amorphization occurs when the damage density exceeds approximately 10% of the lattice density (damage density $\approx 5.0 \times 10^{21}$ cm^{-3} for Si). Thus, heavier ions tend to amorphize the target more easily, requiring lower doses to reach the amorphization threshold.

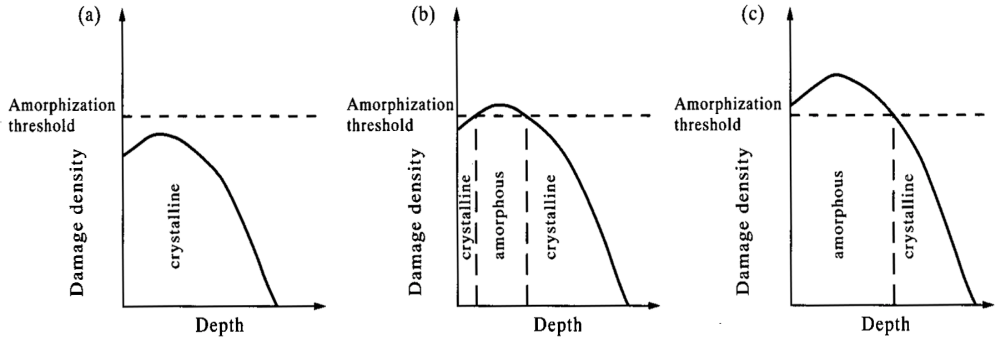

Figure 7. Primary implant damage: (a) no amorphous layer formed, (b) buried amorphous layer, (c) amorphous layer extends to the surface.

Post-ion implantation annealing is required to restore crystallinity and enable the dopants to occupy electrically active sights. This thermal processing results in the recombination of interstitial and vacancy point defects, and the formation of extended defects. The morphology of the resulting extended defects, or secondary damage, is dependent upon the primary damage origin as classified in Table 2 [Jon88]. This study will pertain strictly to nonamorphizing implants, focusing largely on subthreshold Type-I defects.

The primary, and consequently the secondary, damage is strongly influenced by the mass of the implanted ion. This is evident in Figure 8, which shows the doses necessary for defect formation as a function of ion mass [Jon89]. These values are for a 900°C annealing process. Significant doses of lighter ions such as boron, silicon, and phosphorus can be implanted without reaching the amorphization threshold. Heavier ions such as arsenic amorphize at lower doses. Thus, lighter ions can result in Type-I defects, whereas identical implant conditions for heavier ions will result in end-of-range or Type-II defects.

Table 2. Classification of extended defects from ion implantation

	As-implanted condition	Extended defects after annealing	Possible reason for defects
Type I (subthreshold)	Damaged above a critical dose but not amorphized	Dislocation loops Voids Stacking fault tetrahedra located near the projected range or the surface	Inability of all vacancies and interstitials to recombine and injection of extra atoms into the lattice
Type II (end of range)	Amorphous layer formed either buried or continuous to the surface	Band of dislocation loops located below the amorphous-crystalline interface (end of range)	Recoil of extra atoms from the amorphous layer and/or injection of extra implanted atoms beyond the amorphous layer
Type III (regrowth related)	Amorphous layer formed, either buried or continuous to the surface	Stacking faults Microtwins Hairpin dislocations located in the recrystallized layer	Poor recrystallization of the amorphous layer (i.e., (111) silicon, strained SiGe alloys or compound semiconductors)
Type IV (clamshell or zipper)	Buried amorphous layer formed	Dislocation loops located at the interface where the two recrystallizing interfaces meet	Lack of perfect coherency when the two regrowing amorphous-crystalline interfaces meet
Type VI (solubility related)	Crystalline or amorphous	Precipitates Dislocation loops Half loop dislocations located around the ion projected range	Exceeding the solid solubility of the impurity, also defects from point defects generated by the precipitation process

Source [Jon89]

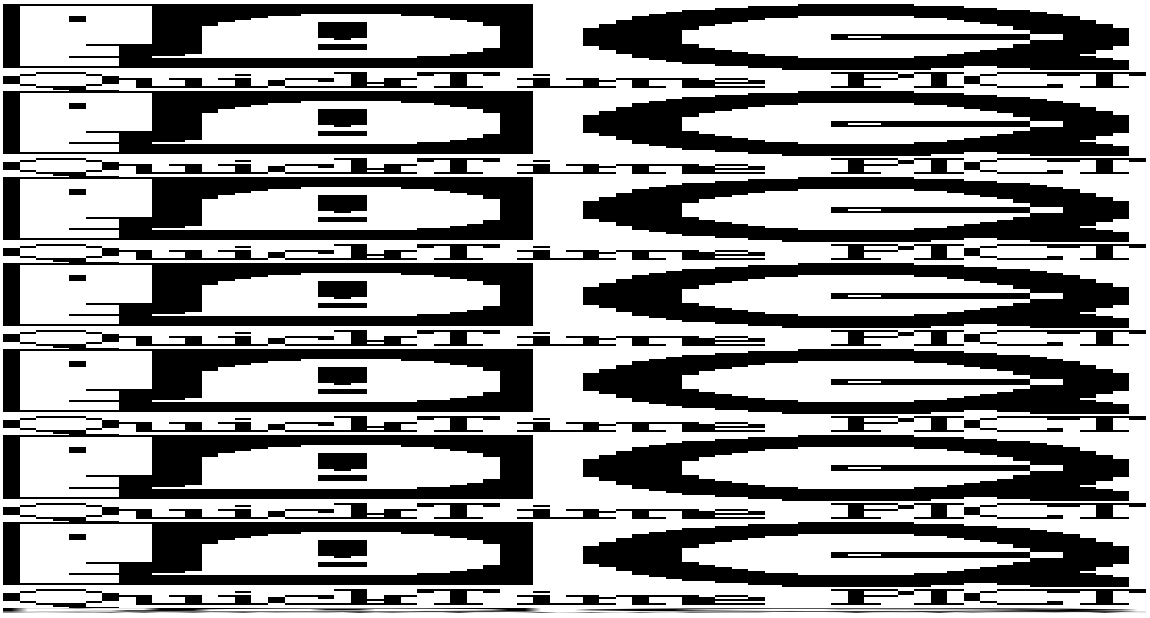

Figure 8. Threshold doses for secondary defect formation of 20-200keV implants and 900˚C anneal [Jon89].

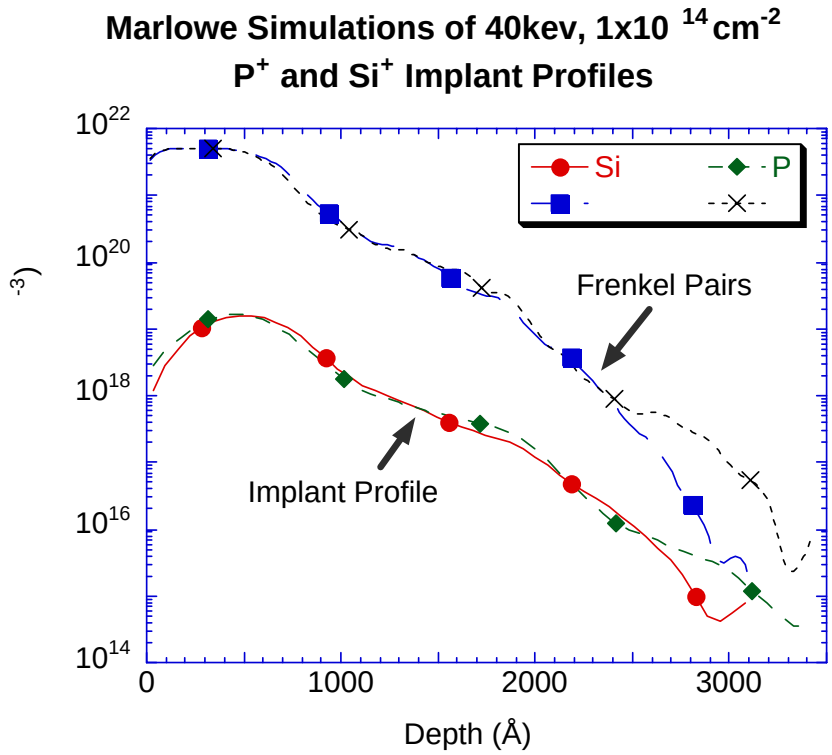

Figure 9. Comparison of primary damage distribution for identical silicon and phosphorus implants simulated with UTMARLOWE.

Due to the similar ion masses of silicon and phosphorus, the primary damage cascades created by each species are expected to be very similar. Damage profiles simulated using the Monte Carlo based software, UTMARLOWE [Tas89, Mor95], for a silicon and a phosphorus implant of identical conditions are shown in Figure 9. These simulations are for 40keV implants to a dose of $1.0x10^{14}$ cm^{-2}. The resulting ion and damage profiles for each species closely overlap. This eliminates the primary implant damage profile as a possible cause for differences when comparing the secondary defects that result from Si and P. Thus, any significant differences after annealing can be attributed to the interaction of phosphorus dopant atoms with point defects.

Type-I Defects: Si Implants

Secondary defects will form after Si implantation if the dose exceeds a critical value, typically around $5.0x10^{12}$ cm^{-2} for energies between 20-200 keV [Jon88, Eag95]. These Type-I defects will be in the form of rod-like defects, called {311} defects, centered at a depth corresponding to the projected range, R_P. {311} defects are extrinsic rows of interstitials lying on the {311} habit plane, elongated in the <110> direction [Bou87, Tak91]. The arrangement is predicted by energetic reduction of dangling bonds [Tan81]. Methods have been developed to quantify the number of interstitials contained within the {311} defects [Eag94, Bha97]. The defect density and quantity of interstitials bound in {311} defects has been shown to increase linearly with implant dose. Based on the dissolution decay rate, the evaporation of {311} defects during annealing between 670˚C to 815˚C follows an activation energy reported to be approximately 3.6 eV [Eag95].

With increasing Si implant dose, Type-I dislocation loops form in addition to {311} defects. The threshold dose for loop formation appears to be greater than $1.0x10^{14}$

cm^{-2}. Generally, they are a/2<110> dislocation loops lying on {111} habit planes. These loops are more stable than {311} defects and have proven to be difficult to dissolve even at temperatures above 900˚C.

Type-I Defects: P Implants

Phosphorus implantation has been shown to result in the formation of dotted defects, rodlike defects, and dislocation loops [Tam73]. Table 3 shows the secondary defects resulting from phosphorus implant conditions that will be of interest to the experimental study [Des97]. "Loops" refers to what were believed to be small a/2 <110> dislocation loops, sometimes referred to as "dotted defects". The appearance of non

Table 3. Extended defect formation from phosphorus implants (Anneal 750˚C, 5 minutes)

		Implant Energy			
		10 keV (R_P=175Å)	30 keV (R_P=455Å)	50 keV (R_P=720Å)	100 keV (R_P=1440Å)
Dose (cm^{-2})	$2.0x10^{13}$	None	None	None	Loops
	$5.0x10^{13}$	None	None	Loops	Loops & {311}
	$1.0x10^{14}$	None	Loops	Loops & {311}	Loops & {311}
	$2.0x10^{14}$	Loops	Loops	Loops & {311}	Loops & {311}

Source [Des97]

{311} defects has been shown to occur under the same conditions that would normally produce {311} defects by identical implantation with silicon. Annealing of phosphorus implants often results in a higher density of smaller defects than silicon implants. This will be further evidenced in the experimental results presented later.

Transient Enhanced Diffusion

A different form of anomalous diffusion is related specifically to the ion implantation process. The excess point defects resulting from implantation increase C_i during the initial stages of the subsequent anneal. This in turn causes an initial period of much faster diffusion (>1000 fold), known as transient enhanced diffusion. The transient period can vary from a few seconds at about 950˚C to several hundred hours at around 650˚C, and the dopant profile moves substantially during this period, resulting in drastic changes of junction depths and abruptness (or lack thereof) [Mic89, Pac90]. Numerous experimental investigations have been conducted to gain a thorough understanding of this behavior.

Recent TED Studies

Over the past decade, experimental research utilizing near-surface silicon implantation spatially separated from underlying boron-doped markers has provided detailed understanding of transient enhanced diffusion (TED) [Pac91, Sto97]. It is now commonly believed that the interstitial point defects generated during the ion implantation process agglomerate into extended defects, maintaining a supersaturation of interstitials which enhance diffusion of dopants such as boron, phosphorus and, to a lesser extent, arsenic. This is supported by experimental diffusion studies coupled with developments in quantitative transmission electron microscopy (QTEM).

It has been shown that there is a strong correlation between the thermal dependence of {311} defect dissolution observed by QTEM and diffusivity enhancements in neighboring boron-doped markers [Eag95, Eag94]. As the {311} defects are condensates of silicon interstitials, they act as storage sites that gradually release interstitials. The enhancement in diffusion of neighboring boron marker layers

coincides with the {311} dissolution process [Eag95]. Furthermore, the Si interstitial release process can be simulated using a first order cluster kinetics model [Raf96].

However, a clear understanding of the complex interactions between point defects and the dopant atoms is still lacking, especially when both are located in the same geometrical regions, i.e., – not spatially separated, as is the case for dopant ion implantation. Often the introduction of dopants causes a change in defect morphology, sometimes leading to the complete disappearance of defects, while TED is still observable [Zha95, Hay96, Li99]. Understanding the formation, agglomeration, and dissolution of point defect / dopant complexes is clearly a fundamental challenge to the use of ion implantation in future Si technologies.

Dopant Clustering

Annealing of shallow boron implants into crystalline silicon can form immobile portions of the dopant profile that are electrically inactive [Cow90, Sto95]. It is believed that the high levels of interstitial supersaturation induce clustering of substitutional boron at concentrations below the solid solubility limit of boron in silicon. These clusters cannot be detected using TEM [Sto95, Zha95], leading one to believe that they contain only a few atoms (<1000 atoms). Monte Carlo simulators have been utilized to explain the clustering behavior using values derived from both phenomenological fits [Pel97, Pel99] and *ab initio* calculations [Cat98, Len00]. Boron clustering has also been modeled using continuum process simulators [Lil97, Uem98], demonstrating improvements in accuracy.

Although significant experimental data of similar phosphorus clustering is lacking, it has been suggested that phosphorus diffusion simulations can also be improved through the incorporation of phosphorus clusters [Sch99, Uem99]. This model

assumes an initial portion of phosphorus is clustered prior to annealing. During annealing, phosphorus interstitials are released upon cluster dissolution based on empirical fit. Additionally, the interaction between phosphorus clusters and silicon interstitials is neglected.

Dopant of Study: Phosphorus

The common silicon dopants are boron (p-type), arsenic (n-type) and phosphorus (n-type). A vast amount of research has been focused on studying boron as it is the only p-type dopant. Compared to the silicon target atoms, arsenic is a relatively heavy ion, often resulting in amorphization during implantation. Arsenic also can come out of solution and electrically deactivates during lower temperature processing. The usage of phosphorus has gradually been getting phased out due to its higher diffusivity and deeper junction depths than arsenic. However, it has a high solubility limit and can be used to form reliable junctions. Understanding its diffusion characteristics under nonequilibrium conditions is of significant importance.

Phosphorus is very close in mass to silicon, thus resulting in almost identical primary implant damage profiles. Also, phosphorus can be implanted up to doses of approximately 5.0×10^{14} cm^{-2} without amorphizing the silicon. For these reasons, the resulting annealing characteristics can be compared directly to those of silicon implants. The use of Si implants to create defects provides a good reference that the effects of different phosphorus implant conditions can be compared to.

When silicon implants were used to study TED, the interstitials were spatially separated from the diffusing dopants and did not interact in the implant-damaged region [Pac90, Eag95]. It still remains unclear how interstitials behave when located in the same region of the dopant atoms, as would be the case for any dopant implant. The influence

of dopants will become increasingly important as the technological trend is towards shallower implants with higher peak concentrations.

Counting the number of trapped interstitials incorporated in extended defects and tracking the release of interstitials has proven to be a tool useful towards gathering information about interstitially assisted diffusion processes. Similar experimental methods can be used to expand our understanding of the mechanisms influencing TED, such as dopant-defect interactions in the implant-damaged region. The subsequent studies will investigate the influence and interaction of phosphorus dopant atoms with silicon interstitials and the resulting effects on TED. Phosphorus is chosen as the dopant for the following reasons:

1. The primary implant damage created by phosphorus and silicon is almost identical as both species have very similar atomic masses. This simplifies comparison of the two species without disruption due to different primary implant damage profiles.

2. Phosphorus exhibits a high fractional interstitial diffusivity component, f_i=1, so it exhibits large diffusion enhancements during interstitial supersaturation.

3. Phosphorus displays many interesting anomalous diffusion characteristics, many of which the physical origins are still not fully understood. Results from this research will aid in further understanding these anomalies.

This research investigates the interaction of phosphorus and silicon atoms during post-ion implantation annealing. It can be expected that phosphorus and silicon interstitials strongly compete for excess free interstitials during the initial phase of ion implant damage recovery, resulting in the formation of phosphorus interstitial clusters (PICs). This expectation is based on the behavior of other dopants and seems reasonable due the high affinity for interstitials that is demonstrated by phosphorus diffusion (f_i=1).

It is expected that this competition will reduce the number of interstitials bound in metastable {311} storage sites, thus altering the transient enhanced diffusion resulting from phosphorus implants as compared to silicon implants. Furthermore, this effect may be concentration dependent, centering around the kink concentration as phosphorus exhibits a transition of dominant diffusing species.

Experimental Approach

An experimental procedure that will systematically investigate the interaction of implanted phosphorus ions with silicon interstitials has been developed. The experiments address the study from two different approaches as shown in Figure 10. The first experimental approach is based on the implantation of silicon into wells doped with

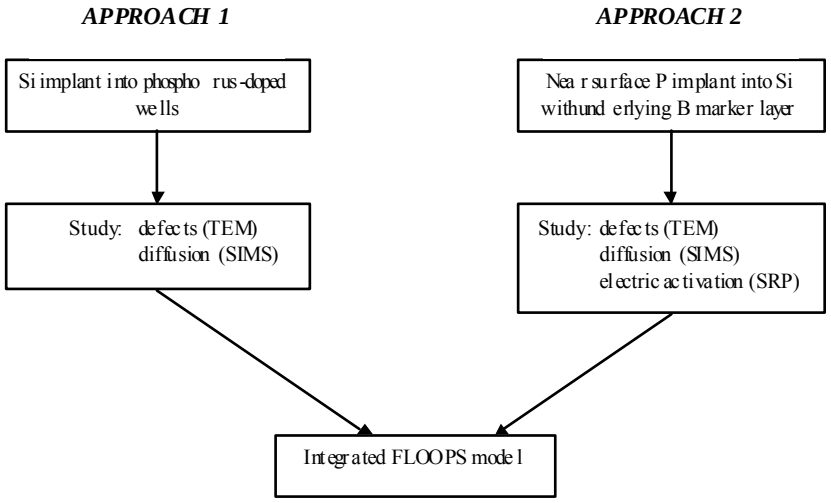

Figure 10. Dual-approach experimentation, "well experiments" & direct phosphorus implants with underlying boron-doped marker.

phosphorus. The second set of experimental studies is based on direct implantation of phosphorus into silicon. In this case, the diffusion enhancements resulting from the phosphorus/interstitial reaction are monitored using an underlying boron doped marker

and compared to the diffusion enhancements resulting from an identical self-implant. Although different in methodology, the results of each experiment are closely related to one another.

Each experimental approach will be conducted using a series of isothermal anneals. Samples are processed for a sequence of times at each temperature to extract dissolution parameters. Furthermore, a novel temperature dependent methodology has been developed to investigate the reaction dynamics and correlation with the phosphorus kink concentration as described in the next section.

Procedure

This section briefly describes common experimental procedures used throughout the investigation. Procedures specific to an individual experiment are included within the description of the individual experiment. Samples were processed using ion implantation followed by subsequent annealing (furnace and RTA). Characterization techniques commonly used include transmission electron microscopy (TEM), secondary ion mass spectrometry (SIMS), and electrical spreading resistance probe (SRP). General descriptions of these characterization techniques can be obtained in reference books.

Isochronal Annealing

Experimental annealing investigations conducted over a range of different temperatures are often carried out isochronaly, in which all samples are compared after identical annealing times. While isochronal annealing is a valid approach in many temperature dependent experiments, it does not allow for the defects to be compared in the same evolutionary phases. For example, at a given isochronal annealing time low temperature samples would observe the defects in their earlier nucleation, growth and coarsening stages (point ① of Figure 11), while high temperature samples would observe

the defects further along in their dissolution phase (point ② of Figure 11), if not already completely dissolved (point ③ of Figure 11).

Figure 12 is from a study of the electrical activation of phosphorus after 30 minute anneals at different temperatures [Web69]. At 600˚C (point ① of Figure 12) the implanted dopant has yet to be fully activated. However, it is now known that defect annealing and TED is not yet complete for this annealing condition. Alternatively, for a 30 minute anneal at 800˚C (point ③ of Figure 12) defect dissolution and TED are near completion. Clearly, isochronal anneals do not capture defects and TED in the same evolutionary states at different temperatures.

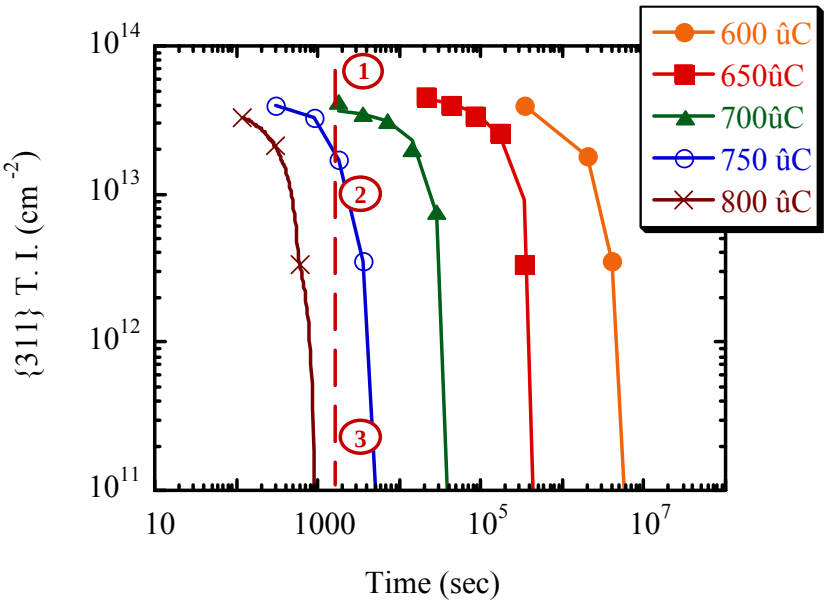

Figure 11. Evolution of {311} defects shows that at 30 min the defects can be in different evolutionary states depending on temperature.

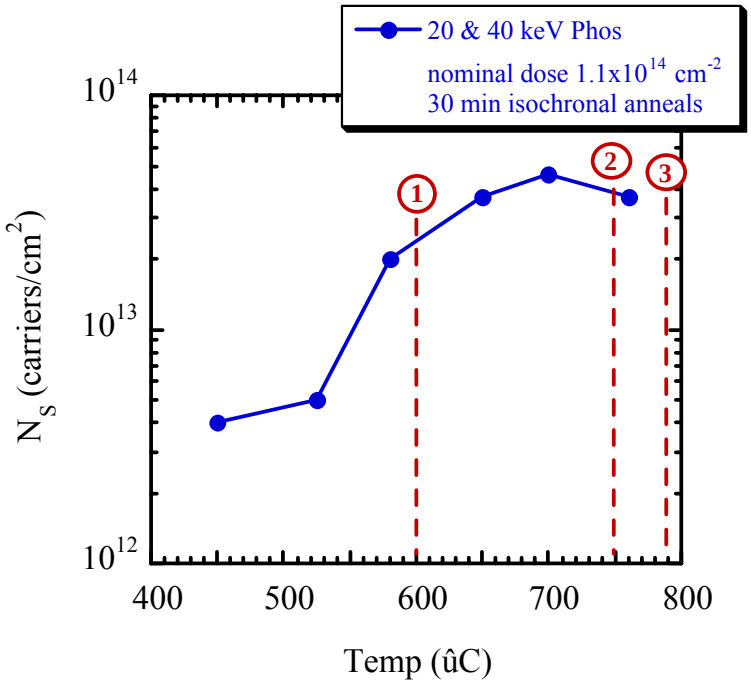

Figure 12. Isochronal (30 min) study of phosphorus implant activation (data from [Web69]).

Iso311 Annealing

Temperature dependent experiments performed in this study are conducted in a much different manner. In order to compare defects in their equivalent states at different temperatures, annealing times are selectively chosen for the given temperature. Figure 13 shows the typical annealing behavior of {311} defects over a wide range of temperatures. The horizontal dashed line is arbitrarily selected for a quantity of trapped interstitials that can be readily quantified with a high degree of reliability. For a given annealing temperature, the dissolution curve will intersect the horizontal dashed line at a particular point. The annealing times corresponding to the desired defect state are shown by the vertical dotted lines (t_1 through t_4). Thus, a complete set of annealing conditions can be obtained which produce identical defects at different temperatures.

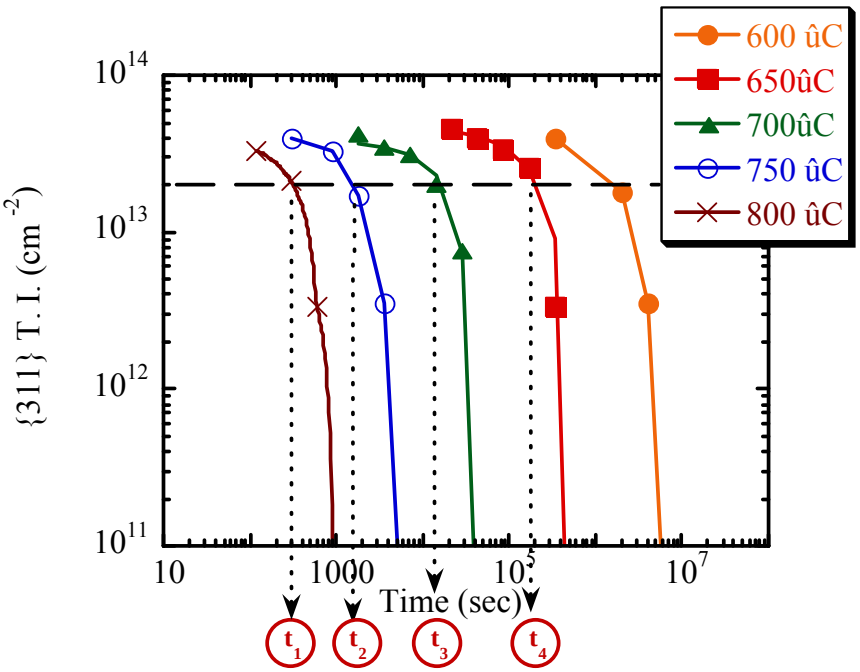

Figure 13. Different annealing times must be used to compare defects in the same evolutionary state at several temperatures.

Table 4. Temperature dependent annealing conditions resulting in equivalent {311} defect states

Temperature (˚C)	Equivalent Time (E_A = 3.6 eV)
950	2.5 sec
850	48 sec
800	5min
750	33 min
700	275 min
650	47 hr, 14 min

Analytically, the temperature and time of all annealing sequences can be selectively determined to provide comparison of equivalent defect and diffusion states based on an Arrhenius activation energy of 3.6 eV. As previously shown, this activation

energy correlates closely with the activation energy of {311} defect dissolution and TED [Eag95]. Thus, annealing will be based on an "equivalent time" relative to the {311} defect and TED timescales. The equivalent annealing conditions are calculated relative to a chosen reference state using the ratio of the rates at different temperatures by:

$$t_2 = \frac{Rate_{T_1}}{Rate_{T_2}} \times t_1 = \frac{e^{\left(\frac{-3.6eV}{kT_1}\right)}}{e^{\left(\frac{-3.6eV}{kT_2}\right)}} \times t_1 \qquad (13)$$

In the above equation, T_1 and t_1 are the temperature (˚K) and time of an arbitrarily chosen reference state, respectively, k is the Boltzmann constant (8.617×10^5 eV/˚K), and T_2 and t_2 are the temperature (˚K) and time of the desired anneal, respectively. Table 4 shows the equivalent states for experimental temperature ranges in which {311} defects and TED are readily observable. It is evident that a wide experimental temperature range (650˚C to 1000 ˚C) exists, over which the desired phenomena can be investigated. It is also evident that at higher temperatures (RTA regime) satisfactory control of the time and temperature is vital. Slight overshoots in either one could result in significant amounts of TED and defect evolution. This is closely guarded against during experimentation.

CHAPTER 3
INTERSTITIAL BEHAVIOR IN PHOSPHORUS BACKGROUND

This chapter begins the experimental investigation into phosphorus-defect interactions using self implants into phosphorus doped wells. An experimental overview and the processing steps used to create the wells will be described. Results of several defect studies and the influence on diffusion will be presented. Finally, the effect of variables such as self-implant dose and annealing temperature will be examined.

Phosphorus-Doped Wells

To gain an understanding of the dopant-defect interactions associated with phosphorus, the experimental investigation starts by observing the behavior of silicon implant damage recovery in phosphorus-doped silicon. This is similar to the experimental approach used by Haynes and Brindos for boron and arsenic, respectively [Hay96, Bri99]. The method requires the creation of doped wells of various background concentrations into which a large excess interstitial concentration is introduced by a self-implant (dose = 1.0×10^{14} cm^{-2}). By creating phosphorus doped wells and implanting silicon into them, the effect of phosphorus on secondary damage can be easily studied using QTEM. This same experimental procedure can also track the release of interstitials from the damaged region and the amount of TED incurred using SIMS. One advantage of implanting into doped phosphorus wells is that the amounts of phosphorus and silicon interstitials can be independently varied. Also, both the intrinsic and extrinsic doping concentrations can be investigated with the same experimental approach.

Creating and Validating Wells

Starting silicon wafers (<100> p-type Czochralski 10-20 ohm-cm) received preamorphizing double Si^+ implants to create an approximately 210 nm deep amorphous layer using an Eaton GSD200 ion implanter. Each amorphized wafer was then doped with a double phosphorus implant (80 keV & 20 keV) to various doses (see Table 5). The amorphous layer was regrown using a low temperature 550 ˚C solid phase epitaxial furnace anneal in an inert N_2 ambient. In order to remove the end-of-range defects and diffuse the implanted phosphorus profile, the wafers were further annealed at 1100 ˚C for 60 min (N_2 ambient). The resulting phosphorus wells had peak concentrations of $2.0x10^{17}$ cm^{-3}, $5.0x10^{17}$ cm^{-3}, $2.0x10^{18}$ cm^{-3}, $4.0x10^{18}$ cm^{-3}, $1.0x10^{19}$ cm^{-3}, and $3.0x10^{19}$ cm^{-3} as shown in the SIMS profiles in Figure 14. The profiles show even doping uniformity in the near surface regions up to a depth of at least 500 nm.

Plan-view transmission electron microscopy (PTEM) revealed a negligible amount of residual end-of-range (EOR) damage. Imaging using cross-sectional TEM

Table 5. Ion implant and anneal conditions used to create the phosphorus-doped wells

	Preamorphizing Implant* (Y/N)	Total Phos. Implant Dose** (cm^{-2})	Anneal*** (Y/N)	Peak Phos. Concentration (cm^{-3})	X_j**** (μm)
(1) Bare Si control	N	-	N	-	-
(2) Preamorphized control	Y	-	Y	-	-
(3) Low phos-well	Y	$8.0x10^{12}$	Y	$2.0x10^{17}$	0.7
(4) .	Y	$2.1x10^{13}$	Y	$5.0x10^{17}$	0.8
(5) .	Y	$8.0x10^{13}$	Y	$2.0x10^{18}$	1.1
(6) .	Y	$2.1x10^{14}$	Y	$4.0x10^{18}$	1.2
(7) .	Y	$8.0x10^{14}$	Y	$1.0x10^{19}$	1.5
(8) High phos-well	Y	$2.4x10^{15}$	Y	$3.0x10^{19}$	1.6

* Dual Si Preamorphizing Implant - 120 keV $1.0x10^{15}$ cm^{-2} & 30 keV $1.0x10^{15}$ cm^{-2}

** Dual P Implant - 80 keV & 20 keV to different doses optimized to attain reasonably flat profile

*** Furnace Anneal - 550 ˚C 60 min & 1100˚C 60 min

**** Junction Depth (X_j) - corresponds to a doping concentration of $1.0x10^{17}$ cm^{-3}

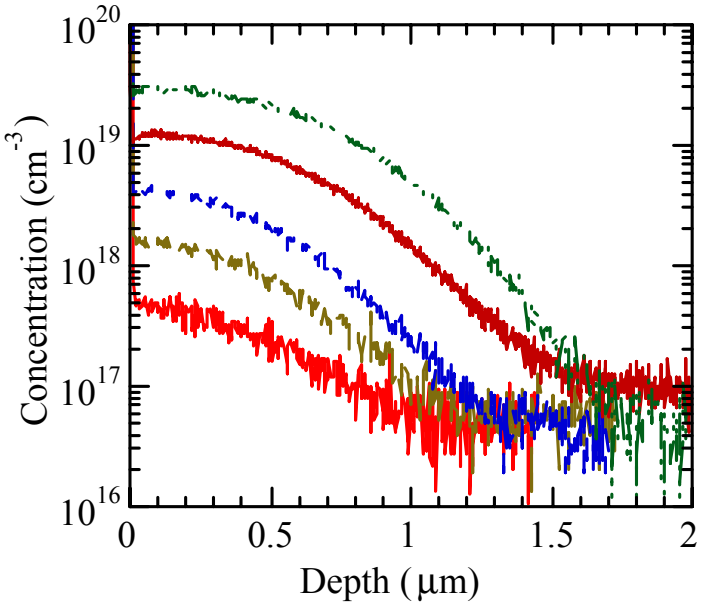

Figure 14. SIMS profiles of phosphorus-doped wells prior to 40keV 1.0x10^{14}cm^{-2} Si^{+} ion implant. All wells exhibit a uniform doping level over a depth of at least 500nm.

confirmed that the EOR dislocations were beyond the former amorphous/crystalline interface. These defects were too deep and of too low of a density to play any role in the experimental observations mentioned in this work [Ram99]. The thermal surface oxide (approximately 25 nm thick) which grew during the high temperature well anneals was removed using a 10:1 HF/NH_4F buffered oxide etch (BOE) prior to the Si self-implant.

The wafers were split, half of which would be used as unimplanted control samples. One sample of each well was then implanted with a non-amorphizing 40keV Si^{+} implant to a dose of 1.0x10^{14} cm^{-2}. A preamorphized undoped annealed wafer and a bare Si wafer were also implanted with Si under the same conditions to serve as control samples. The purpose of the self-implant was to create crystal damage which would coalesce into extended defects upon subsequent furnace anneals. The wells and the

control samples were subjected to a series of 750˚ C isothermal furnace anneals in an inert N_2 ambient.

PTEM confirmed that defects did not nucleate in the unimplanted control samples after the 750˚C anneals. It was also confirmed that the annealed SIMS profiles of wells that did not receive the self implant showed no diffused motion for the temperatures and times investigated.

Effect of Phosphorus on {311} Defects

PTEM micrographs using the $\mathbf{g}_{220}$ weak beam dark field **g**.3**g** diffracting condition after a 750 ˚C 15 min anneal are shown in Figure 15. The bare Si control wafer and the preamorphized control sample (not shown) displayed no discernable differences from each other. All extended defects in the lower concentration and bare Si control samples were {311} defects, rows of self-interstitials lying along the {311} plane elongated in the <110> direction. The density of {311} defects gradually decreased with increasing phosphorus concentration until reaching a critical concentration (between 4.0×10^{18} cm^{-3} and $1.0 \times 10^{19} cm^{-3}$) above which no {311} defects were observed. A low density of uniformly dispersed Type I dislocation loops, however, were observed at the highest phosphorus concentration.

The number of interstitials trapped in {311} defects was quantified from the plan-view TEM images assuming an average of 26 interstitials were contained per nm of dislocation length [Sal79, Eag94]. The defect dissolution after 750˚C isothermal anneals is shown in Figure 16. Dissolution of the {311} defects is fitted using an exponential decay as

$$[Si_i(t)] = [Si_i(0)] e^{(-k_{311} t)} \ [\mathrm{cm}^{-2}] \qquad (14)$$

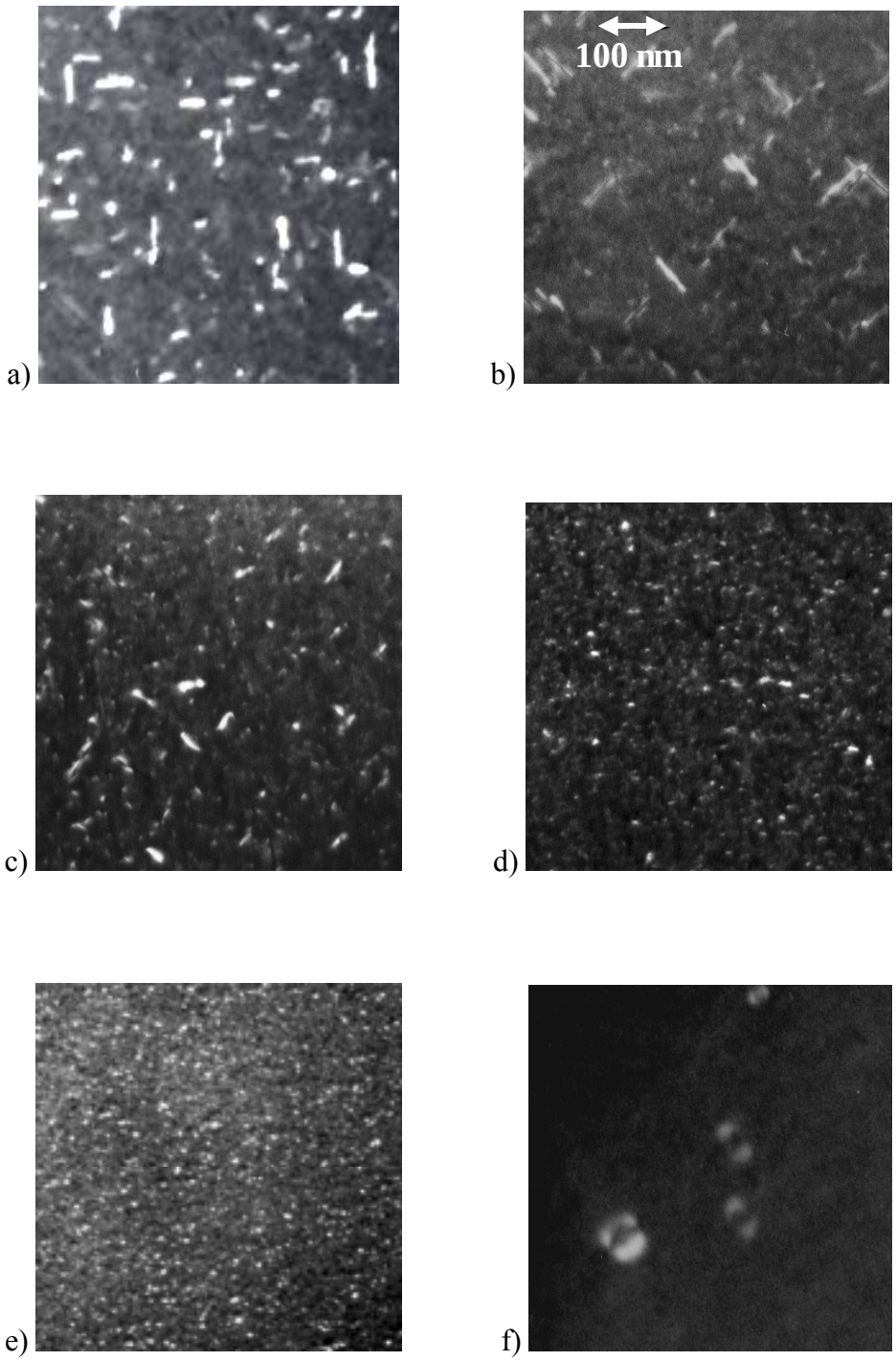

Figure 15. Plan-view TEM images of wells after 40keV $1.0x10^{14}$ cm^{-2} Si^{+} ion implant and 750˚C 15 minute anneal. Background phosphorus concentration: a) undoped, b) $2.0x10^{17}$ cm^{-3}, c) $5.0x10^{17}$ cm^{-3}, d) $4.0x10^{18}$ cm^{-3}, e) $1.3x10^{19}$ cm^{-3}, f) $3.0x10^{19}$ cm^{-3}. Shows a reduction of {311} defects with increased background phosphorus concentration.

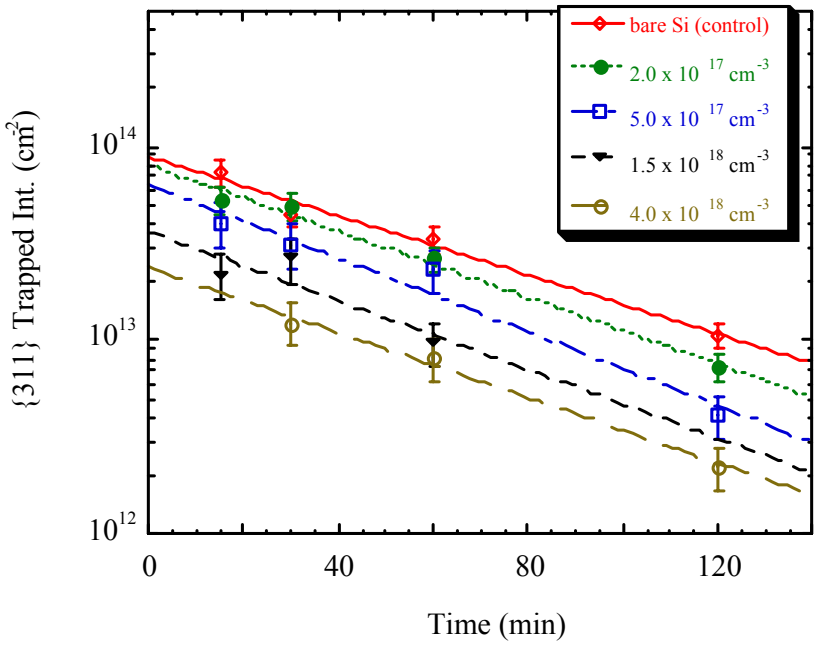

Figure 16. Time dependence of {311} decay for various background phosphorus concentrations (indicated in legends). The dissolution rate of {311} defects is unaffected by phosphorus concentration. Note the reduction in the net number of interstitials with increasing phosphorus concentration.

where $[Si_i(0)]$ is the initial density of interstitials trapped in {311} defects and k_{311} is a characteristic decay rate. The decay rate is unaffected by the phosphorus background concentration, however, there is a reduction of the net number of interstitials trapped in {311} defects with increasing phosphorus concentration. This is similar to previously reported results for arsenic background doping [Bri99]. Extrapolation of the bare Si control sample dissolution curve shows the initial trapped interstitial concentration $[Si_i(0)]$ is approximately 8.5×10^{13} cm^{-2} or 85% of the implanted dose. This is in close agreement with the "plus one" model [Gil91], which suggests that only the excess implanted interstitials contribute to extended defect formation, not the knock-on

interstitials created during the implant. A slight reduction of the initial number of trapped interstitials is observable at a phosphorus concentration of $2.0x10^{17}$ cm^{-3}. This trend continues up to a phosphorus concentration of $4.0x10^{18}$ cm^{-3} in which case the initial trapped interstitial concentration is $2.4x10^{13}$ cm^{-2} or "+0.24". It should be noted that this is approaching the critical dose (approx. $5x10^{12}$ cm^{-2}) necessary for subthreshold {311} defect formation [Eag95]. Following this trend, an initial trapped interstitial concentration of $5.0x10^{12}$ cm^{-2} or "+0.05" would be reached at a phosphorus concentration of approximately $9.2x10^{18}$ cm^{-3}, which is below the peak concentration of the next highest phosphorus well sample ($1.0x10^{19}$ cm^{-3}). In fact, no {311} defects were observed in the higher concentration wells ($1.0x10^{19}$ cm^{-3} and $3.0x10^{19}$ cm^{-3}). However, a low density of dislocation loops was observed in the highest concentration sample within the first anneal time (15 min). Quantitative measurements as shown in Figure 17

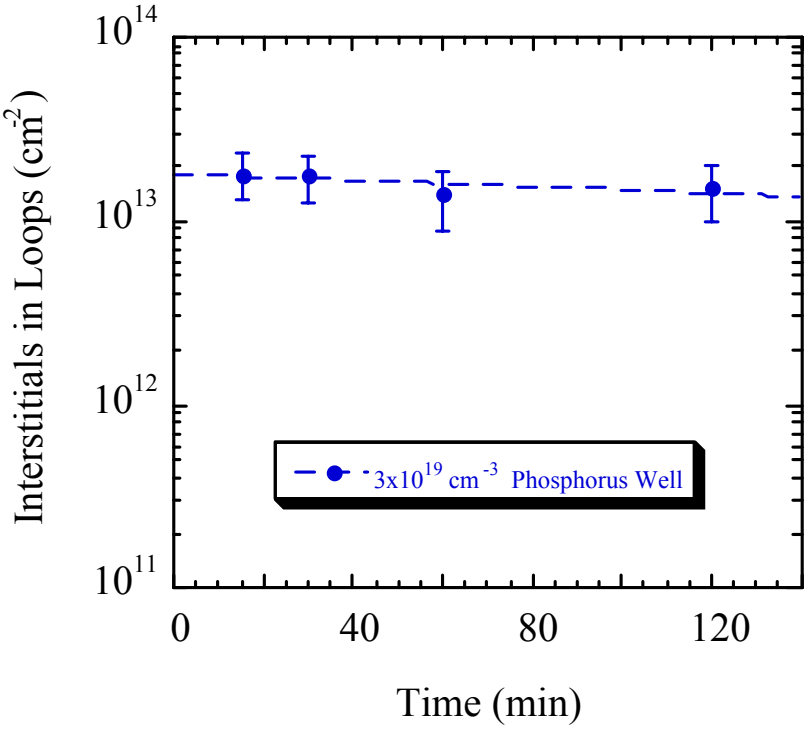

Figure 17. Interstitials trapped in Type I loops remains constant over the times measured.

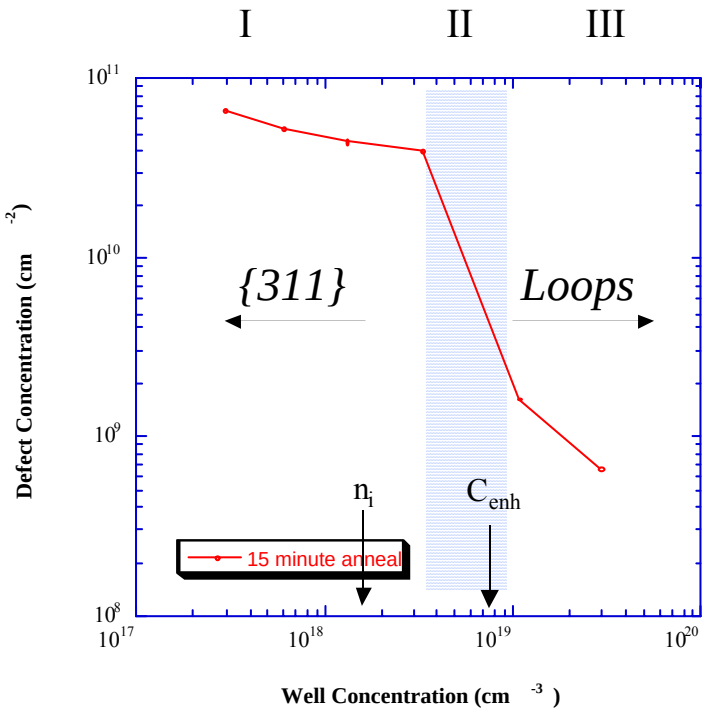

Figure 18. Changes in extended defects with phosphorus concentration can be separated into three regimes; I - {311} defects, II - transitional, III - subthreshold loops.

revealed that the loops maintained a trapped interstitial concentration of approximately $1.6\text{x}10^{13}$ $\text{cm}^{-2} \pm 0.25\text{x}10^{13}$ cm^{-2}. These loops proved to be relatively stable and remain even after the longest anneal time (2 hrs) when the {311} defects were almost completely dissolved in the other samples.

The defect morphology can be separated into three distinct regimes as shown in Figure 18. Regime I occurs at low phosphorus concentrations in which only {311} defects were observed. At higher phosphorus concentrations there is a transition, regime II, were the morphology crosses over from {311} defects to subthreshold loops. Regime III occurs at high phosphorus background concentrations and is identified by the presence of only dislocation loops and no {311} defects. Through this classification, an

understanding of the influence of defects on diffusion may be gained by studying the profile enhancements of samples from each regime.

Diffusion with {311} Defects

The influence of the extended defects on dopant diffusion was investigated by comparing the SIMS profiles of unimplanted wells and self implanted wells after 750˚C furnace anneals as demonstrated in Figure 19. As previously mentioned, no diffused motion was observed in the unimplanted wells after 750˚C furnace anneals. There was considerable motion observed in the implant damaged region and the junction tail of the self-implanted wells after 750˚C furnace anneals. This was true for all well concentrations, with or without {311} defects. However, a significant difference in the nature of the diffusion enhancements was distinguishable for regime I and regime III wells.

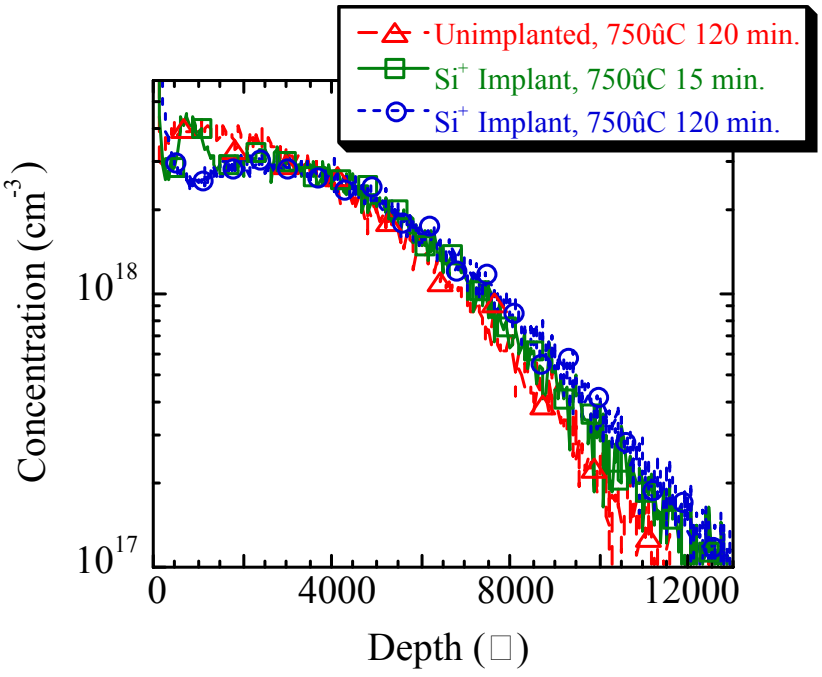

Figure 19. Diffused profiles of 4.0×10^{18} cm^{-3} phosphorus well after self-interstitial implant and anneal.

The diffusion in the implant damaged region of the $4.0x10^{18}$ cm^{-3} well after self implantation and 750˚C annealing is shown in Figure 20. There is a noticeable reduction of phosphorus occurring over the entire implant damaged region, suggesting that phosphorus diffusion is enhanced by the point defects created over the whole self implant cascade. This sample contained {311} defects that gradually dissolve with time during the 750˚C anneals. Localized segregation of the phosphorus is observable at the same depth that the {311} defects are located. The phosphorus is gradually released with time and diffuses away from the projected range of the damaged region. Similar behavior has been reported by Taniguchi to occur with boron [Tan99]. The enhancement time-scale is similar to the {311} dissolution time-scale, clearly demonstrating a transient nature.

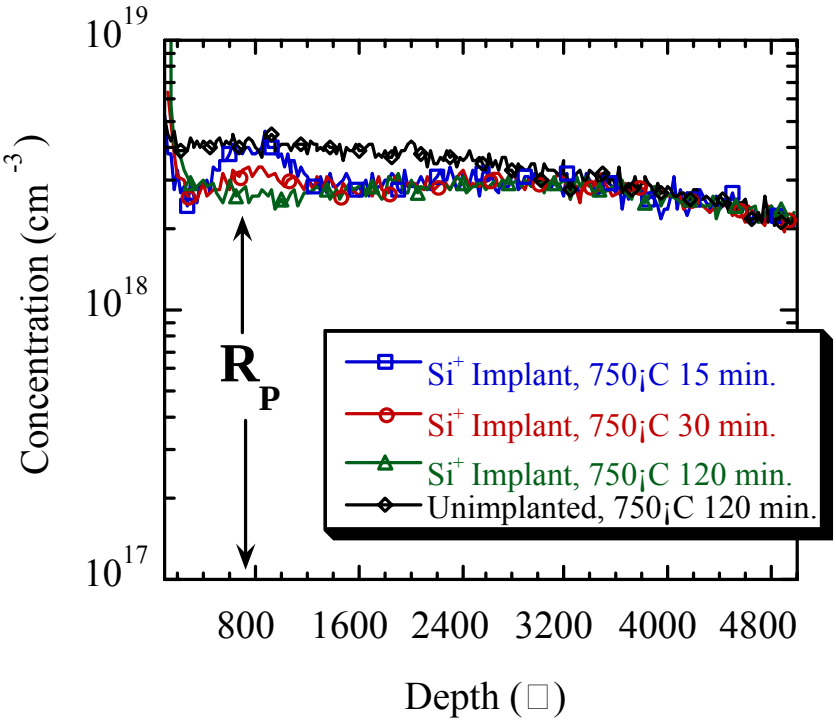

Figure 20. Diffusion in implant damaged region of $4.0x10^{18}$ cm^{-3} phosphorus well after 40 keV, $1.0x10^{14}$ cm^{-2} Si^{+} implant and 750˚C anneal.

Observing the diffusion enhancements in the junction of the well further evidences this. The time averaged diffusivity enhancements of the $4.0x10^{18}$ cm^{-3} well are shown in Figure 21. Diffusion enhancements were extracted using a best fit to intrinsic diffusion with FLOOPS. The gradual reduction of enhanced diffusivity with time is indicative of {311} defect mediated TED. It may be speculated that the initially high diffusivity enhancement is due to the supersaturation of interstitial point defects occuring over the entire damaged region. The excess interstitials in the projected range first coalesce into {311} defects, while the point defects in the Frenkel-pair cascade region cause the phosphorus to quickly diffuse. With longer times, the gradual release of interstitials from {311} defects leads to further diffusion enhancements until interstitial concentrations return to equilibrium values.

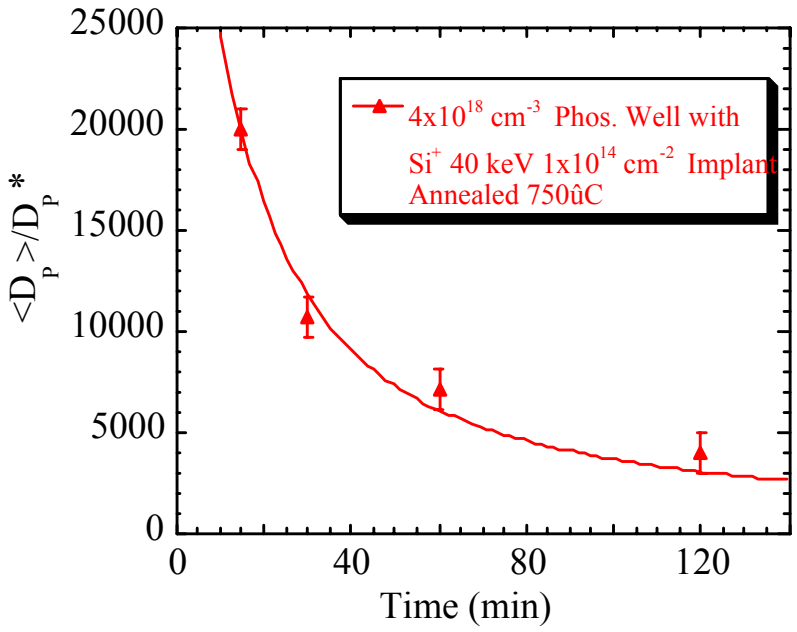

Figure 21. Time averaged diffusivity enhancement, $<D/D^*>$, in tail region of $4.0x10^{18}$ cm^{-3} phosphorus well after Si^+ implant and 750˚C anneals.

Diffusion in the absence of {311} Defects

The nature of the enhanced diffusion for the high concentration wells in regime III when no {311} defects were present was much different. As shown for the self implanted and annealed $3.0x10^{19}$ cm^{-3} phosphorus well in Figure 22, the observed diffusion enhancements in the damaged and tail regions were already completed within the first experimentally measured time-step (15 min). This resulted in an overall diffusivity enhancement, $<D_P/D_P^*>$, of approximately 2100X in the tail region. Close observation of the implant damaged region as shown in Figure 23, reveals that the phosphorus diffusion has occurred mostly within the projected range of the self implant, suggesting the excess implanted interstitials and not those created through cascading damage are responsible for the diffusion enhancement. In fact, the dose of the

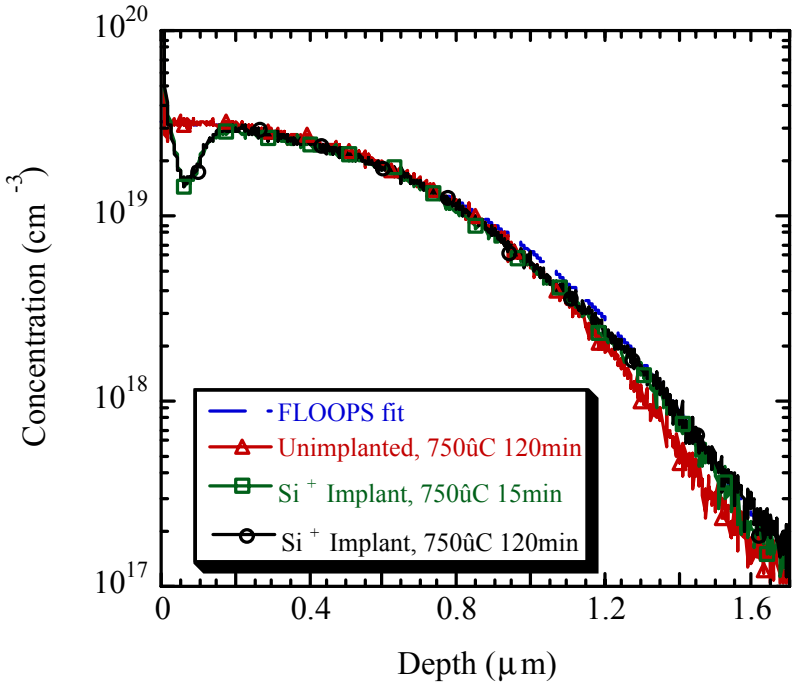

Figure 22. Diffusion in $3.0x10^{19}$ cm^{-3} phosphorus well after Si^+ implant and anneal. Enhancement determined using intrinsic diffusion fit with FLOOPS.

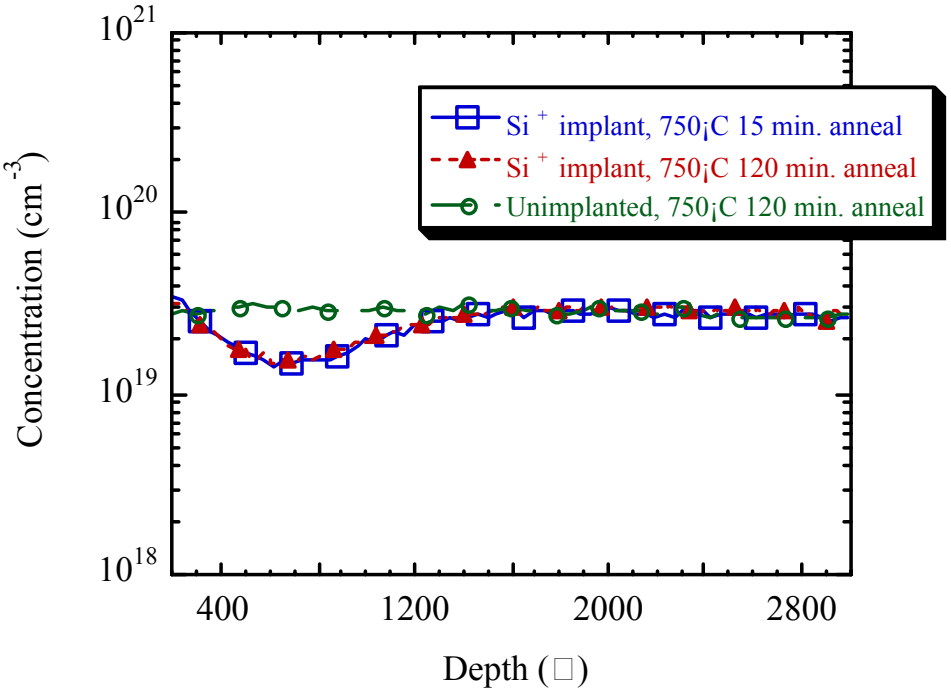

Figure 23. Localized diffusion in the implant damaged region of $3.0x10^{19}$ cm^{-3} phosphorus well after Si^+ implant and 750˚C anneal. Diffusion enhancement is already completed within 15 minutes.

phosphorus atoms missing from the diffused region was calculated to be approximately $1.0x10^{14}$ cm^{-2}, in direct agreement with the implanted silicon dose. From this, one may believe that coupled phosphorus interstitial pairs are responsible for the observed diffusion enhancements in regime III and the reduction of interstitials trapped in {311} defects. This reaction is much faster than the {311} nucleation and dissolution reaction responsible for TED in regime I. From the defect study in the previous section, it was shown in Figure 17 that the subthreshold loops visible in these samples maintained a low density of interstitials and did not exhibit noticeable transient dissolution. This is in agreement with the observed diffusion enhancement behavior.

Effect of Si^+ Implant Dose

The influence of extrinsic variables such as implant dose may be investigated using the same experimental approach. The effect of self-interstitial implant dose was studied for 40keV non-amorphizing Si^+ implants with doses ranging from $5.0x10^{13}$ cm^{-2} to $2.0x10^{14}$ cm^{-2}. After implantation, samples were annealed at 750˚C for 15 minutes.

PTEM images of wells implanted with 40keV Si^+ ions to a dose of $5.0x10^{13}$ cm^{-2} are shown in Figure 24. As expected, the $5.0x10^{13}$ cm^{-2} implant results in less {311} defects than the previously investigated $1.0x10^{14}$ cm^{-2} dose implant. This is in agreement with previously reported results for self-implants into undoped silicon [Eag95]. The undoped control sample (not shown) displayed identical defects to the lightly doped

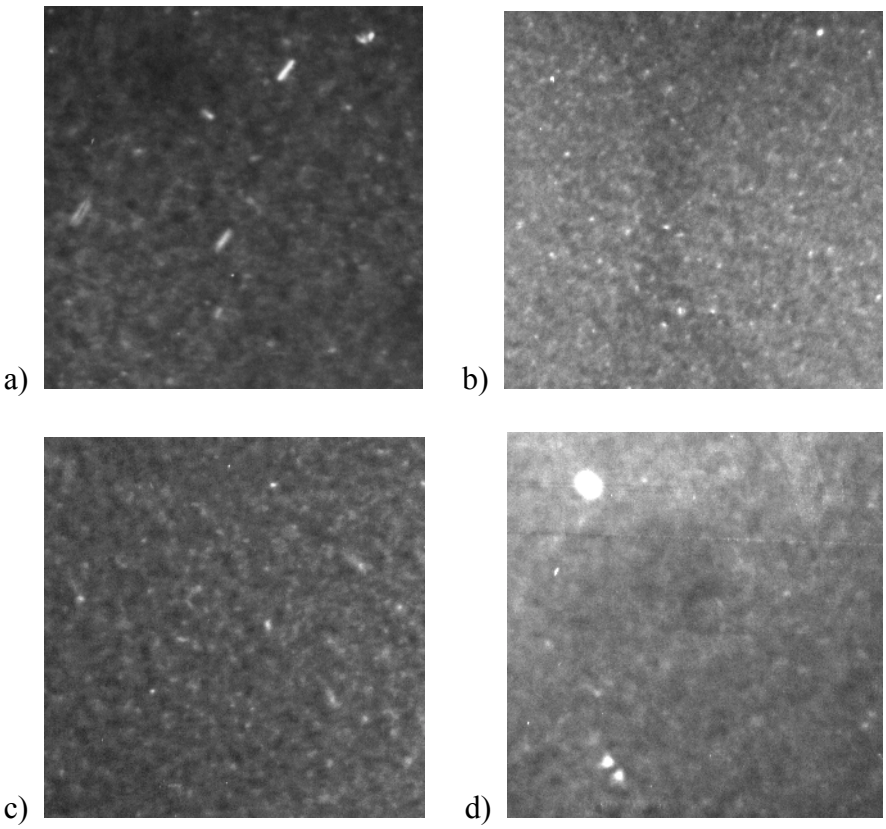

Figure 24. PTEM of wells implanted with 40keV Si^+ ions to a dose of $5.0x10^{13}$ cm^{-2}. Phosphorus well doping concentrations are: a) $5.0x10^{17}$ cm^{-3}, b) $4.0x10^{18}$ cm^{-3}, c) $1.0x10^{19}$ cm^{-3}, d) $3.0x10^{19}$ cm^{-3}.

($5.0x10^{17}$ cm^{-3} concentration) sample shown in Figure 24a. However, as the background phosphorus concentration increases, there is a noticeable reduction of interstitials in {311} defects. The interstitial population incorporated in {311} defects appears to be reduced below the {311} threshold dose (approximately $2.0x10^{13}$ cm^{-2}) with a phosphorus background concentration less than $1.0x10^{19}$ cm^{-3} for these annealing conditions. Again, a low density of small dislocation loops is observable in the highest doped well after the self-implant and 750˚C anneal. These loops did not form in the unimplanted control samples that did not receive the self implant but were subjected to 750˚C anneals. This confirms that the type-I loops that nucleated in the highly doped wells are in fact due to the self implant and not associated with the well formation process.

When the self implant dose is increased to $2.0x10^{14}$ cm^{-2} the nucleation of {311} defects is accompanied by subthreshold dislocation loops. This bi-modal distribution occurs in the undoped control samples, the lightly doped wells, and the highly doped wells as shown in Figure 25. Once again, the undoped control samples and the lightest doped well displayed identical defect morphologies and densities, confirming that phosphorus doping levels below $5.0x10^{17}$ cm^{-3} have no influence on the defects during 750˚C anneals. {311} defect are again shown to decrease with increasing background concentration as previously observed for the lower dose self-implants. Samples that had doping concentrations above $1.0x10^{19}$ cm^{-3} did not contain {311} defects. The subthreshold loops were observable in all samples, regardless of phosphorus background concentration. However, the loop diameter steadily increased with increasing phosphorus concentration as can be seen in Figure 25.

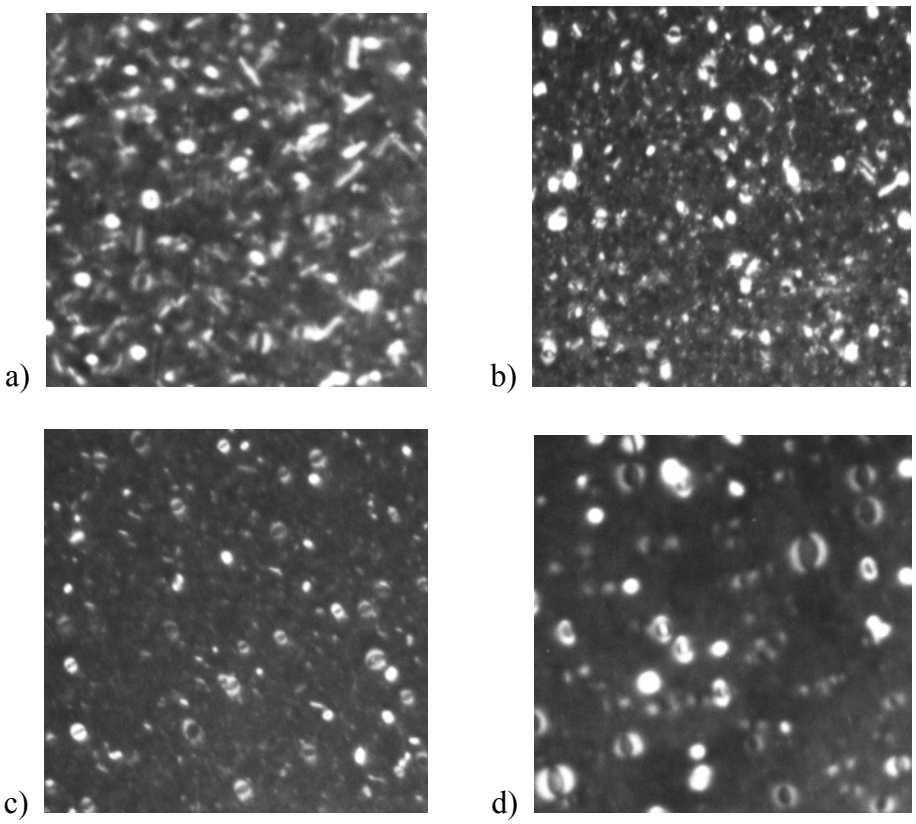

Figure 25. PTEM of wells implanted with 40keV Si^{+} ions to a dose of $1.0x10^{14}$ cm^{-2}. Phosphorus well doping concentrations are: a) $5.0x10^{17}$ cm^{-3}, b) $4.0x10^{18}$ cm^{-3}, c) $1.0x10^{19}$ cm^{-3}, d) $3.0x10^{19}$ cm^{-3}.

Observation of the phosphorus profiles reveals that the Type-I loops can have a significant effect on diffusion. Figure 26 compares the diffusion enhancements of the $3.0x10^{19}$ cm^{-3} phosphorus well after various doses of self implants and 750˚C annealing for 15 minutes. Considerable diffusion occurs in the implant damaged region and the tail region for all self implant doses. Enhancement in the tail after $5.0x10^{13}$ cm^{-2} and the $1.0x10^{14}$ cm^{-2} self implants and annealing are proportional to the implant dose. However, this trend seems to saturate above $1.0x10^{14}$ cm^{-2}, as the enhancement from the $2.0x10^{14}$ cm^{-2} self-implant produces the same amount of motion as the $1.0x10^{14}$ cm^{-2} self-implant.

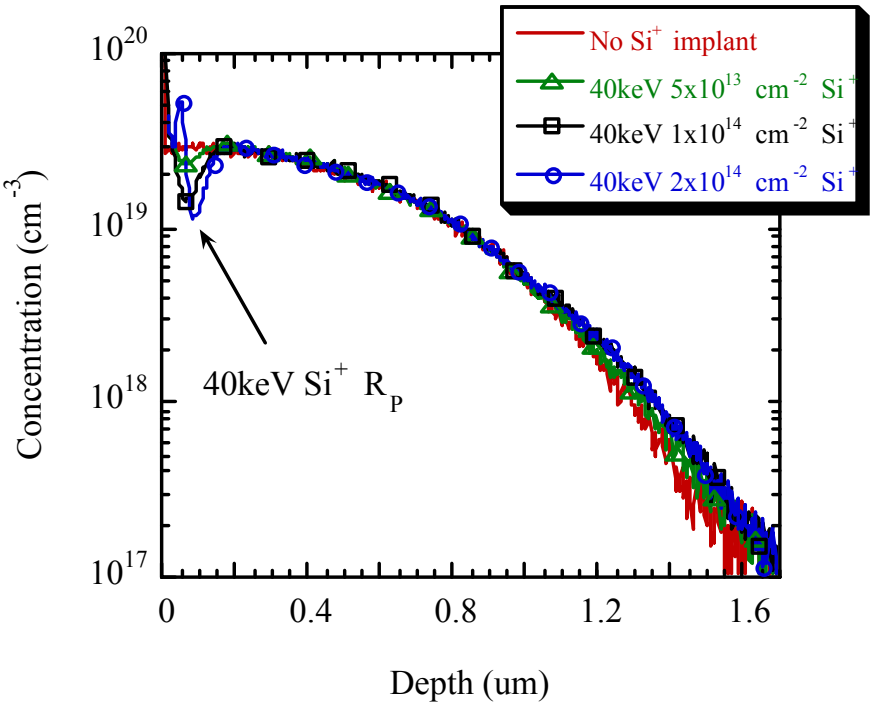

Figure 26. Diffused profiles after Si^+ implants and 750˚C, 15minute anneal. Magnitude of diffusion enhancement in $3.0x10^{19}$ cm^{-3} phosphorus well is proportional to the self-interstitial implant dose up to $1.0x10^{14}$ cm^{-2} above which enhancement is saturated. Pile-up is noticeable after $2.0x10^{14}$ cm^{-2} implant due to Type-I loops.

This may be due to the excess interstitials being incorporated into subthreshold loops as the self-implant dose is increased above $1.0x10^{14}$ cm^{-2}. Another possible explanation could be that a higher percentage of the excess interstitials generated by the $2.0x10^{14}$ cm^{-2} implant diffused towards the surface and not into the bulk.

Similar behavior is observed when comparing the diffusion in the damaged region. The amount of phosphorus that has diffused away from the implant-damaged region is also proportional to the self-implant dose. However, there is a large pile-up of dopant in the $2.0x10^{14}$ cm^{-2} near the projected range. The pile-up occurs at the same

depth where the subthreshold loops have formed, indicating that the dopant is segregating to the loops. This is similar to the often observed pile-up of dopant in the end-of range damage resulting from amorphizing implants.

Temperature Dependence

It is interesting to note that in Figure 18 the transition from {311} defects occurs at a concentration higher than the intrinsic carrier concentration (n_i) but close to the phosphorus kink concentration, C_{ENH}. As the kink concentration is an intrinsic temperature dependent property its correlation to the transition in defects can be investigated using the iso311 annealing approach. If indeed the two phenomena are

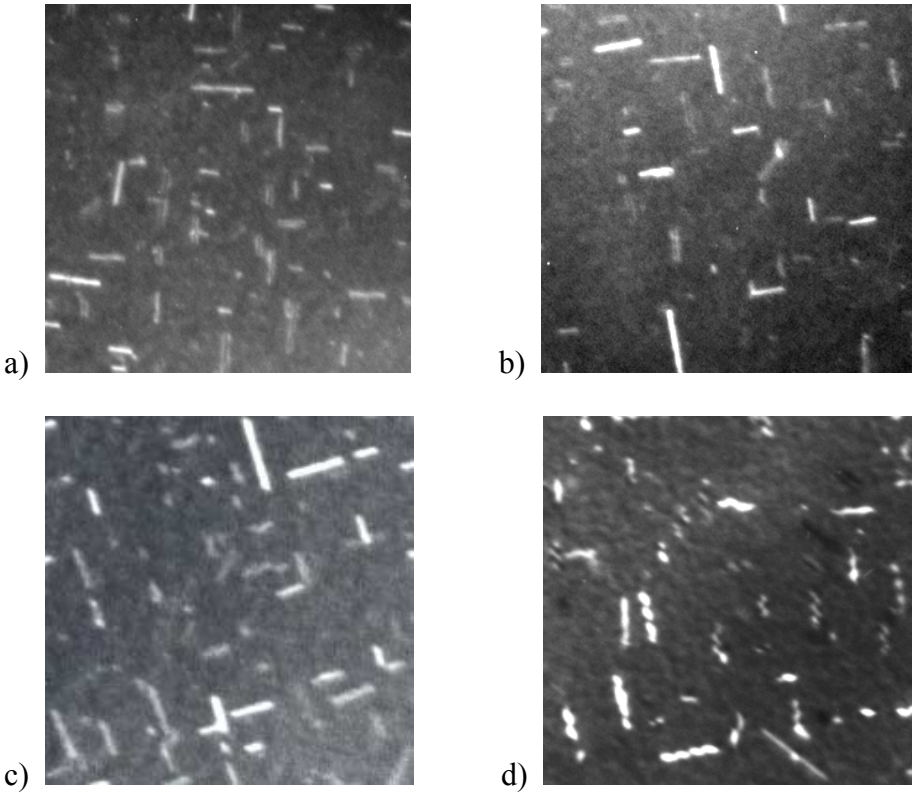

Figure 27. PTEM of undoped samples implanted with 40keV Si^+ ions to a dose of $1.0x10^{14}$ cm^{-2} and iso311 annealed: a) 650˚C, 47 hours 14 minutes b) 700˚C, 275 minutes c) 750˚C, 30 minutes d) 800˚C, 5 minutes.

related, they should exhibit the same temperature dependence. The primary focus of this section is to experimentally investigate the correlation between the two.

The phosphorus wells and undoped control samples were annealed according to the temperatures and times previously given in Table 4 after a 40keV 1.0×10^{14} cm^{-2} self-implant. Comparison of the undoped control samples confirms that {311} defects are in equivalent states as they display similar density and size distributions for all anneals. This is clearly displayed in Figure 27. QTEM further confirmed that all of the undoped control samples contained approximately 5.0×10^{13} cm^{-2} interstitials trapped in {311} defects.

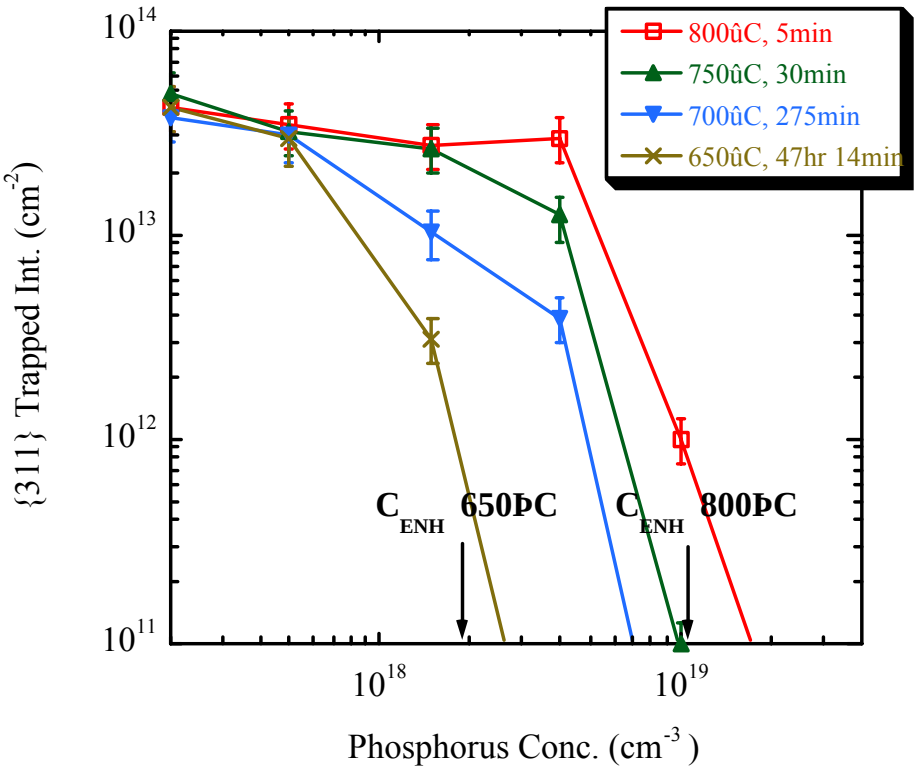

Figure 28. Trapped interstitial content as a function of background phosphorus concentration at several temperatures. Similar values are observable in lightly doped samples. The transition concentration decreases at lower temperatures.

This analysis is extended to the phosphorus doped samples as shown in Figure 28. The number of interstitials trapped in {311} defects is plotted as a function of background phosphorus concentration for several temperatures. At low phosphorus concentrations the trapped interstitial content is the same for all temperatures and in close agreement with the undoped control samples. For all annealing temperatures, the number of interstitials trapped in {311} defects dramatically decreases as the phosphorus concentration increases. The concentration at which this transition occurs is highly temperature dependent, increasing with increasing annealing temperature. One may

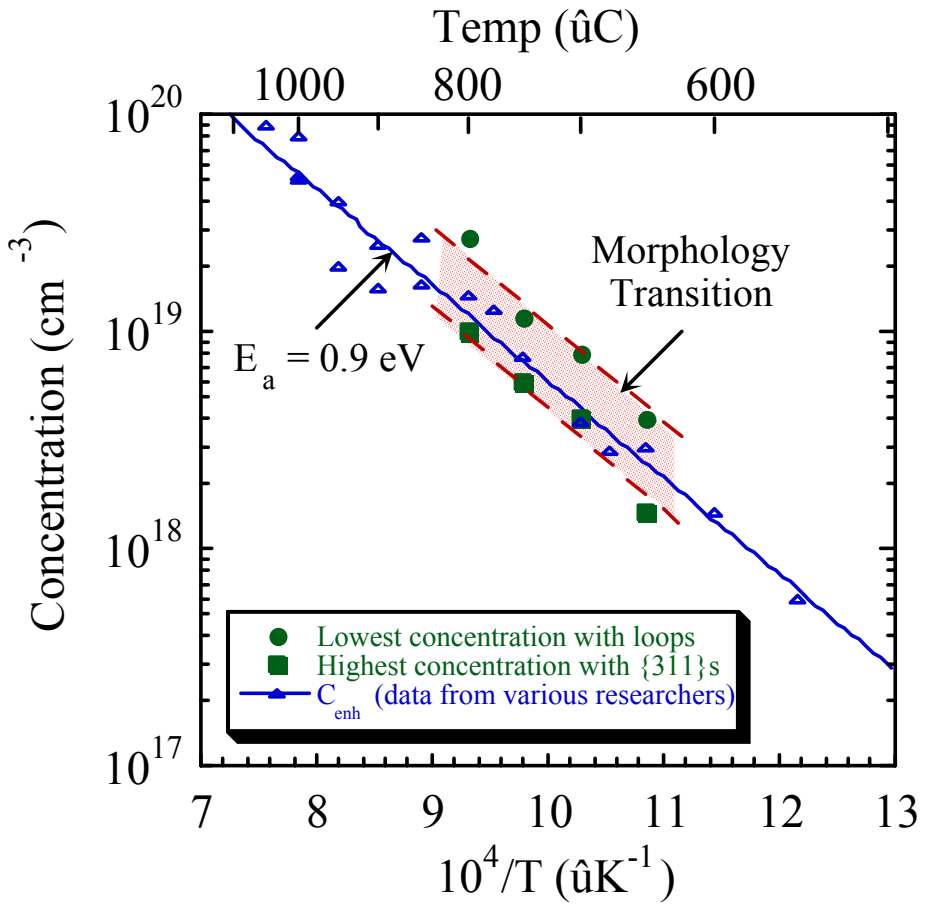

Figure 29. Comparison of the phosphorus concentration at which the defect morphology transition occurs and the phosphorus kink concentration shows strong correlation.

argue that changes in the {311} dissolution due to the phosphorus invalidate the iso311 comparison. However, this argument may be dismissed as the {311} defect dissolution has been shown to be unaffected by the phosphorus background concentration (see Figure 16).The shift in transition concentration with temperature appears to follow the same trend as the phosphorus kink concentration. Indeed it seems that the observed effect is centered about the kink concentration for the entire experimental range. This is clearly exemplified when shown on an arrhenius plot as in Figure 29. The experimental well concentrations about which the transition is centered are plotted as a function of inverse temperature. The kink concentration reported by Schwettmann *et al* [Sch72] is also shown for comparison. There is an amazingly strong correlation between the two, suggesting that both phenomena are influenced by the same reaction.

Discussion

Comparison of these results to similarly observed phenomena for other dopant types provides additional qualitative insight into possible contributing mechanisms. The phosphorus concentration at which {311} nucleation ceases in this experiment is lower than the concentrations at which this phenomena occurs for other dopants such as boron and arsenic [Hay96, Bri99]. When performed with a boron background doping, it was shown that above a boron concentration of $1.0x10^{18}$ cm^{-3}, the number of interstitials trapped in {311} defects decreases with increasing boron concentration, almost completely eliminating the {311} defects for boron concentrations above approximately $1.0x10^{19}$ cm^{-3}. This dependence was attributed to the trapping of interstitials by B_SB_i clusters [Hay96]. When performed with an arsenic background, a similar but less pronounced reduction of interstitials trapped in {311} defects started for arsenic

concentrations in excess of $2.0x10^{17}$ cm^{-3}. {311} defects were still observable at much higher arsenic background concentrations of $3.0x10^{19}$ cm^{-3}. The dissolution rate was also shown to be consistent over all arsenic concentrations, suggesting that once nucleated the {311} defects are sufficiently stable regardless of the surrounding dopant environment. Thus the dopant induced interstitial capture process is dominant prior to or during the nucleation phase of the {311} defect kinetics. Two possible explanations for the reduction of interstitials trapped in {311} defects were presented: a) trapping of interstitials by arsenic clusters such as As_2I, or b) increased diffusivity of the silicon interstitials due to the increase in fermi energy caused by arsenic doping[Bri99]. Comparison of the n-type dopants indicates that the increase in interstitial diffusivity due to changes in Fermi level from higher doping is not the direct cause of the observed phenomena as it is much more pronounced in the case of phosphorus at equivalent n-type doping levels. However, the effect of shifting the fermi level may lead to a complex dependence of individual point defect energy levels and dopant charge state energy levels associated with each individual dopant type.

An argument could be made that the hydrostatic strain induced by the individual dopant due to size mismatch with silicon may alter the ability of the lattice to accommodate excess interstitials through strain relaxation. A rough measure of the mismatch can be approximated using the tetrahedral covalent atomic radii (B=0.88Å, P=1.10Å, Si=1.17Å, As=1.18Å) [Kit76]. As such, one would expect boron-doped silicon to accommodate excess interstitials better than phosphorus doped silicon prior to the onset of dislocation formation. However, this is in disagreement with the experimental results which shows phosphorus appears to be more effective at consuming

excess interstitials than boron thus affecting the nucleation of {311} defects at lower concentrations.

Clustering explanations are further supported by the trend of how significantly the dopants seem to trap interstitials (phosphorus > boron > arsenic). This appears reasonable as phosphorus exhibits a higher fraction interstitialcy diffusion component, f_I, than both boron and arsenic. Thus it is expected to be more likely to bind with free interstitials during the initial stages of implant damage recovery as it displays a higher affinity for interstitials. Additionally, the preferred diffusion mechanism of the impurity could influence how well the stress induced by implantation of excess interstitials may be relaxed.

Summary

In this chapter, the interaction of phosphorus and silicon interstitials was experimentally investigated using self-implants into phosphorus-doped wells. It is experimentally confirmed that like arsenic and boron, the background concentration of phosphorus doped silicon effects the nucleation of {311} defects created through silicon implantation and annealing. Increased phosphorus doping reduces the number of interstitials bound in {311} defects without altering the {311} defect dissolution rate. At high concentrations, {311} defects never form, only subthreshold loops. The defects were categorized into three separate regimes ({311}, crossover, and loop), dependent upon the background phosphorus concentration. These secondary defects strongly influence the observed nature of diffusion enhancements in the dopant profile.

{311} defects were present under all conditions in which transient enhanced diffusion occurred during this experiment. Phosphorus segregated to the damaged region

were {311} defects reside, resulting in a gradual release over time. This suggests that the interstitials stored in the metastable defects lead to the transient diffusion enhancements until point defect concentrations approach equilibrium levels. The diffusion enhancement in samples that did not contain {311} defects was already completed within the first experimentally measured anneal step. Loops observed in these samples are stable enough to remain even after the longest anneal times. These loops do not lead to measurable diffusion enhancements.

The reduction of interstitials in {311} defects may be attributed to the capture of interstitials by phosphorus atoms during the initial stage of implant damage recovery and appears to be strongly associated with the reaction causing phosphorus kink and tail diffusion. Comparison to other dopants confirms that the adjustment of fermi level due to increased doping concentrations is not the direct cause of the noticeable reduction of interstitials trapped in {311} defects.

CHAPTER 4
DIRECT PHOSPHORUS IMPLANTATION

While the previous chapter of experimental work investigated deviations in the annealing behavior of self-interstitial implants in phosphorus doped wells, it remains to be seen if this carries over to direct phosphorus implants. This chapter will experimentally investigate the dopant-defect interactions as they occur after direct phosphorus implantation. Results from these experiments will be compared to identical silicon implants when appropriate. It will conclude with a discussion of the similarities to the experimental observations of chapter three and research by other investigators.

Phosphorus Implants / Boron Marker Layer

As previously described, a great deal of research has focused on the effects of near-surface Si implants on underlying boron marker layers. Similar experiments can be performed using near-surface phosphorus implants. As phosphorus is very close in mass to silicon, it is relatively easy to design experiments that separate the effects of primary and secondary damage. Literature review from chapter two confirmed that phosphorus implantation can result in the formation of different defects than implantation of silicon under identical conditions. This investigation will use the underlying boron marker layer to detect the release of interstitials form the implanted region. The release of interstitials will be observed in both the boron diffusion and the extended defects, allowing for the correlation between the two. Unlike silicon, the diffusion of the implanted phosphorus can be monitored directly with SIMS (the implanted silicon cannot be distinguished from

the target silicon). Additionally, the electrical activation of the implanted phosphorus is investigated using SRP and Hall measurements. The fraction of activated dose is extracted from these electrical measurements for further correlation with the QTEM and SIMS results.

Experimental Setup

The experimental setup used to study phosphorus-defect interactions due to direct phosphorus implantation is shown schematically in Figure 30. Boron marker layers can be created by ion implantation and annealing [Pac90], molecular beam epitaxy (MBE) [Sto97], or epitaxial chemical vapor deposition (CVD) [Cow99]. CVD grown samples with a single B spike were obtained from Intel Corp. for use in this experiment. A boron-doped spike was grown at 850˚C on a (100) Si substrate using a commercial single wafer epi system. B_2H_6 was used as the boron source and $SiCl_2H_2$ was the silicon source. The boron spike is approximately 500Å wide with a peak concentration of approximately $2.0x10^{18}$ cm^{-3}. A 4000Å buffer layer of Si was deposited on top of the boron spike. This was followed by a 200Å PECVD screen oxide.

The as-deposited wafers were qualified by monitoring the diffusion of the boron spike after thermal anneals and comparing with intrinsic diffusion values. This was done by annealing two sample pieces at 750˚C for short (30 to 60 minutes) and long (4 to 6 hours) times in a nitrogen ambient and then measuring the profiles with SIMS . The as deposited and annealed profiles (see Figure 31) were analyzed using FLOOPS and the boron diffusivities were extracted. It was determined that the as-grown boron diffusivity enhancements for all the spikes were less than 10X for the short time anneal and decreased with time to approximately 3X (compared to an accepted value for the boron diffusivity). The results indicate that although there is a slight enhancement grown into

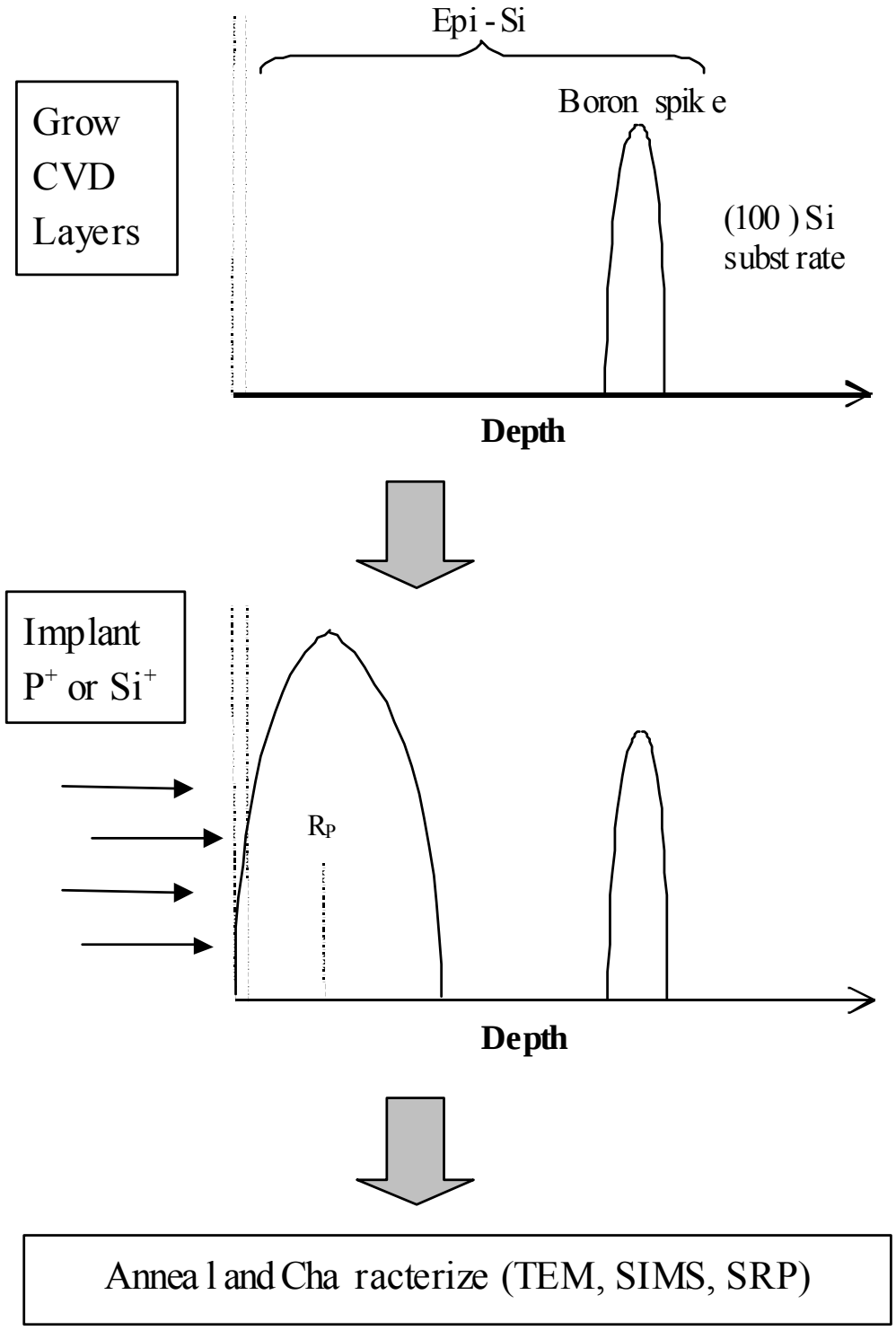

Figure 30. Schematic of experimental process used to investigate phosphorus-defect interactions due to direct implants.

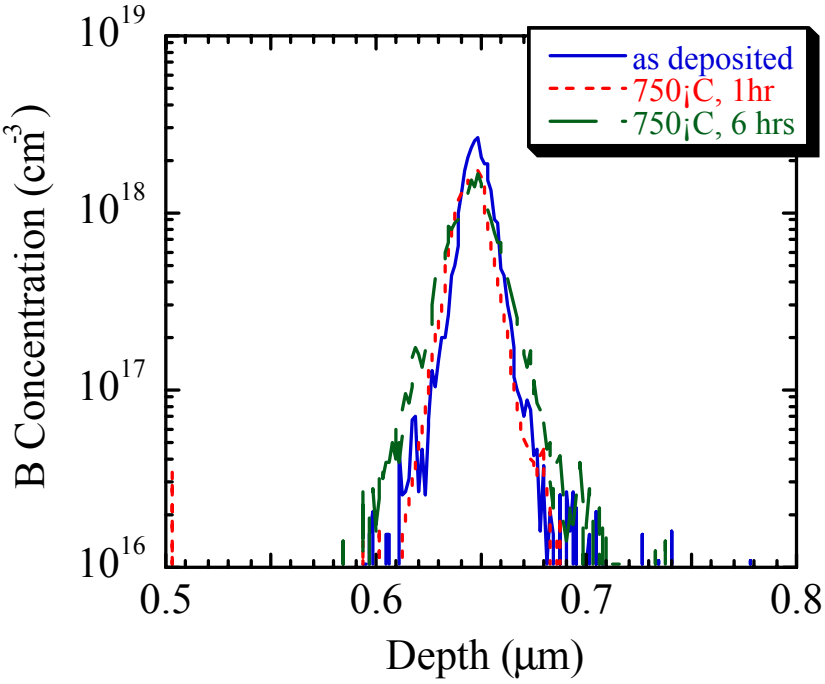

Figure 31. SIMS profiles of CVD grown boron marker layer samples; as-deposited and after 750˚C anneals.

the samples, it is too low to introduce error into the experiment. PTEM of these samples also revealed no extended defects before or after annealing.

After qualification of the CVD material, various doses of phosphorus or silicon were implanted with an energy of 40 keV into the epitaxially conditioned wafer. The projected range of this implant is approximately 650Å. The implants were performed for low ($2.0x10^{13}$ cm^{-2}) and medium ($1.0x10^{14}$ cm^{-2}) doses. Higher doses would result in amorphization and is beyond the scope of this investigation. After implantation the wafer surfaces were capped with approximately 2000Å of low temperature SiO_2 for protection. This process was performed at a low enough temperature to avoid disruption to the primary implant damage. Following processing, the wafers were split and furnace

annealed in an inert N_2 ambient at various temperatures and times. The oxide cap was stripped using a buffered oxide etch (BOE).

Samples were characterized using TEM, SIMS, and SRP. Phosphorus SIMS profiles were obtained on a PHI6600 system using a Cs primary beam. The boron dopant profiles were measured on a Cameca IMS-3f secondary ion mass spectrometer using an O_2 source beam to get better concentration resolution. Thin plan view TEM samples were created by lapping the wafer from the backside followed by a hydroflouric/nitric acid etch. Extended defects were imaged using **g**.3**g** weak beam dark field (WBDF) $\mathbf{g}_{220}$ with the deviation from the exact Bragg condition being slightly positive ($s \geq 0$). SRP profiles was obtained from an external testing facility. Measurements were conducted using a probe load of 2.5 grams with a bevel angle of approximately 0.003 degrees and 4.0 μm step increments.

Low Dose Implants

As shown in Figure 32, enhanced boron diffusion occurred in both the 40 keV 2.0×10^{13} cm^{-2} Si and P implanted samples. The enhancements were analyzed using the procedure described in Appendix B and the characteristic diffusion distance is shown in Figure 33. Diffusion enhancements were already completed within 15 minutes at 750°C with no observable transient nature. It is important to note that at this dose the overall diffusion length due to Si and P implants was approximately the same. This is in agreement with similar experimental results by other researchers [Cha00]. No visible crystallographic defects were observed in plan view TEM analysis. This suggests that all the excess interstitials created during implantation were released during the initial stages of damage recovery.

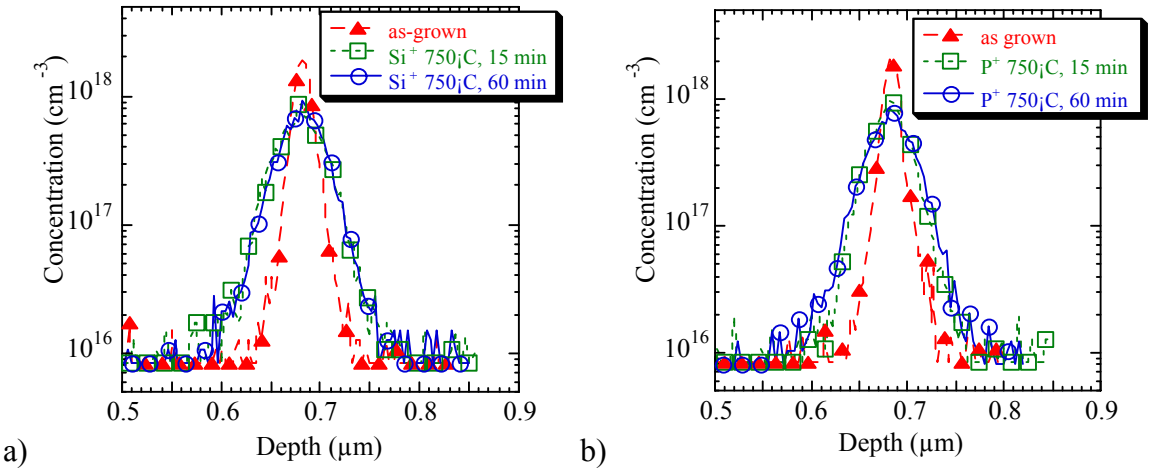

Figure 32. Diffusion of boron spikes after 750˚C anneals for 40keV, $2.0x10^{13}$ cm^{-2} implants: a) Si^+ implant b) P^+ implant.

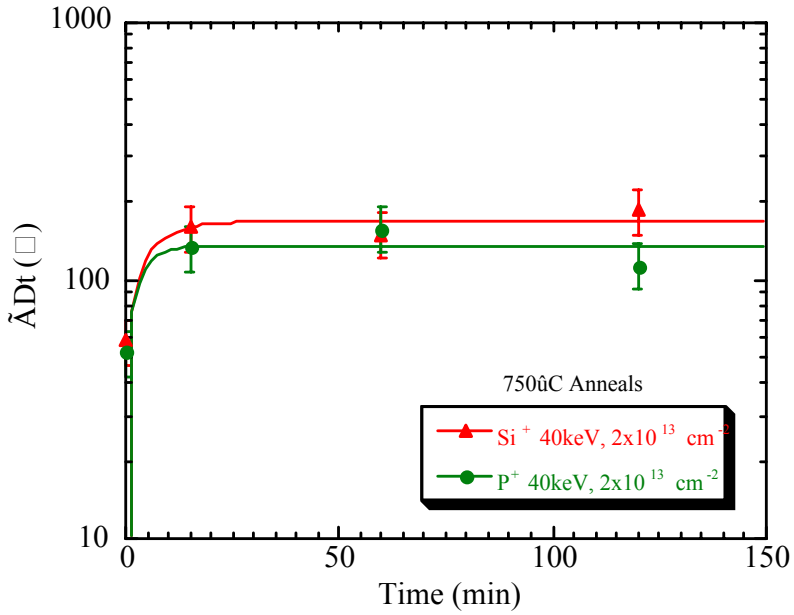

Figure 33. Boron spike diffusion enhancements at 750˚C for $2.0x10^{13}$ cm^{-2} dose implants show similar enhancements for silicon and phosphorus

Medium Dose Implants

Extended defects begin to form from 40keV Si^+ implants at higher doses (above $2.0x10^{13}$ cm^{-2}) [Eag95]. This results in transient diffusion enhancements of nearby dopants starting with a very high diffusivity that gradually decays back to intrinsic values as the implant damage anneals. As expected, this is the behavior observed in the boron spike after the 40keV medium dose ($1.0x10^{14}$ cm^{-2}) Si^+ and P^+ implanted samples are annealed at 750˚C. SIMS profiles of samples after annealing at 750˚C for 15 and 120 minutes are shown in Figure 34. In both cases, the boron spike displays significant motion after 15 minutes similar to what occurs after low dose implants. Unlike the lower dose case, the boron spike continues to display enhanced diffusion at 120 minutes if medium dose implants are used. Furthermore, at both annealing times the boron spike profiles seem to be wider if phosphorus is implanted as compared to silicon. This is more clearly demonstrated when displayed side by side as in Figure 35

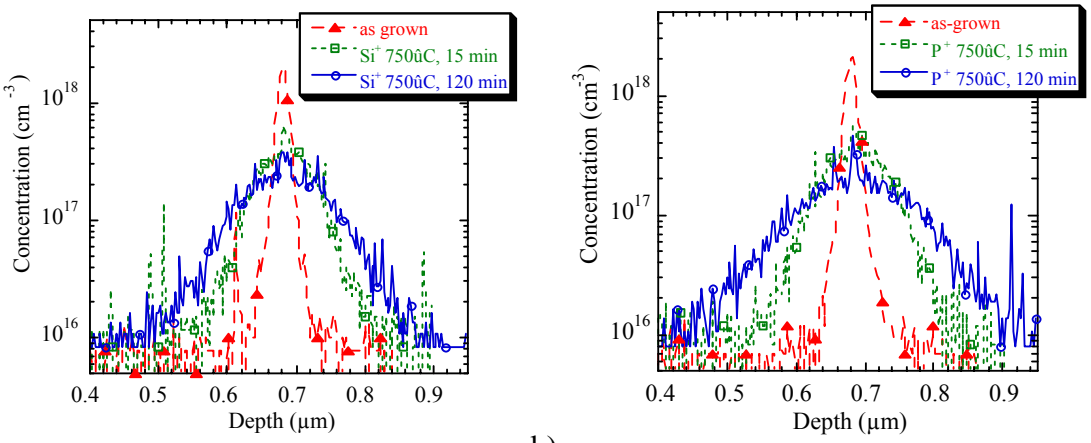

a) b)

Figure 34. Boron spike enhancements after 40 keV, $1.0x10^{14}$ cm^{-2} implants and 750˚C anneals: a) Si^+ implant b) P^+ implant.

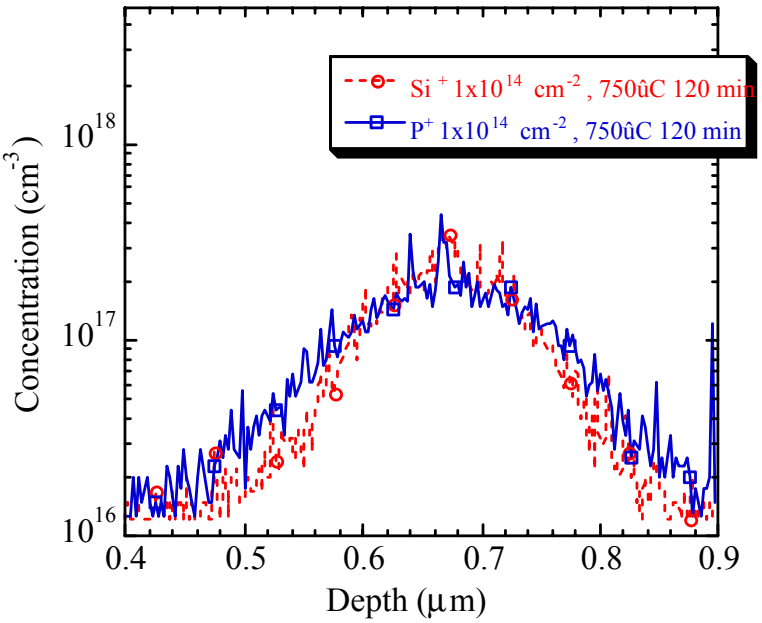

Figure 35. Comparison of boron spike enhancements for 40 keV, 1.0x10^{14} cm^{-2} implants after annealing at 750˚C for 120 minutes.

The characteristic diffusion distances (see Appendix B) resulting from 40 keV 1.0x10^{14} cm^{-2} silicon and phosphorus implants annealed at 750°C are shown in Figure 36. The experimental data is closely fit as a function of time with the following equation

$$\Delta X_J \propto \sqrt{Dt} = \sqrt{D\tau\left(1 - e^{-t/\tau}\right)} \qquad (15)$$

The time constant, τ, is representative of the duration of exponential decay. The time constants extracted from the best fit to the data is 35 minutes and 38 minutes for silicon and phosphorus implant induced diffusivity, respectively. This clearly demonstrates that the transient nature occurs over the same time scale for both cases after 750˚C annealing. As earlier noted, the overall diffusion distance resulting from phosphorus implants is greater than that from silicon implants. This is shown to be consistent for all annealing

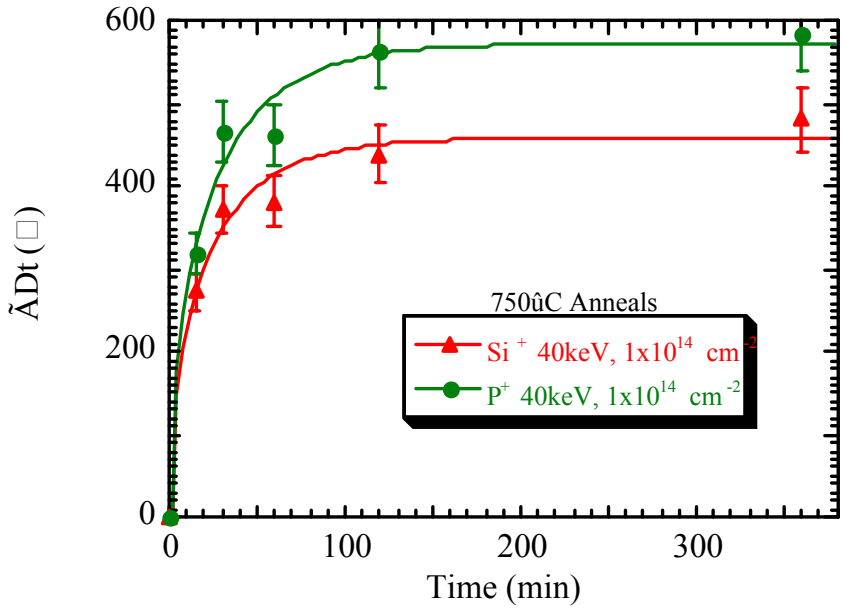

Figure 36. Boron spike diffusion enhancements at 750˚C for $1.0x10^{14}$ cm^{-2} dose implants show greater enhancement due to phosphorus.

times at 750˚C. This suggests that a greater number of interstitials escape from the damaged region during the early stages of damage recovery when extended defects are nucleating. These results are in agreement with those previously reported by other researchers [Gri93, Cha96]. To provide further information about the cause of these deviations the extended defect evolution is investigated using TEM.

Comparing PTEM images of the extended defects from 40 keV, $1.0x10^{14}$ cm^{-2} silicon and phosphorus implants shows a distinct difference. This is readily observable in Figure 37 after 750˚C annealing for 15 min. {311} defects form in Si implanted samples (Figure 37a). Phosphorus implanted samples form small dot defects (Figure 37b). These defects were believed to be a/2<110> dislocation loops with diameter approximately 20-60Å [Des97]. These defects are at the resolution limits of conventional TEM so it is

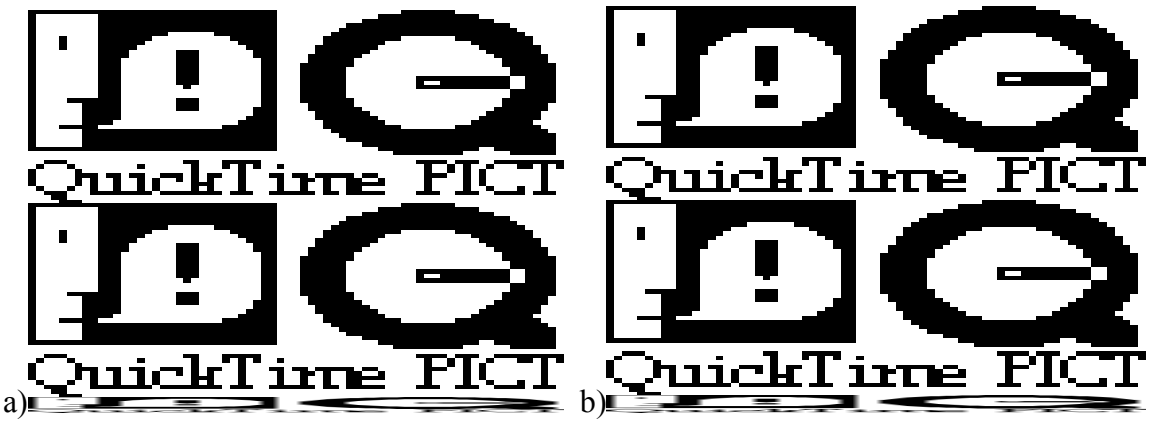

Figure 37. PTEM of extended defects from 40keV, $1.0x10^{14}$ cm^{-2} ion implants after 15 minute anneal at 750˚C: a) Si^+ implant, b) P^+ implant.

difficult to determine if inside/outside contrast exists. However, after annealing at 750˚C for 30 minutes the coarsening phase is near completion. At this time the defects are at their largest and elongation can be discerned, identifying them as {311} defects. With longer annealing the defects continue to dissolve and eventually loops are the only defects present. This behavior is indicative of {311} defects, suggesting the dot defects are in fact very small "proto" {311} defects. It is also possible that these dot defects are a complex of phosphorus atoms and silicon interstitials.

The release of interstitials from the {311} defects created from the Si^+ implant can be linked to the flux of interstitials that causes enhanced diffusion of the boron spike. However, the dissolution of dot defects is much more difficult to quantify. Even so, the dissolution can still be linked to the diffusion enhancements by considering the loop formation process as shown in Figure 38. The density of dot defects is approximately constant throughout the duration of TED. At longer times there is a sudden reduction in the density of dot defects. This coincides with the appearance of larger (d≈20nm) dislocation loops. These loops have a much lower density and are not believed to

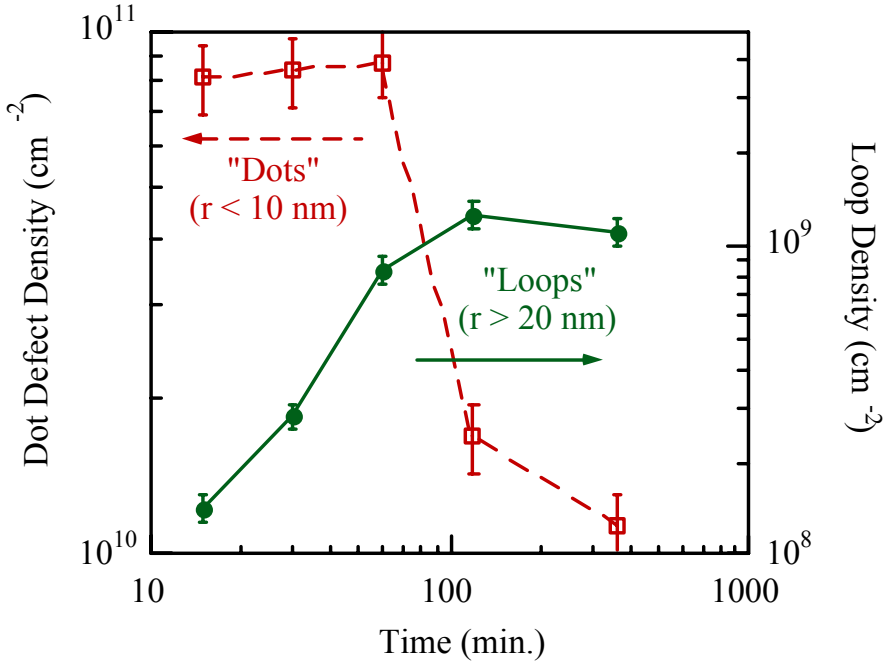

Figure 38. Quantified phosphorus 40keV, 1.0x10^{14} cm^{-2} implant defect dissolution at 750˚C.

contribute to the release of interstitials causing TED. Based on the number of interstitials that are initially contained in the dot defects and remain in the loops, it is evident that the dot defects are not the primary source of TED in phosphorus implanted silicon. It is quite possible that smaller clusters of interstitials below the resolvable limit of conventional TEM are present. The dissolution of the dot defects occurs at approximately the same time as the TED of the boron spike saturates.

An Arrhenius plot of dot defect dissolution time at different temperatures (shown in Figure 39) reveals an activation energy of 3.3eV (data from this study and [Des97]). This suggests that the dot defects become unstable at the same time that the flux of interstitials to the boron spike returns to equilibrium. Thus, the dissolution process may be limited by interstitial driven phosphorus diffusion.

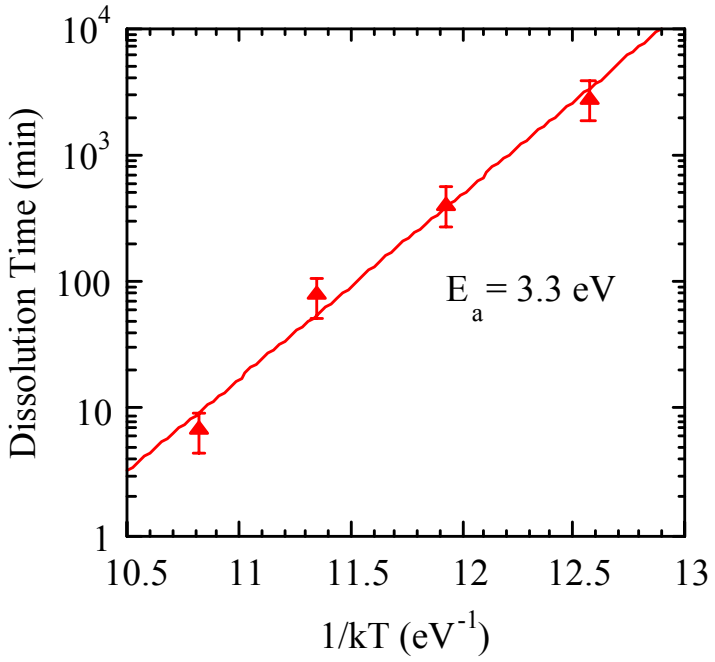

Figure 39. Arrhenius dependence of dot defect dissolution (data from this work and [Des97]).

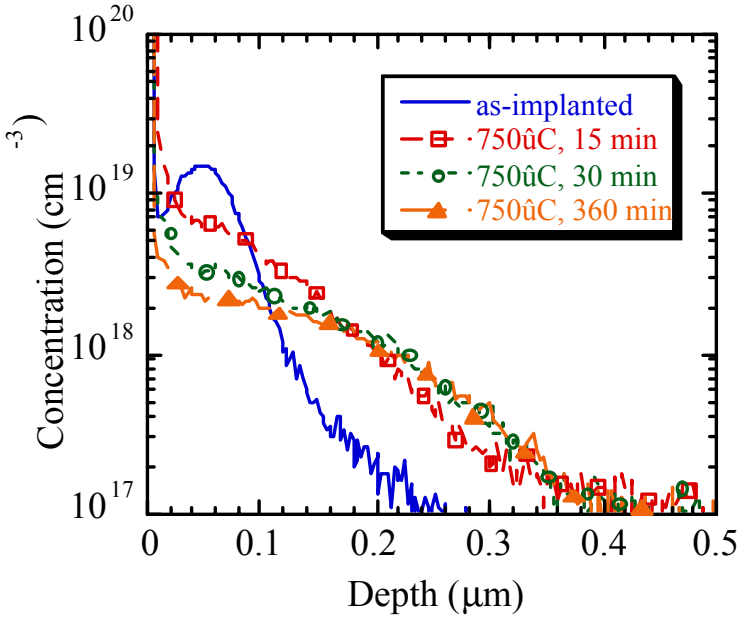

Figure 40. SIMS profiles before and after 750˚C diffusion of 40keV phosphorus implanted to a dose of 1.0×10^{14} cm^{-2}.

SIMS profiles of the implanted phosphorus after 750˚C annealing are shown in Figure 40. There is a significant amount of diffusion after 15 minutes causing the junction depth to shift approximately 0.1μm deeper into the bulk. This is accompanied by a reduction of the peak concentration. The junction has shifted an additional 0.04μm after another 15 minutes of annealing (30 minutes total) at 750˚C, with TED being almost complete. After another 330 minutes (360 minutes total) of annealing there is little more shift in junction depth signaling that the phosphorus diffusivity returned to equilibrium after 30 minutes from the start of annealing at 750˚C. This is slightly faster than TED observed in the boron spike. The profiles display a completely gaussian shaped profile at long annealing times. Also, a noticeable portion of the implanted dose has been lost to the SiO_2/Si interface. This is due to a diffusion-limited process that is magnified by the effects of TED [Gri95].

Temperature Dependence of Defects

The temperature dependence of the defect dissolution is investigated using isothermal annealing at several temperatures. Implantation of the B-spike samples with 40 keV Si^+ ions to a dose of $1.0x10^{14}cm^{-2}$ leads to the formation of {311} defects during annealing. The dissolution in the number of interstitials trapped in {311} defects is shown in Figure 41 for temperatures between 650-750˚C. The data can be fit using an exponential decay as given in equation 14. The dissolution time constant, $\tau_{311}=1/k_{311}$, from this experiment ($\tau_{311}\approx$20 minutes at 750˚C) is slightly faster than the control samples in the previous well experiment ($\tau_{311}\approx$55 minutes at 750˚C), however, both are within the range of previously reported values. An arrhenius plot of the dissolution rates as shown in Figure 42 reveals an activation energy of approximately 4.2eV. This is

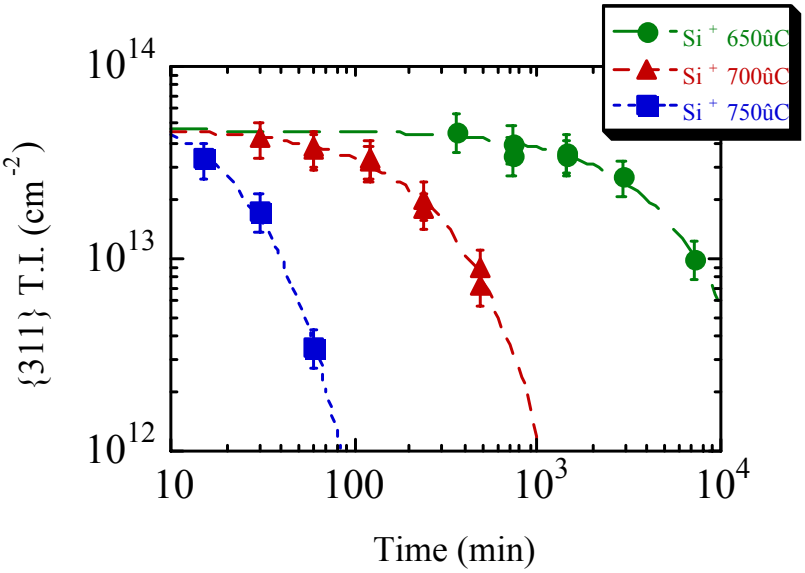

Figure 41. {311} defect dissolution in B-spike samples implanted with 40keV Si^+ ions to a dose of $1.0x10^{14}cm^{-2}$ and annealed at various temperatures. Dissolution is fit using an exponential decay

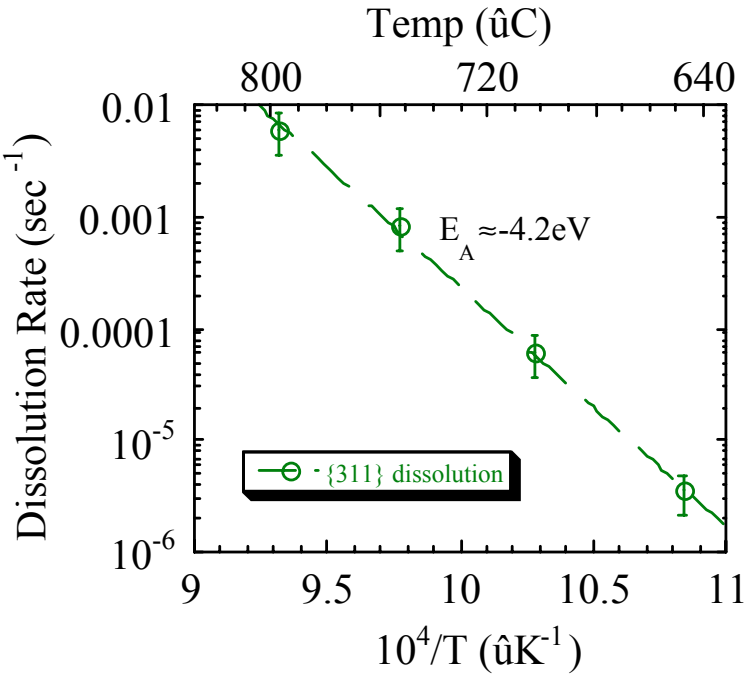

Figure 42. Arrhenius dependence of the {311} defect dissolution rate in the 40keV, $1.0x10^{14}cm^{-2}$ Si^+ implanted B-spike samples has an activation of approximately 4.2eV.

higher than the originally reported energy of 3.6eV for $5.0x10^{13}cm^{-2}$ Si^{+} implants [Eag95] but similar to the energy reported for 50 keV Si^{+} implants with a dose of $1.0x10^{14}cm^{-2}$ [Des97].

As previously shown in Figure 37 the extended defects that form in the B-spike samples implanted with phosphorus are not always {311} defects. Differences in extended defects that form due to phosphorus implants are highly temperature dependent. Further insight into this peculiar nature may be gained by using the iso311 annealing methodology to study the defects as done in the previous chapter for the phosphorus doped well experiments.

A 750˚C anneal for 30 minutes is chosen as the reference annealing condition as the defects are fully coarsened and can be reliably quantified. The equivalent anneal conditions used were 650˚C for 48 hours, 700˚C for 240 minutes, 750˚C for 30 minutes, 800˚C for 5 minutes, and 950˚C RTA for seconds. The wafer implanted with 40 keV P^{+} ions to a dose of $1.0x10^{14}$ cm^{-2} was split and annealed at iso311 equivalent temperatures and times. The samples identically implanted with Si^{+} ions were also annealed at the same time to serve as control samples. As expected, PTEM of the self-implanted and annealed samples show identical density and sizes of {311} defects for all annealing conditions.

Figure 43a shows the {311} defects after annealing at 700˚C for 240 minutes as a representative example of the self-implanted samples. Formation of {311} defects from silicon implants displays no deviation with temperature. PTEM images of the phosphorus implanted samples are shown in Figure 43b-f. Unlike the self-implanted

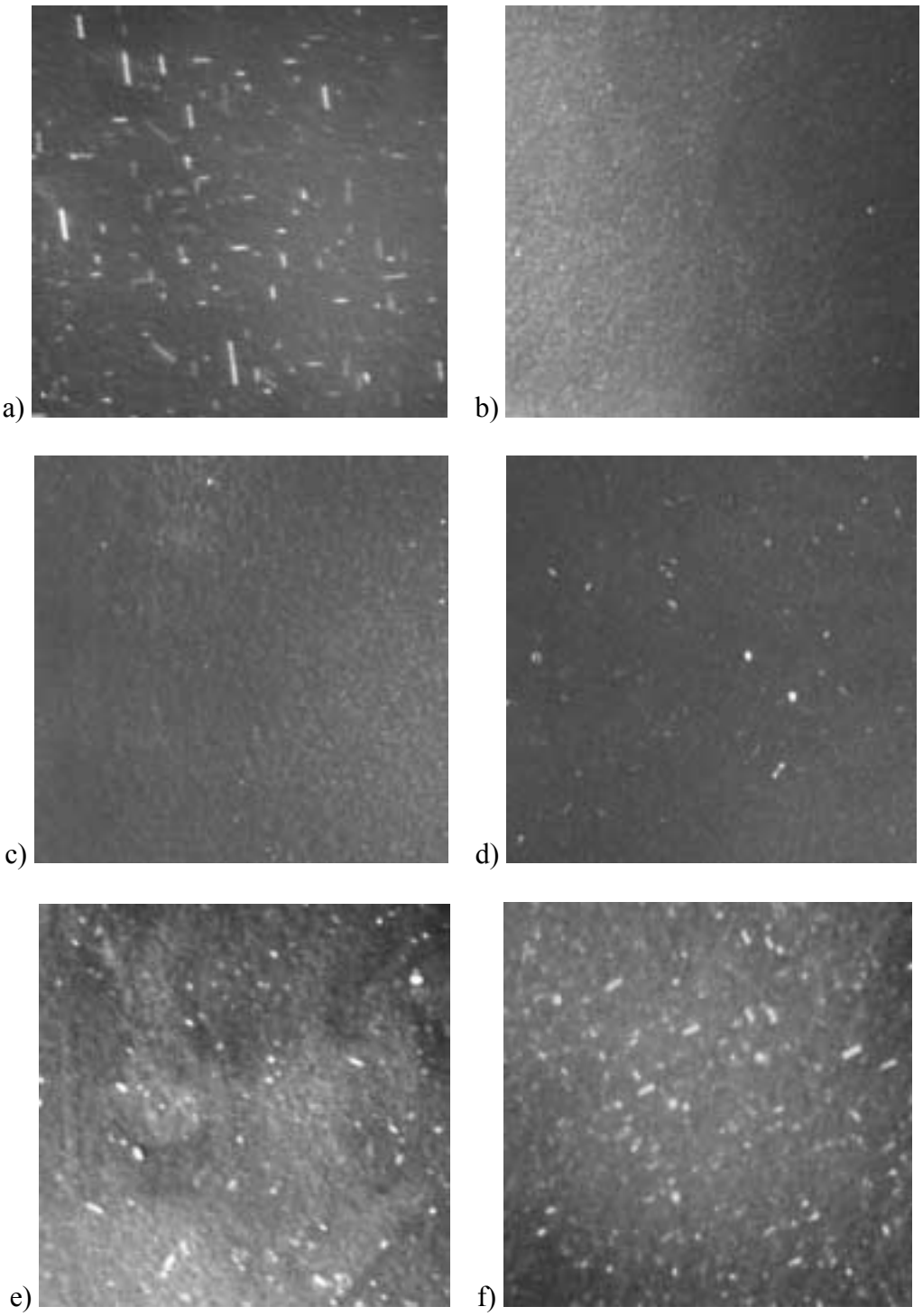

Figure 43. PTEM of 40 keV $1x10^{14}$ cm^{-2} implanted samples after iso311 anneals: a) Si^{+} 700˚C 240 minutes, b) P^{+} 650˚C 48 hours, c) P^{+} 700˚C 240 minutes, d) P^{+} 750˚C 30 minutes, e) P^{+} 800˚C 5 minutes, f) P^{+} 950˚C 2 seconds.

samples, there is a significant temperature dependence observed in the phosphorus implanted samples. The phosphorus implanted sample annealed at 950˚C for 2 seconds (Figure 43f) contains a uniform distribution of {311} defects as did the self-implanted control samples. There is also a low density of small dislocation loops and the {311} defects are slightly smaller than the {311} defects in the control samples. This is similar to the previously reported differences in 100keV silicon and phosphorus implants with a dose of $1.0x10^{14}$ cm^{-2} when annealed at 750˚C [Li99].

As the annealing temperature is reduced, there is a significant reduction of {311} defects in the phosphorus implanted samples. In fact, there are relatively no observable defects present in the samples annealed at 700˚C and 650˚C. It seems that the formation of {311} defects has been fully suppressed in the samples annealed below 750˚C. Quantification of the {311} defects as shown in Figure 44 demonstrates the magnitude of this effect. The number of interstitials trapped in {311} defects is plotted as a function of the annealing temperature (using the equivalent time). The number of interstitials confined in {311} defects as a result of self-implants is constant at all temperatures, containing approximately $2.0x10^{13}$ cm^{-2}. At high temperatures, the {311} defects in phosphorus implanted samples contain nearly the same amount of interstitials as the self-implanted control samples. However, below 800˚C there is a dramatic reduction of interstitials bound in {311} defects.

The interaction of phosphorus atoms with the primary implant damage is the only variable this can be attributed to. In this case it seems there is a critical temperature below 800˚C for which this reaction becomes very strong. As demonstrated in the previous chapter in the case of the phosphorus doped well experiments, the suppression

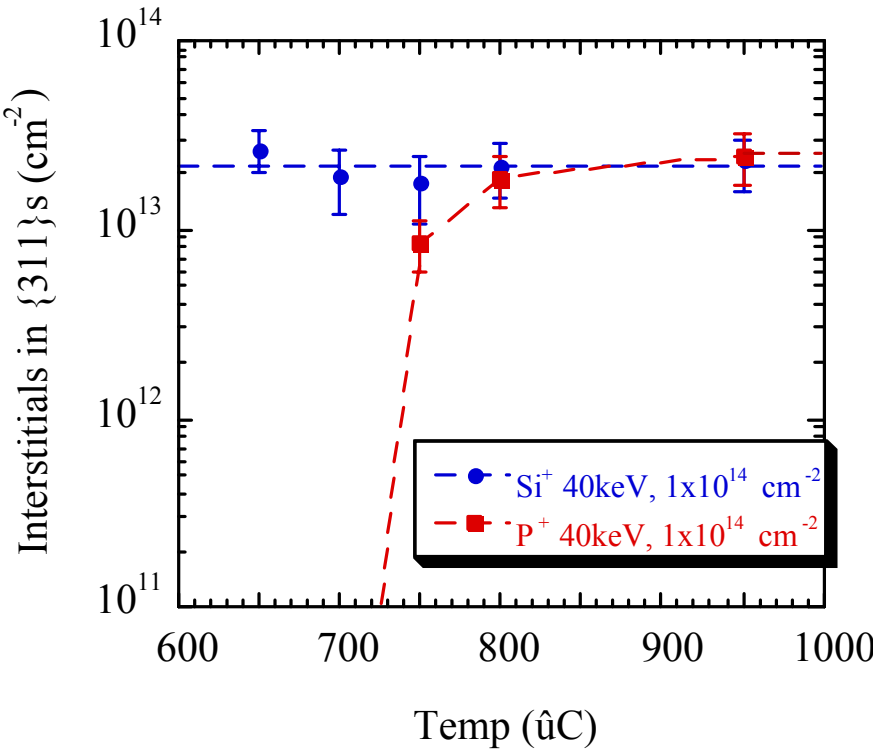

Figure 44. Temperature dependence of {311} defects due to 40keV Si^+ or P^+ $1.0x10^{14}$ cm^{-2} implants.

of {311} defects strongly correlates with the phosphorus concentration relative to the kink concentration (C_{enh}) at the given temperature.

Figure 45 shows C_{enh} at the given iso311 anneal temperatures superimposed on the as-implanted SIMS profile of the 40 keV, $1.0x10^{14}$ cm^{-2} phosphorus. The concentrations for C_{enh} were calculated from equation 13. At 950˚C, C_{enh} is above the peak of the implanted phosphorus. At this temperature the number of interstitials trapped in {311} defects was equivalent to the self-implanted sample. The number of interstitials trapped in {311} defects after the 800˚C anneal was slightly less than the self-implanted control samples. This is also the temperature at which the peak of the as-implanted phosphorus profile exceeds C_{enh}. As the temperature is reduced further the concentration

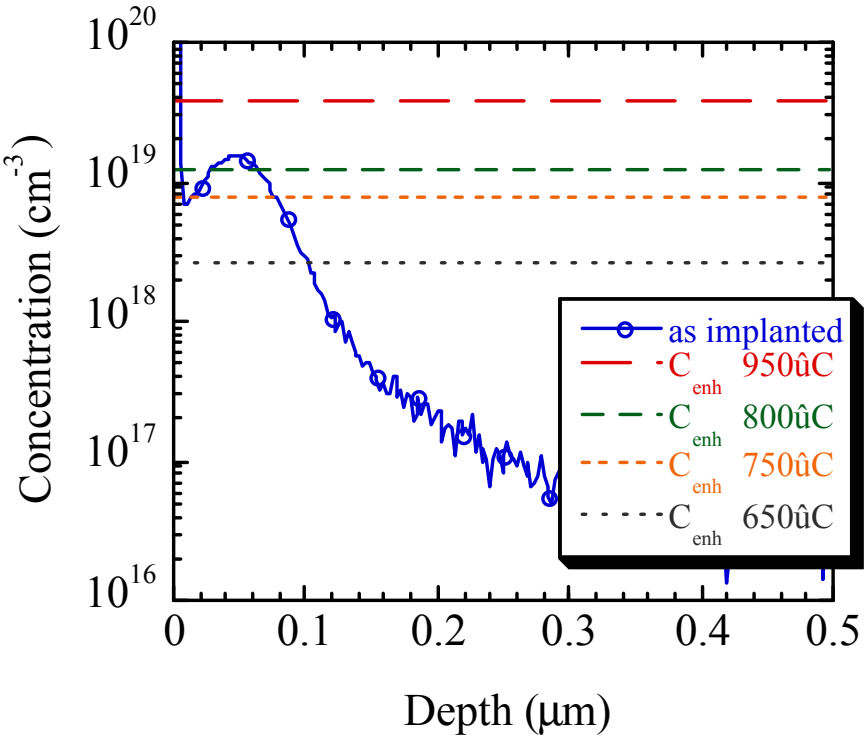

Figure 45. Kink concentration, C_{enh}, at several temperatures relative to the 40keV P^+ $1.0x10^{14}$ cm^{-2} implant profile.

of phosphorus in excess of C_{enh} increases. Likewise, the number of interstitials missing from {311} defects increases. By 650˚C when all the interstitials were depleted from {311} defects the peak of the as-implanted phosphorus profile far exceeds C_{enh}. This analysis indicates that the phosphorus in excess of C_{enh} captures interstitials during the earliest phase of annealing, prior to the nucleation of {311} defects.

Phosphorus Clustering and Electrical Activation

By observing the diffusion of the phosphorus profile at lower temperatures further understanding can be gained. Figure 46 shows the SIMS profiles of the 40keV phosphorus implanted to a dose of $1.0x10^{14}$ cm^{-2} after annealing at 700˚C for several

times. This sample contained no {311} defects. However, TED is still evident. As with the sample annealed at 750˚C there is a large amount of broadening in the junction depth and reduction of the peak concentration with increased annealing time. Unlike the 750˚C samples, the profiles are no longer gaussian in shape as they display a distinct kink at approximately 2.2×10^{18} cm^{-3}. This is more clearly evident at the shortest annealing times (15 and 30 minutes). Again, there is a large amount of dose lost to the SiO_2/Si interface as was observed for the samples annealed at 750˚C. The amount of dose lost increases with annealing time, resulting in a loss of approximately 50% at the longest annealing times.

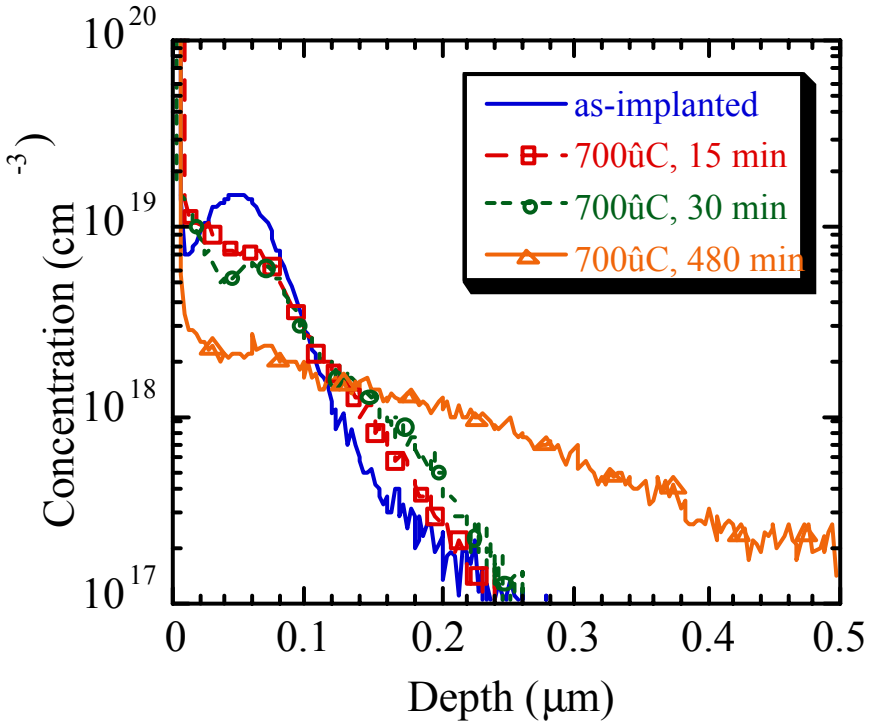

Figure 46. Phosphorus SIMS profiles after 700˚C anneals. Clustering is apparent in the peak region at shorter anneal times.

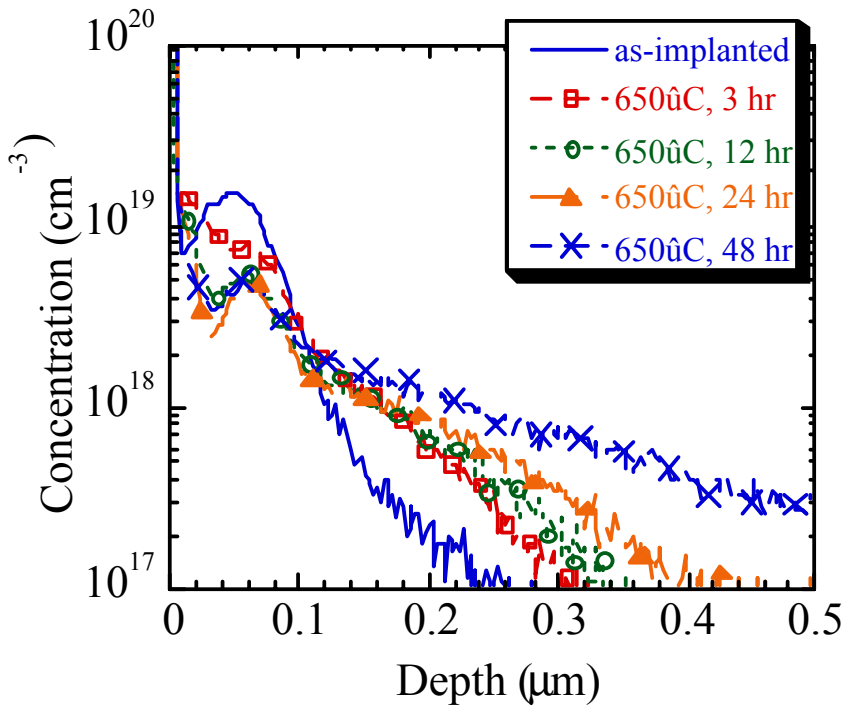

Figure 47. Phosphorus SIMS profiles after 650˚C anneals. Clustering is seen in the peak of the phosphorus profiles.

Similar behavior is observed for samples annealed at 650˚C as shown in Figure 47. Extended defects were not detectable in these samples using PTEM. The SIMS profiles display enhanced tail diffusion for long annealing times and a static peak portion. This peak decays with time as the gaussian tail diffuses deeper into the bulk. The exponential shape of the tail profile observed in the 48 hour annealed sample is believed to be due to sensitivity limitations of the SIMS technique used, not kick-out mediated diffusion. For all annealing times the kink in the profile occurs at a phosphorus concentration of approximately 1.5×10^{18} cm^{-3} at 650˚C.

SRP may be used to reveal if the static portions of the phosphorus profiles are electrically active. As shown in Figure 48 and Figure 49 for samples annealed at 700˚C

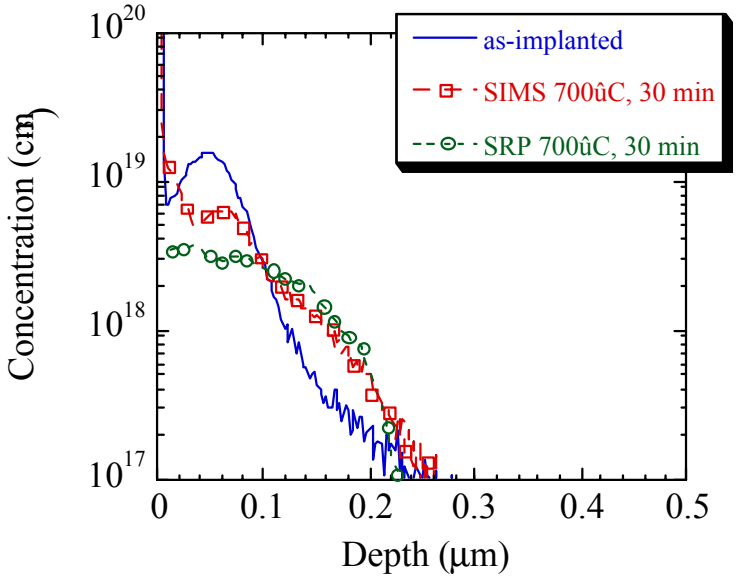

Figure 48. SIMS and SRP profiles for 40keV phosphorus implanted to a dose of 1.0×10^{14} cm^{-2} and annealed at 700˚C for 30 minutes. The clustered portion of the phosphorus profile is electrically inactive.

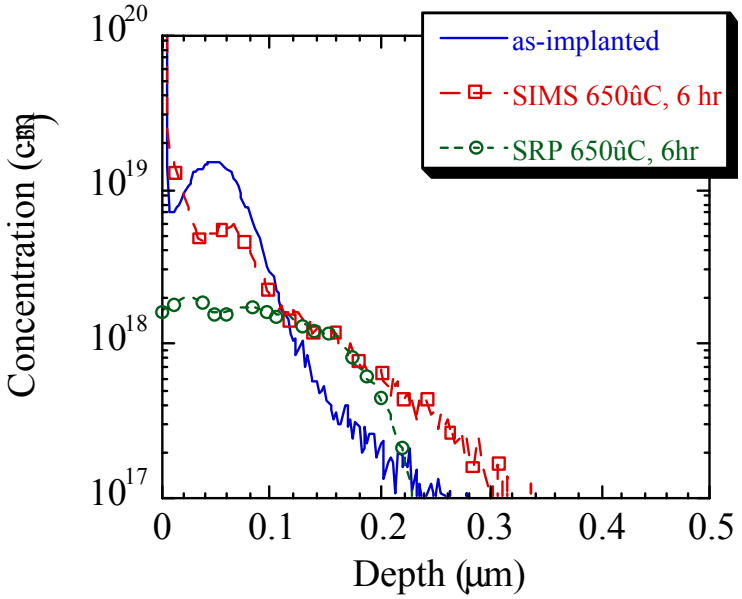

Figure 49. SIMS and SRP profiles 40keV phosphorus implanted to a dose of 1.0×10^{14} cm^{-2} and annealed at 650˚C for 6 hours.

and 650˚C, respectively, the SRP profiles are noticeably different than the SIMS profiles. While the SIMS profile give the entire chemical phosphorus profile, the SRP profiles show that only the gaussian tails of the profiles are electrically active. This suggests that the phosphorus in the static peak portion is clustered and the phosphorus in the gaussian tail portion is on substitutional sites. As with the kink concentration, the maximum concentration of active phosphorus is similarly temperature dependent. Although the end of the tail in the SRP profile of the 650˚C, 6 hour sample in Figure 49 appears to be electrically inactive, it is believed this is attributable to erroneous effects of the p-n junction space-charge region, not clustering. However, this would not account for the inactive peaks.

The transient nature of the electrically inactive cluster evolution at 650˚C is shown in Figure 50. The maximum concentration that is electrically active is higher at

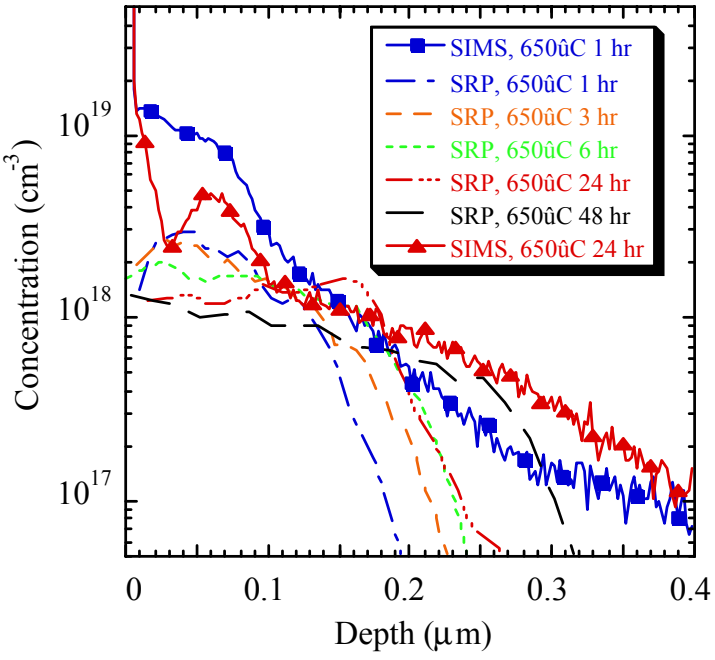

Figure 50. Time evolution of clustered phosphorus profile at 650˚C.

short annealing times, reaching almost $3.0x10^{18}$ cm^{-3} after just 1 hour. As the annealing time increases, the maximum concentration that is electrically active decreases and the junction depth increases. With longer anneal times at 650˚C the maximum active concentration stabilizes to approximately $1.5x10^{18}$ cm^{-3}. This is accompanied by diffusion of the phosphorus tail, suggesting that the dissolution of the clustered region is closely connected to the transient enhancement.

The dissolution of the clustered phosphorus and enhancement in the tail diffusion was analyzed by using a gaussian deconvolution technique to extract experimental rates. An example of the method used is given in Figure 51 for the sample annealed at 650˚C for 12 hours. First the tail of the SIMS profile was fit using a gaussian curve (equation B1) centered at the surface ($x_0 = 0$) with the dose, Q, and the square of the characteristic diffusion distance, Dt, as flexible parameters. From this the clustered portion of phosphorus was extracted by subtracting the tail fit from the whole SIMS profile. This

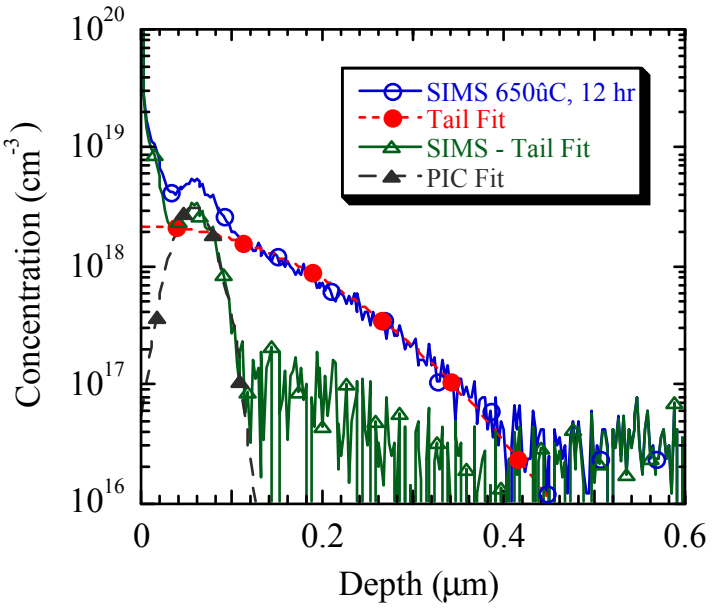

Figure 51. Gaussian curves used to fit phosphorus profile and extract the portion that is clustered.

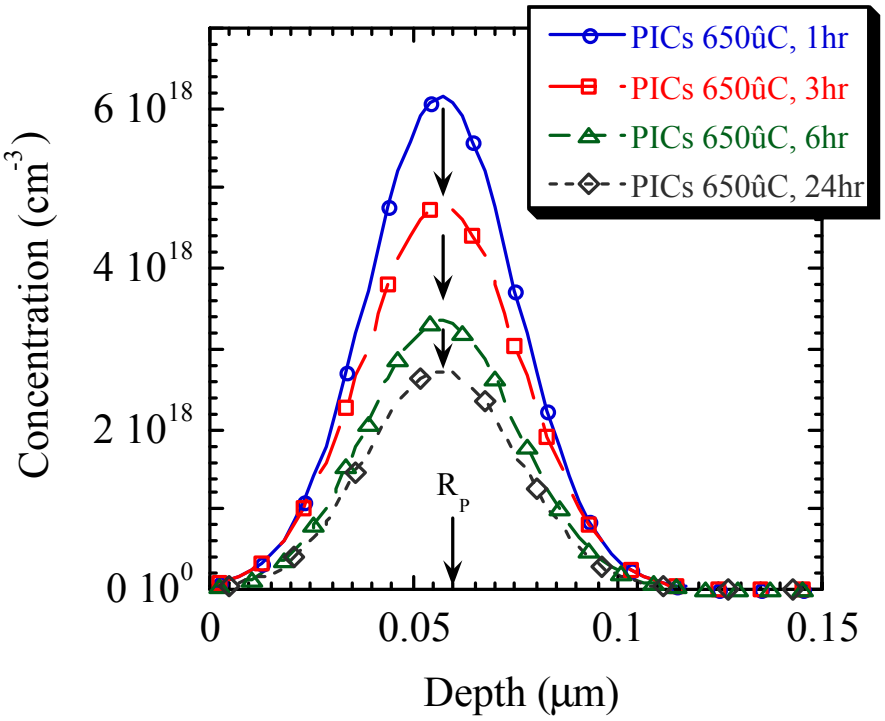

Figure 52. Experimentally extracted PIC profiles at 650˚C show dissolution over time.

resulted in a narrow gaussian distribution centered about the projected range as shown with open triangles in Figure 51 and the standard deviation between the tail fit beyond it. Another gaussian curve was fit to this clustered distribution representing the phosphorus contained in phosphorus-interstitial clusters (filled triangles in Figure 51) again using *Q* and *Dt* as flexible parameters. Although there is a significant amount of noise associated with the subtraction of two large numbers (SIMS - Tail fit) relatively accurate estimate of the clustered portion of phosphorus can still be obtained.

The resulting PIC profiles for several annealing times at 650˚C are shown in Figure 52. The clusters are centered about the projected range and decay in dose with annealing time. The PIC profiles show no signs of diffusional broadening. This is

confirmed in Figure 53 by plotting the *Q* and *Dt* extracted from the best fits as functions of time. The PIC dose is plotted on the left Y-axis and the square of the diffusion length on the right hand Y-axis. *Dt* remains constant for all annealing times at approximately $1.7\text{x}10^{-12}$ cm^{-2}. *Q* displays a transient dissolution with time. The dissolution of clustered phosphorus can analytically be expressed as a function of time using

$$Q(t) = Q_0 e^{-t/\tau_{PIC}} + Q_f \ [\text{cm}^{-2}] \qquad (16)$$

where Q_0 is the initial clustered dose, τ is the dissolution time constant in units of time and Q_f is the remaining clustered dose at long times. As the dissolution is yet to be completed at the longest experimental anneal time the dose of $5.7\text{x}10^{12}$ cm^{-2} is used to match the data. The extracted values for Q_0 and τ_{PIC} are $9.0\text{x}10^{12}$ cm^{-2} and $2.2\text{x}10^{4}$ sec

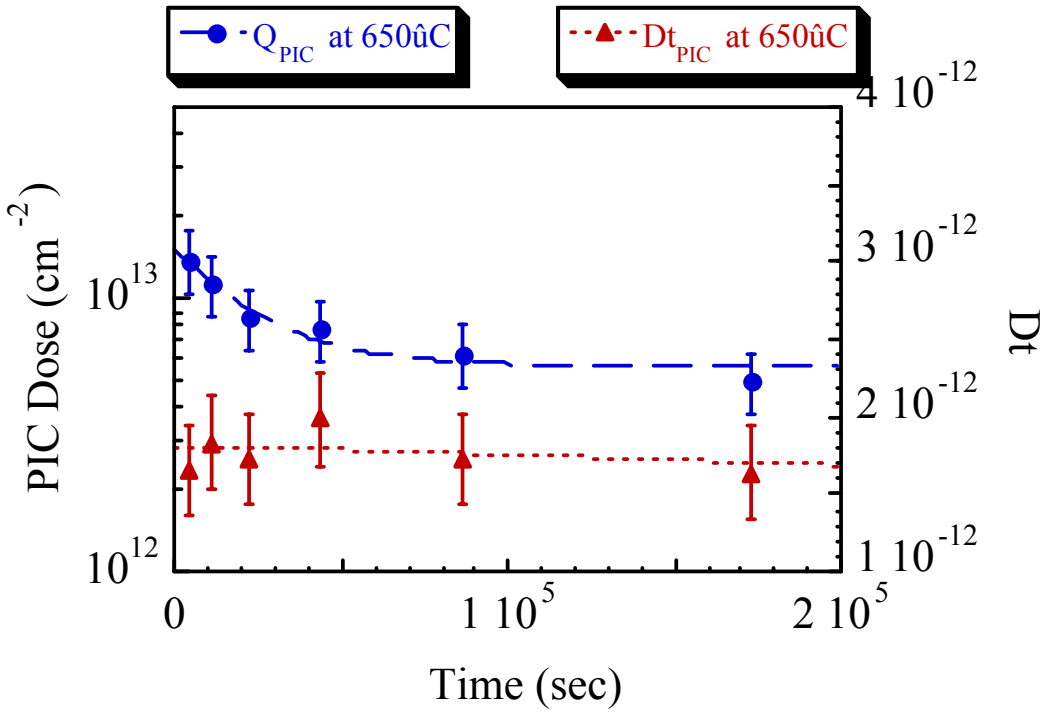

Figure 53. Dissolution occurs in the dose of clustered phosphorus but not the diffusion length at 650˚C. Decay of PIC dose is fit using equation 16.

(6.1 hours), respectively. The pre-exponential factor and the final PIC dose, Q_0+Q_f, is approximately $1.5\text{x}10^{13}\text{cm}^{-2}$, suggesting that the initial amount of cluster phosphorus is an order of magnitude less than the implanted dose. This suggests that the initial PICs may contain a high interstitial content. The PIC could evolve to more stable clusters at longer anealing times. The PICs are relatively stable at 650˚C as compared to 750˚C at which temperature the dissolution was already completed within 30 minutes.

The dissolution of clustered phosphorus extracted after 700˚C annealing is shown in Figure 54. The gradual decrease in clustered dose, Q, is fit using the exponential decay from equation 16. The best fit is obtained with $Q_0=6.1\text{x}10^{12}\text{cm}^{-2}$, $Q_f=1.3\text{x}10^{12}\text{cm}^{-2}$, and $\tau_{PIC}=7900\text{sec}$. The initial PIC dose ($Q_0+Q_f$) at 700˚C is approximately half of the that observed at 650˚C. As would be expected, the decay rate is much faster at 700˚C.

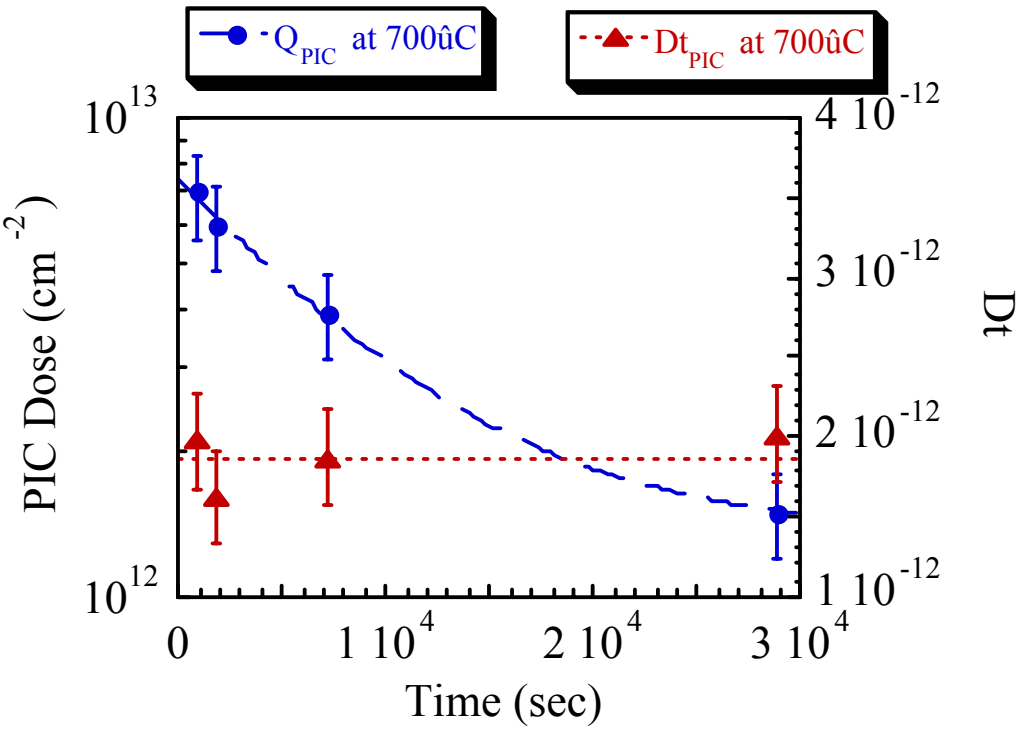

Figure 54. Dissolution of clustered phosphorus in 700˚C samples extracted using gaussian deconvolution. Decay in clustered dose is fit to an exponential decay.

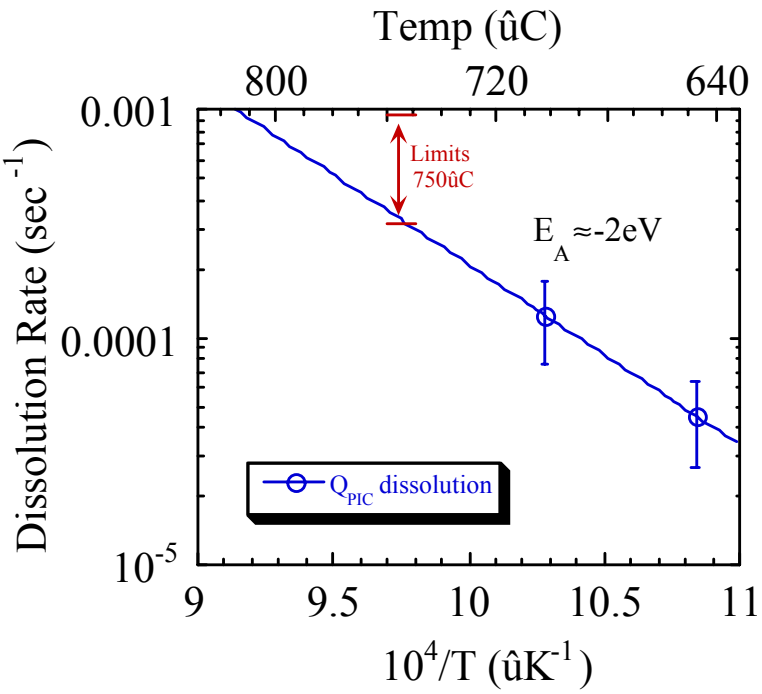

Figure 55. Arrhenius dependence of the clustered phosphorus dissolution rates.

An arrhenius plot of the extracted dissolution rates ($1/\tau_{PIC}$) as shown in Figure 55 yields a rough estimate of the activation energy for this process. Close inspection of the samples annealed at 750˚C for the shortest times reveals that some clustering is evident in the peak, $Q \approx 3.3 \times 10^{12} cm^{-2}$ at 15 minutes. By 30 minutes, the clustering is below the detectable limits of the gaussian deconvolution method. While the dissolution rate could not be extracted at 750˚C, approximate upper and lower bounds can be imposed from the information gathered assuming Q_0 is $6.0 \times 10^{12} cm^{-3}$ or less. These are shown to be slightly above the extrapolated dissolution rate in Figure 55. Although the reliability of the exact arrhenius energy is limited due to the low number of data points, a rough estimate of approximately 2eV may be associated to this process.

Another significant effect that was previously mentioned is the loss of implanted dose to the single monolayer of the Si/SiO_2 interface. The transient nature of this process is investigated after isothermal annealing of the samples implanted with 40keV phosphorus ions to a dose of $1.0x10^{14}cm^{-2}$. The dose retained in the silicon was obtained by integrating the phosphorus SIMS profiles assuming that the apparent peak in surface of the profile occurs when the primary ion beam sputters through the interfacial spike of dose [Gri95]. The transient nature of this process is clearly demonstrated in Figure 56. The amount of dose being lost to the surface exponentially decreases with time, confirming that it is a diffusion limited process that is exacerbated by TED. The total dopant lost after TED has completed slightly increases with decreasing temperature.

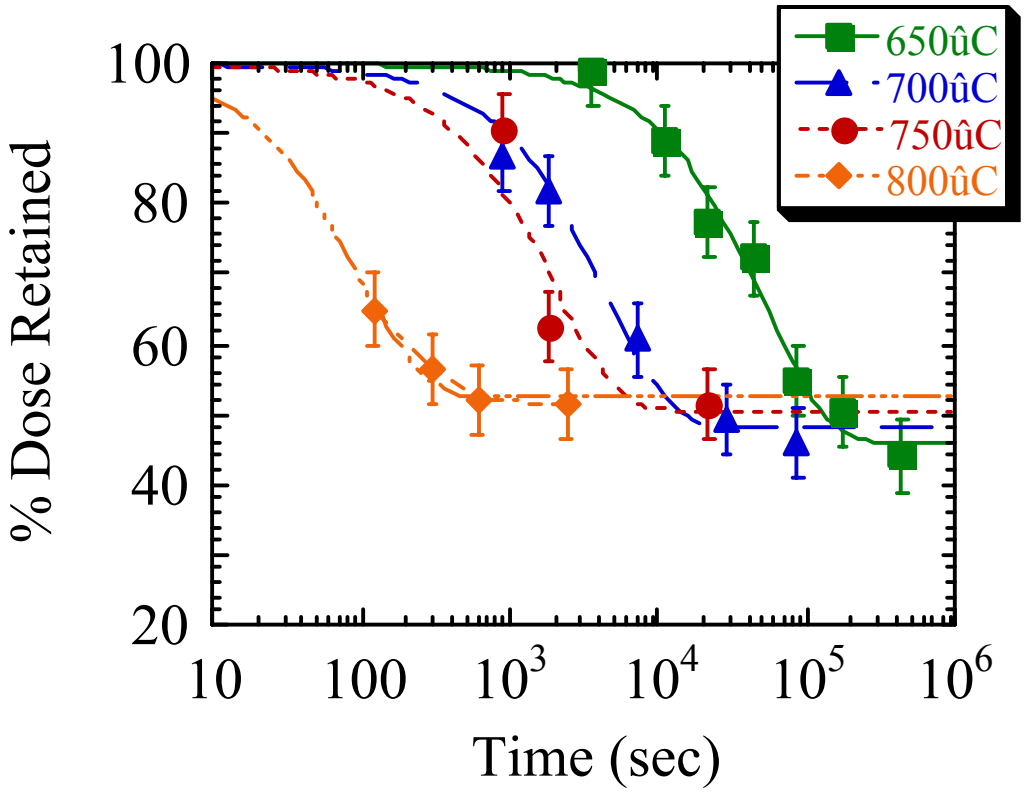

Figure 56. Transient nature of the dose loss process for 40keV P^+ implants with a dose of $1.0x10^{14}cm^{-2}$ and isothermally annealed between 650-800˚C.

Discussion

Results from this analysis of 40keV phosphorus implants with a dose of $1.0x10^{14}$ cm^{-2} indicate that the concentration of phosphorus in excess of the kink concentration captures interstitials during the earliest stages of damage recovery prior to the nucleation of {311} defects. These phosphorus-interstitial clusters are electrically inactive as confirmed by SRP and non-diffusive, only dissolving with time.

This can be extended to the 10-100keV range for further support. Table 6 summarizes the type of extended defects that form after 5 minutes of annealing at 750˚C for 10-100keV phosphorus implants using a dose of $1.0x10^{14}$ cm^{-2} [Des97]. Small dot defects were classified as loops in that study. Also, the amount of interstitials in {311} defects was much less in the 50 keV implanted sample than in the 100 keV implanted sample. Identical conditions using Si^+ implants would produce {311} defects for all samples in this dose and energy range. Comparison of 100keVP^+ and Si^+ implants with a dose of $1.0x10^{14}$ cm^{-2} showed that the total interstitial concentration trapped in extended defects was less for P^+ implanted samples than Si^+ implanted samples [Li99].

The correlation of interstitial trapping and phosphorus kink concentration can be easily applied to these experimental conditions as a test. By comparing the as-implanted profiles to the kink concentration for the conditions of Table 6 the energy range may be

Table 6. Extended defects for $1.0x10^{14}$ cm^{-2} dose phosphorus implants with 10keV - 100keV energies

	Extended Defects (1x10 ^{14} cm^{-2} P^+ implant; annea l 750ÞC,5 min)			
Energy ý	10 keV	30 keV	50keV	100keV
De fects ý	None	Loops	Loops & {311}	Loops & {311}

Source [Des97]

expanded. The approximate as-implanted phosphorus profiles are recreated in Figure 57 with a simple gaussian function using projected range and straggle values determined by LSS theory [Lin63]. This approximation is applied with a relatively high confidence level for the implant conditions used. At 750˚C C_{enh} is slightly below the peak of the 100 keV as-implanted profile. As the energy is reduced, the peak concentrations of the as-implanted profiles increase well beyond C_{enh}. This results in the concomitant reduction of interstitials in extended defects as described in Table 6.

Diffusion studies of these implant conditions could further confirm the clustering behavior, however, the PICs may be very unstable at higher temperatures resulting in rapid dissolution. Still, as a rule of thumb to determine if interstitial trapping is going to

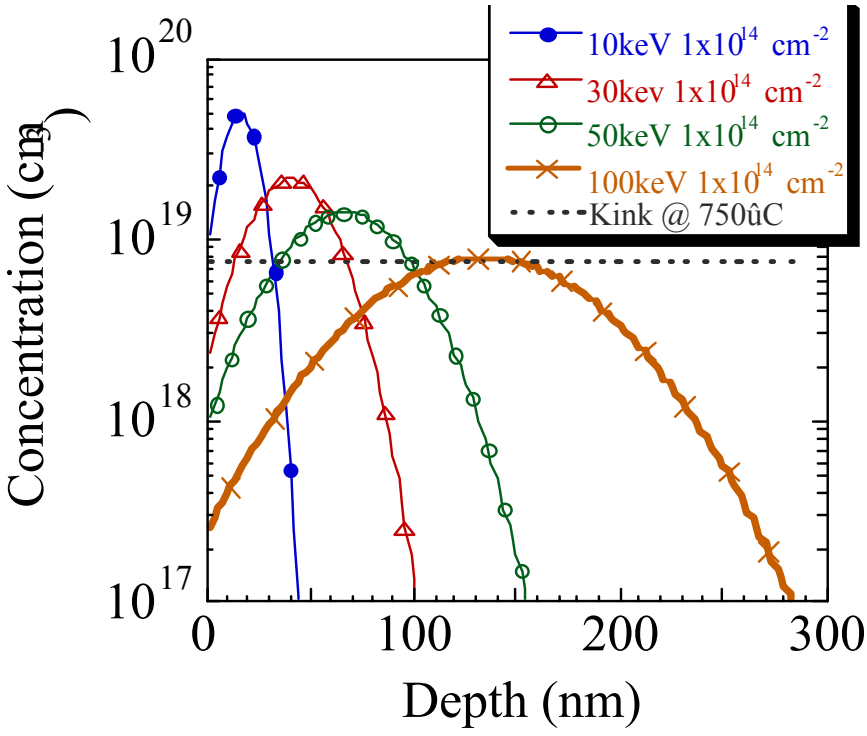

Figure 57. Approximate implant profiles (gaussian) for 1.0×10^{14} cm^{-2} phosphorus ions implanted with 10keV - 100keV energies and phosphorus kink concentration at 750˚C.

occur during the annealing of non-amorphizing phosphorus implants at a given temperature the peak concentration should be compared to C_{enh}. A rough estimate of

$$N_{\max} = 0.4Q/\Delta R_P \qquad (17)$$

may be used with Q being the implant dose and ΔR_P being the straggle.

In such cases when the peak concentration exceed C_{enh} the amount of interstitials in imageable extended defects will decrease. This implies that the interstitials are incorporated in clusters of atoms too small to create strain fields that can be detected with conventional TEM methods, making the determination of the exact configuration of these clusters difficult. Schematically, the clustering process is considered in Figure 58. In the absence of phosphorus and at significantly low concentrations extrinsic defect can freely agglomerate during annealing (left side of Figure 58). However, as the phosphorus concentration is significantly increased beyond C_{enh} at the given annealing temperature the free interstitials that are created during the implant get trapped by the phosphorus (right side of Figure 58). This reduces the number of excess interstitials that condense to form extended defects. Furthermore, the phosphorus that is incorporated in the PICs is not able to participate in the diffusion and electrical conduction processes. Formation of

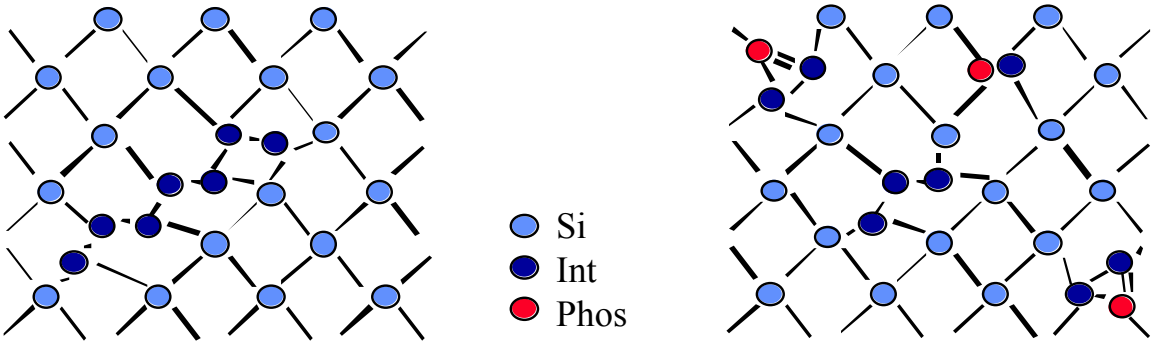

Figure 58. Phophorus-interstitial clustering: (Left) excess interstitials form {311} defects in absence of phosphorus; (Right) excess interstitials are captured by PICs, thus reducing the amount of interstitials available for {311} defects.

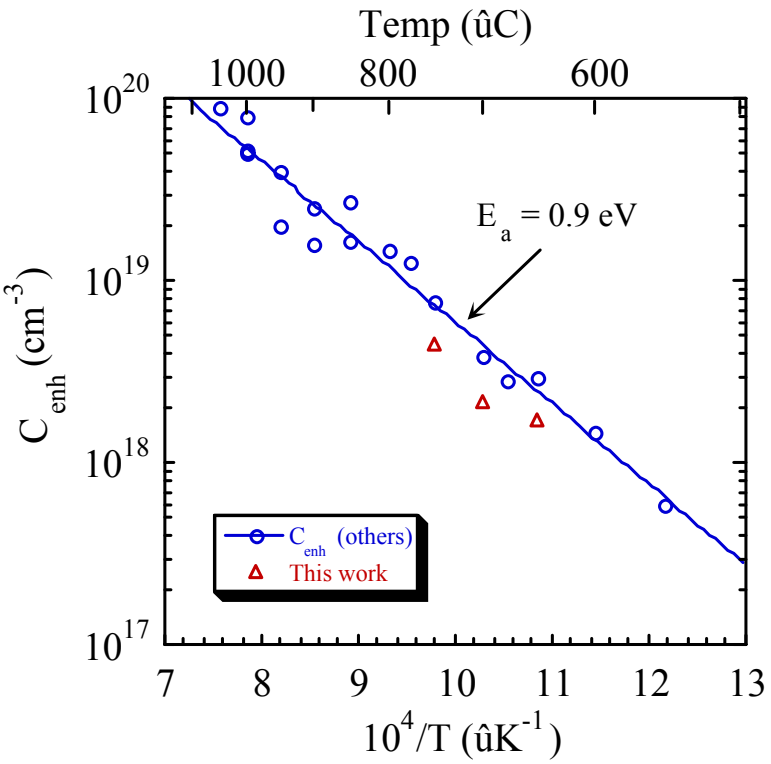

Figure 59. Kink concentration from this work and those previously reported by other researchers.

these clusters requires a sufficiently large amount of interstitials as this clustering process is only observed under nonequilibrium conditions. It is conceivable that the PICs may start as interstitial-rich clusters and gradually release interstitials as they evolve to more stable phosphorus-rich clusters.

Finally, it is worth comparing the kink concentration observed in this experimental work with those of previously reported experiments [Sch72, Mas77, Oeh84, Ang87, and Fai90]. Values extracted from the SIMS profiles when clustering was observable are included on the arrhenius plot in Figure 59. The concentrations from this experimental work are represented with open triangles and values from other researchers with open circles. Although the data from this experiment are lower than those

previously reported, they are in relatively close agreement and display an identical arrhenius dependence. As there are only single data points for comparison at the temperatures used in this experiment it is difficult to determine which values are more precise. Also, there may be some inherent deviation in C_{enh} due to wafer material and processing methods used as is common for intrinsic defect properties.

Summary

In summary, extended defects were not present after low dose implants during this experiment. Without extended defects the release of interstitials exhibited no transient nature. As defects form at higher doses the enhancement becomes transient.

In silicon implanted samples the excess interstitials are incorporated in {311} defects, accounting for TED. The number of interstitials trapped in dot defects after phosphorus implantation does not account for all the interstitials released during TED. Furthermore, a high percentage of the interstitials trapped in dot defects remain captured in dislocation loops after TED is completed. However, it is interesting to note that the dissolution of dot defects occurs at approximately the same time as TED saturates. This suggests that the environment surrounding the dot defects causes the defects to become unstable as the point defect concentration approaches equilibrium levels. Loops larger than an undetermined critical radius are stable enough to remain.

The missing interstitials are believed to be incorporated in immobile and electrically inactive clusters as supported by the experimental results. There is a definite temperature dependence of cluster formation and dissolution. For the implant conditions investigated, the cluster formation occurs in interstitially supersaturated environments when the phosphorus concentration exceeds C_{enh}. The PICs are stable at low annealing

temperatures, dissolving along the same time-scale that TED takes place. The atomic configuration of these clusters is currently undetermined. It is likely that the clusters evolve from small interstitial-rich clusters to more stable phosphorus-rich clusters at longer annealing times.

CHAPTER 5
PHOSPHORUS DIFFUSION SIMULATIONS

In the prior two chapters, the physics of phosphorus-defect interactions were experimentally investigated. This chapter will focus on the simulation and modeling of phosphorus-defect mediated diffusion.

Diffusion models in FLOOPS

Modeling diffusion has become essential to predicting dopant profiles for modern device structures. As discussed in chapter two, the diffusion of dopant atoms is controlled by the reactions with point defects. In this work, diffusion is modeled using a set of partial differential equations to describe the reactions that are numerically solved using FLOOPS. Dopant diffusion simulations will use the five-stream model, referred to in FLOOPS as the "React" model to take into account dynamic pairing. In addition to simple point defects, when modeling diffusion after implantation, one must also include extended defect clusters such as {311} defects to account for transient enhanced diffusion.

Si-Cluster models

Models to describe the evolution of {311} defects cover a wide range of complexity, from a simple solubility approximation [Cha96], to solving rate equations of multiple moment-based models [Raf96, Law96b, Gen97, Hob99]. While the single moment model [Raf96], containing only information about the concentration of interstitials contained in the {311} defects, seems to accurately explain the most apparent

features of TED associated with {311} defects, it does not take into account the small self-interstitial cluster-precursors that form prior to {311} defect nucleation. Modeling of these smaller self-interstitial clusters is necessary for matching the ultrafast TED supersaturation associated with post-implantation annealing [Cow94, Cow99]. As the interaction of phosphorus and self-interstitials has been shown to be most important during this early stage of damage recovery, a Si-cluster model which takes into account the smaller self-interstitial clusters was implemented in FLOOPS. This continuum model is similar to the Monte Carlo-based model developed by Cowern *et al.* [Cow99] and is used for all simulations described in this chapter.

The Si-cluster model accounts for di-interstitials (I_2), sub-microscopic interstitial clusters (SMICs) of sizes 3 interstitials (I_3) through 10 interstitials (I_{10}), and {311} defects (clusters greater than 10 atoms large). The concentration of interstitials in each cluster of size *n* is governed by

$$\frac{\partial C_n}{\partial t} = K_{f_n} C_I C_{n-1} - K_{r_n} C_n \exp\left(-\frac{E_{b_n}}{k_B T}\right) \qquad (18)$$

where K_f and K_r are the rates for forward and reverse clustering reactions, respectively, C_I is the interstitial concentration, k_B is the Boltzmann constant, T is the annealing temperature, and E_b is the binding energy of the cluster. In their study, Cowern *et al* used $D_I C_I^*$ equivalent to 4.52 eV [Cow99]. The simulations performed in this chapter use interstitial parameters taken from Bracht *et al.* that result in $D_I C_I^*$ of 4.95eV [Bra94, Bra95]. The cluster energetic parameters were converted to match the interstitial parameters used. Using the converted cluster parameters in the continuum-based FLOOPS model to simulate the experimental conditions reported by Cowern *et al.* provides close correlation to the early transient supersaturation as shown in Figure 60.

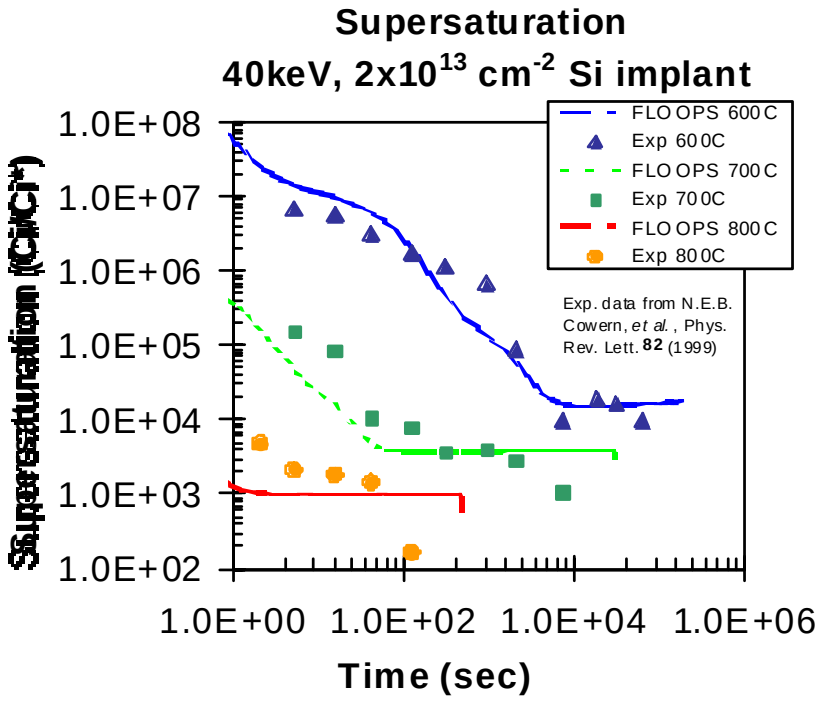

Figure 60. Interstitial supersaturations simulated using the higher order Si cluster model show strong agreement with experimental data.

The large supersaturations observed at early annealing times are attributed to the smaller cluster precursors. The kinetic transition of smaller cluster sizes to larger clusters is shown in Figure 61 for di-interstitials, I_4 clusters, I_8 clusters, and {311} defects. At early annealing times, the excess interstitials are incorporated in di-interstitials and I_4 clusters. At longer annealing times the larger I_8 clusters and {311} defects capture excess interstitials at the expense of di-interstitials and I_4 clusters. Eventually, the I_4 clusters and I_8 clusters completely dissolve yielding interstitials for incorporation in {311} defects. The {311} defects then control the supersaturation of interstitials that sustain TED for longer annealing times.

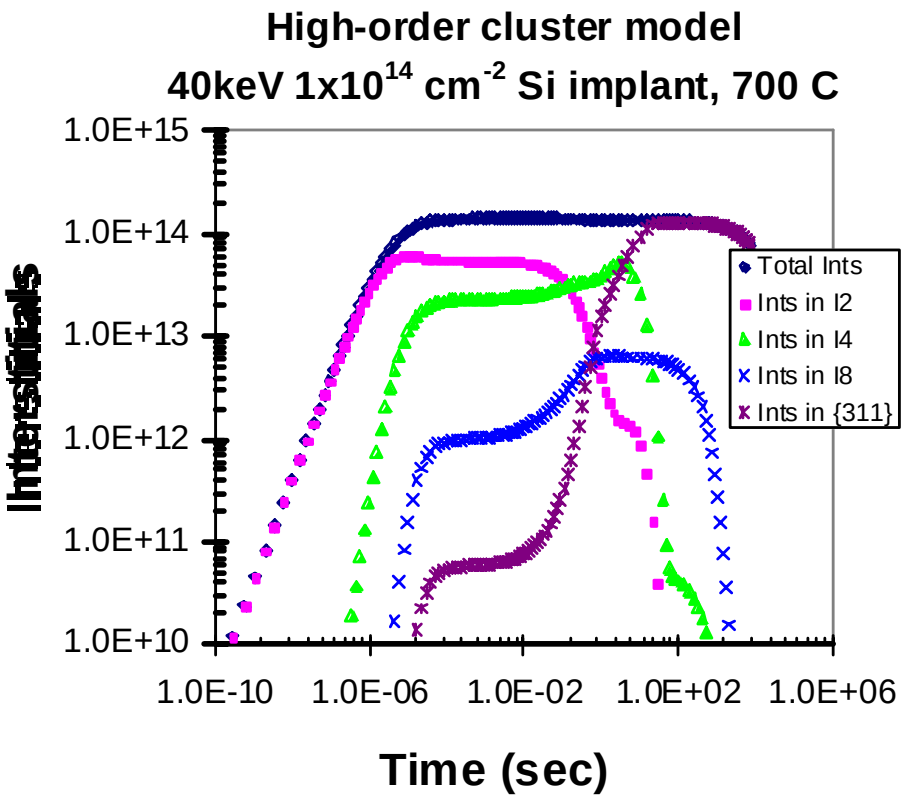

Figure 61. Simulated cluster concentrations shows kinetic transition to larger clusters with time.

The Si-cluster model was also tested against the experimental results for the self-interstitial implant work from chapter four of this study. Simulations of the boron spike enhancements and the quantity of interstitials trapped in {311} defects provides close agreement with experimental results over the entire experimental range used. Figure 62 shows the buried boron spike enhancements resulting from 40 keV Si^+ implants using a dose of $1.0x10^{14}$ cm^{-2} after annealing at 650˚C for several times. Simulation of the enhanced boron spike diffusion (lines) is closely matched to experimental results (symbols) at both short and long annealing times. Figure 63 compares the simulated defect dissolution to the quantified experimental results for 40 keV Si^+ ions implanted

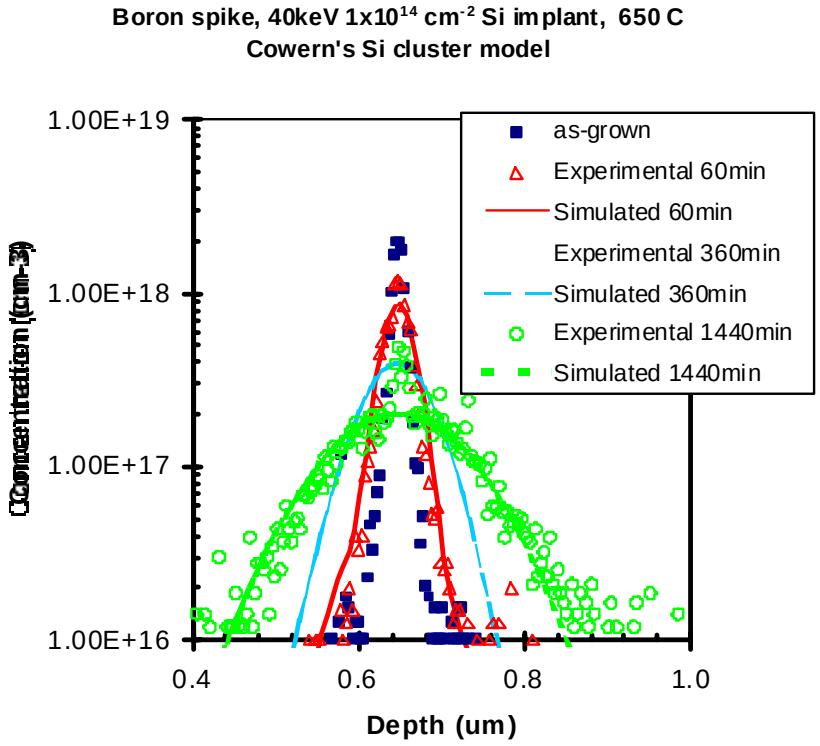

Figure 62. Simulated boron spike diffusion enhancements match experimental data using the Si cluster model.

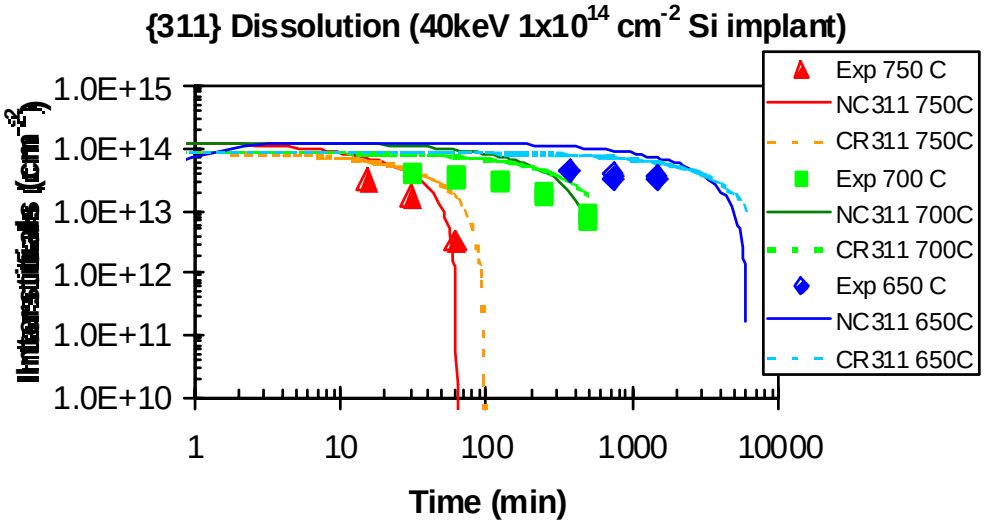

Figure 63. Dissolution of {311} defects using single moment cluster model and higher order Si cluster model that accounts for precursor clusters.

to a dose of $1.0x10^{14}$ cm^{-2} and annealed at several temperatures. The transient decay in the amount of interstitials trapped in {311} defects is closely approximated by the simulations. Similarly, the temperature dependence of dissolution is also closely captured in the simulations. These results confirm that the Si-cluster model can accurately simulate the behavior of self-interstitials in the direct absence of dopants and should be adequate for modeling TED of dopants.

Annealing of the 40keV P^+ implants with a dose of $1.0x10^{14}$ cm^{-2} was simulated using the Si^+ cluster model. The excess interstitials generated by the implant were allowed to form clusters and the implanted phosphorus became substitutional, until pairing with free interstitials and diffusing. The resulting phosphorus profiles of

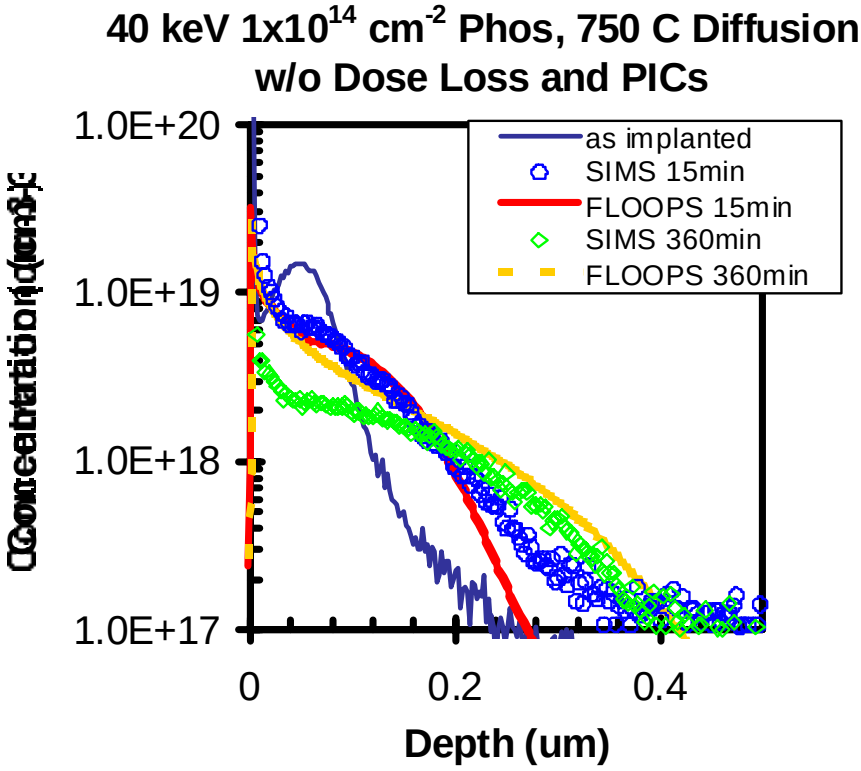

Figure 64. Phosphorus diffusion simulations using Si-cluster model at 750˚C shows reasonable agreement with SIMS. Note the loss of dose in SIMS samples is not accounted for in the simulations.

simulations performed at 750˚C for 15 minutes and 360 minutes are shown in Figure 64. There is reasonable agreement between simulated and experimental results at 15 minutes. However, the results after 360 minutes are much different as there is a significantly higher dose contained in the simulated profile. Clearly the dose lost to the interfacial layer needs to be taken into account.

Phosphorus Dose Loss Models

A significant portion of the implanted phosphorus dose can be lost to the surface [Gri95, Sat99]. The timescale of this dose loss process [Sat97] is proportional to the TED timescale and the magnitude of the loss is higher at lower annealing temperatures similar to TED. A simple model is used to account for this dose loss assuming that every phosphorus atom the reaches the interface sticks. The flux at the interface is described as

$$Flux = -K_{surf} \times C_{Pi} \qquad (19)$$

where K_{surf} is the surface recombination rate for phosphorus, and C_{Pi} is the concentration of Phosphorus interstitials reaching the interface. This model will not take into account that the amount of traps at the interface can be filled under very large doses. However, under the experimental conditions investigated this approximation should be valid (i.e.- not valid for higher doses). Furthermore, it also assumed that K_{surf} is large enough that the reaction is diffusion-limited by the amount of phosphorus interstitials reaching the interface. Results for the 40 keV phosphorus implanted to a dose of $1x10^{14}$ cm^{-2} and annealed at 750˚C for 360 minutes are shown in Figure 65 with and without using the dose loss model. Use of the dose loss model results in improved fits in both the surface and tail regions of the phosphorus profile. By assuming that the dose loss is diffusion-limited, the transient nature of the dose loss is captured as shown in Figure 66. This

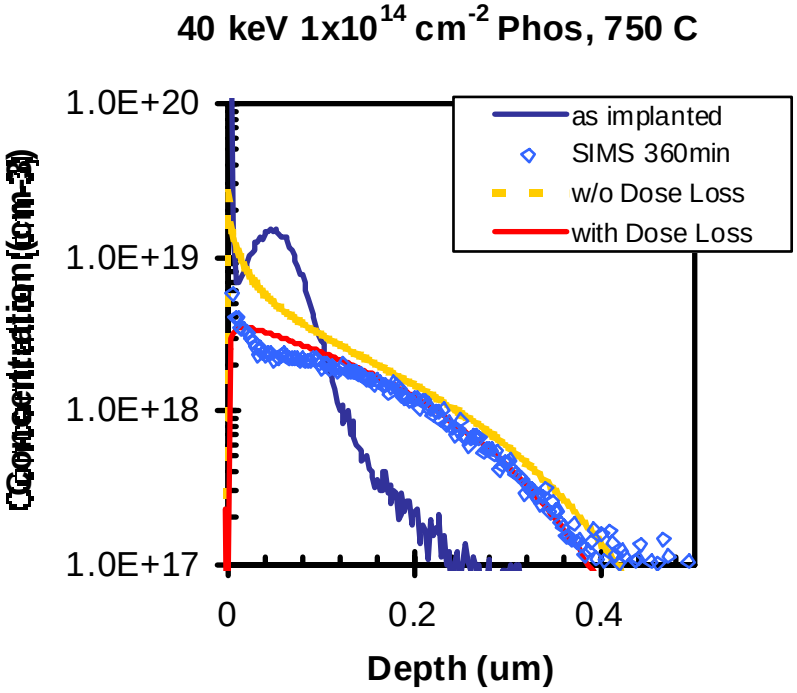

Figure 65. Simulations using dose loss model show improved fit 750˚C.

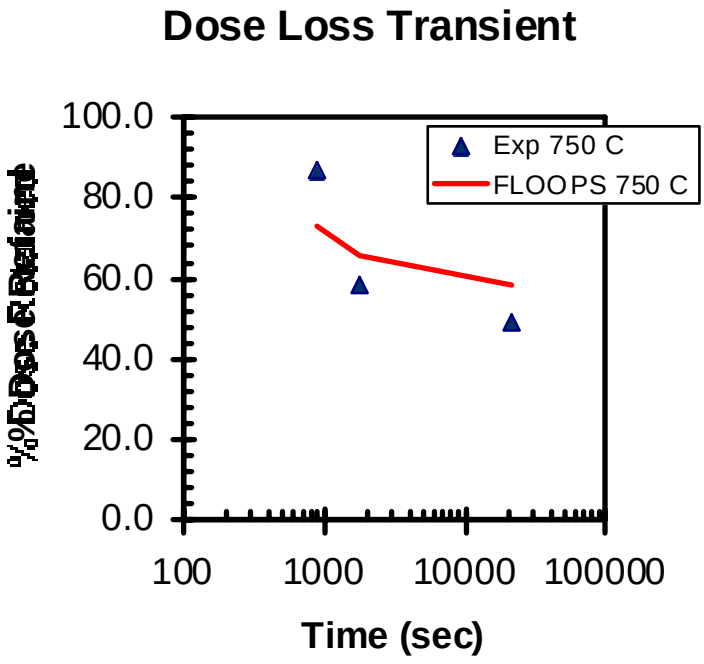

Figure 66. Retained dose decays with time. Dose loss model captures transient nature.

confirms the fact that phosphorus dose loss is magnified by TED as it is a diffusion limited reaction at the interface. Thus, high temperature annealing reduces the amount of dose loss as it reduces the overall magnitude of TED [Gri95].

Results of the 40 keV, $1.0x10^{14}cm^{-2}$ dose phosphorus diffusion simulations show reasonable agreement with experimental results for samples annealed at 750˚C and above. However, at lower annealing temperatures the formation of PICs must also be accounted for as shown in Figure 67. In this case, 650˚C anneal for 720 minutes, the simulation does not predict the significant portion of the phosphorus profile that is electrically inactive and inaccurately reproduces the overall phosphorus profile.

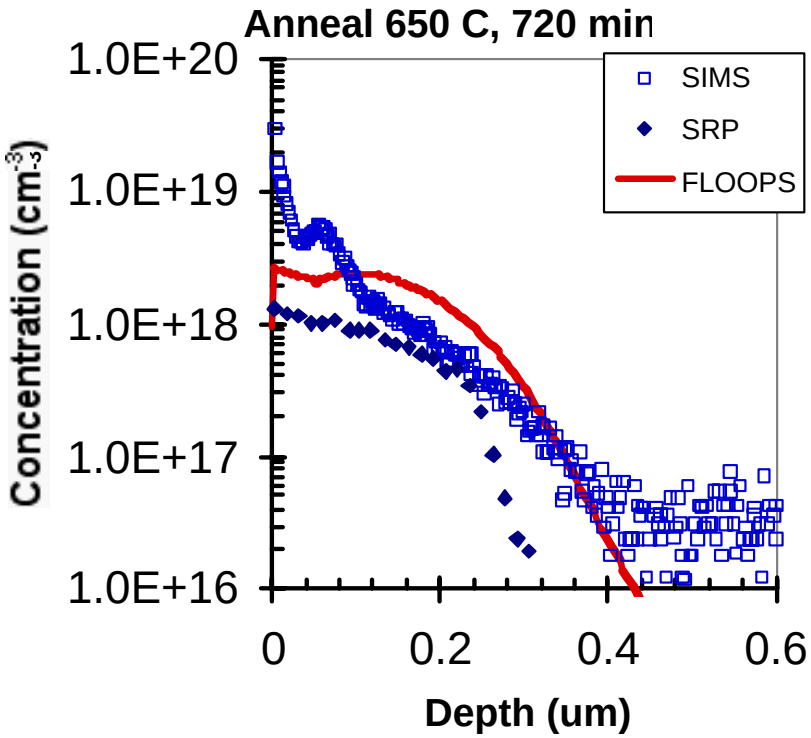

Figure 67. Simulations using the Si-cluster model do not fit at lower temperatures when phosphorus clustering occurs.

Phosphorus-Interstitial Cluster Models

As the exact content and configurations of the clusters are not known a generic cluster model is used. The formation and dissolution of PICs can be accounted for by including a clustering reaction using the equation

$$\frac{\partial[P_n I_m]}{\partial t} = K_f[P_{act}]^n[I]^m - K_r[P_n I_m] \qquad (20)$$

where $[P_nI_m]$ is the concentration of clusters containing n atoms of phosphorus and m interstitials, $[P_{act}]$ is the active phosphorus concentration, $[I]$ is the interstitial concentration, and K_f and K_r are the forward and reverse clustering rates, respectively.

The first term on the right hand side accounts for the formation of clusters, or the forward reaction. The cluster growth is proportional to the active phosphorus concentration raised to the power n and the interstitial concentration raised to the power m. Thus, the forward reaction of PICs mandates that both the interstitial active phosphorus concentration be sufficiently large. The overall abruptness of PIC profiles are controlled by the powers, n and m. The forward rate of the formation reaction, K_f, is typically assumed to be diffusion limited. The last term on the right hand side of equation 20 controls the dissolution of the clusters. Typically, this term has a binding energy associated with the reverse rate, K_r, which represents that the break up of clusters is a rate limited process. The consumption and release of interstitials and phosphorus atoms is coupled to the time dependent differential equations governing interstitials and phosphorus, respectively.

Several different cluster configurations were investigated, with the P_3I_2 yielding the best results. The optimum rates, K_f and K_r, were obtained by fitting the simulation to experimental results for two individual annealing times at two temperatures. The rates

Table 7. Forward and reverse reaction rates for PIC model

Temperature (˚C)	K_f (cm^{12}/sec)	K_r (sec^{-1})
600	2.5x10^{-71}	7.1x10^{-7}
650	1.0x10^{-70}	1.5x10^{-5}
700	3.5x10^{-70}	2.3x10^{-4}
750	1.1x10^{-69}	2.7x10^{-3}
800	3.0x10^{-69}	2.5x10^{-2}

were expanded to several temperatures as given in Table 7 assuming an arrhenius dependence. The arrhenius rate equations are

$$K_f = 3.9\times10^{-60}\exp\left(-1.94/kT\right)\ [\text{cm}^{12}/\text{sec}] \qquad (21a)$$

$$K_f = 1.8\times10^{-18}\exp\left(-4.23/kT\right)\ [\text{sec}^{-1}] \qquad (21b)$$

Using this single set of parameters, the simulated results provided an improved match to experimental data over several times and temperatures. Examples showing the improved accuracy are shown in Figure 68 and Figure 69. In Figure 68 the simulated profiles resulting with and without using the PIC model are compared to the experimental SIMS profile after 12 hours of annealing at 650˚C. The profile predicted by the model that takes into account PIC formation fits the SIMS results much better. With the use of the PIC model, the kink and tail of the profile are accurately reproduced. The clustered portion in the peak of the simulated profile is slightly overestimated. This model still predicts that {311} defects will form, however, the amount is significantly reduced as many of the excess interstitials are incorporated in PICs.

Figure 69 shows the SIMS profile after 700 ˚C annealing for 30 minutes and the simulated profile using the PIC model. Again the simulated diffusion fits the experimental results nicely in the kink and tail portion of the profile with slight

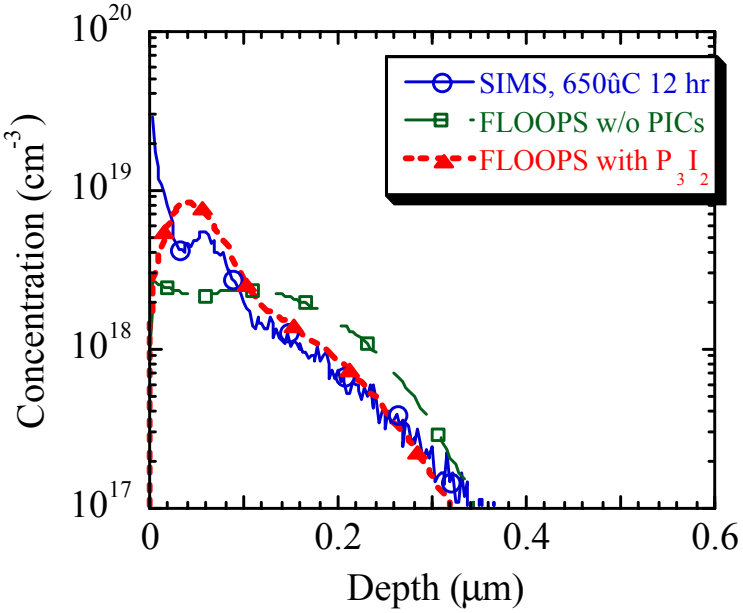

Figure 68. Simulations at 650˚C provide better fit using the PIC model.

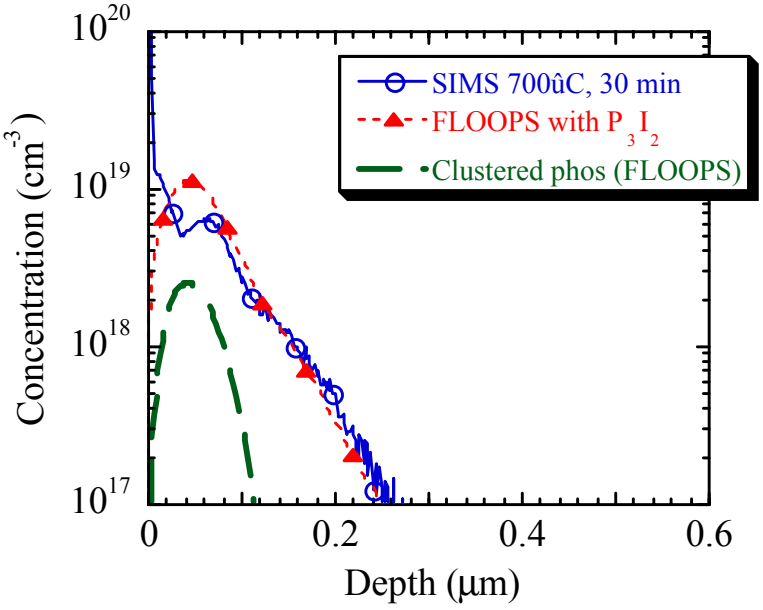

Figure 69. Phosphorus diffusion at 700˚C for 30min (simulations and data). Simulated portion of clustered phosphorus is also included.

overestimation in the clustered peak portion. The portion of phosphorus that is clustered as predicted by the simulations is also shown. If the clustered portion is assumed to be electrically active, as was experimentally shown, the active phosphorus profile fits well with the experimental results. Thus, although the clustering is slightly overestimated, prediction of the electrically active profile is still accurate and vastly improved.

Summary

Work in this chapter showed that the diffusion of non-amorphizing phosphorus implants can be modeled to predict electrically active concentrations and junction depths. Three vital components must be taken into account: 1) Si clusters, 2) dose loss, and 3) phosphorus-interstitial clusters. All of these aspects can be modeled by adding equations to the five-stream diffusion model. Si-cluster modeling controls the behavior of the excess interstitials that dominate TED. The loss of dopant to the SiO_2/Si interfacial layer can easily be accounted for by including a diffusion-limited reaction of phosphorus-interstitial pairs at the interface. This component of the model correctly links the dose loss to TED as was shown to experimentally occur [Gri95]. The third component, clustering of phosphorus with interstitials, can be modeled using a generic dopant-cluster equation. This controls the amount of phosphorus that is unable to contribute to diffusion and electrical activity. Incorporation of all three components of this model were shown to provide improved accuracy to process simulators.

CHAPTER 6
SUMMARY AND FUTURE RECOMMENDATIONS

Dopant-defect interactions are recognized as an important effect that needs to be understood for efficient processing and modeling of IC devices. This thesis has sought to understand these interactions through the use of clever experimental observations and advance the predictive capabilities of TCAD simulators by developing better defect mediated diffusion models. In this final chapter, contributions made in this thesis will be reviewed and some recommendations for areas that may warrant further investigation will be given.

Synopsis of Results

Due to its nonconservative nature, the ion implantation process leaves the silicon crystal in a highly nonequilibrium state. Subsequent thermal annealing of the implant damage can result in the detrimental consequences of TED, incomplete dopant activation, and extended defect formation. A thorough understanding of the complex physical interactions between dopant atoms and point defects is vital for continued device scaling and performance improvements. A novel set of experiments using phosphorus doped wells and direct phosphorus implants was developed and resulted in significantly increasing present understandings. Data was extracted from the experimental results for use in continuum-based diffusion simulation tools to accurately model the observed interactions. This research provides significant scientific and technological contributions in the following areas:

1. Characterization of the nucleation and dissolution kinetics of {311} defects in phosphorus doped silicon.
2. Correlation between extended defects and enhanced diffusion resulting from phosphorus implantation.
3. Identification of the conditions leading to {311} formation and PIC formation in phosphorus implanted silicon.
4. Measured electrical activation of implanted phosphorus.
5. Improvements of nonequilibrium dopant diffusion models used in TCAD simulators such as FLOOPS
6. Additional insight into the physical origin of the phosphorus kink concentration

Experimentation using phosphorus-doped wells showed that the presence of phosphorus has a significant effect on the nucleation of extended defects and their effect on enhanced diffusion. This was attributed to PICs. The temperature dependence of this effect showed that this effect centered about the phosphorus kink concentration. From this, an understanding of the changes in defect formation from direct phosphorus implants was achieved. It was shown that the formation of defects and PICs is strongly temperature dependent and their effect on diffusion can result in much different electrical activation and junction depths. Finally, TCAD models were developed based on the observed physics. Simulations utilizing these models showed strong improvement over those presently existing.

Conclusion

This research provides significant scientific contribution to the understanding of crystallographic defects and dopant diffusion after ion implantation as well as

technological advancement through improved continuum-based modeling of the diffusion process. Furthermore, this work confirms the importance of accounting for dopant-defect clustering during phosphorus diffusion simulations.

Areas of Further Study

Future research could extend the investigation to include amorphizing phosphorus implants and modeling clustering in the implant tail region beyond the amorphous-crystalline interface. This could be of practical importance during the use of low temperature recrystallization when making source / drain regions. Also, the experimental range of this study could be expanded to include lower energy implants and RTA anneals as this is when clustering is most likely to occur.

Ab-initio calculations of stable PIC cluster configurations and energetics would provide a tremendous benefit to the modeling the full kinetic path of PIC nucleation and dissolution. From this, it may also be possible to determine the exact relationship between the phosphorus kink concentration and the interstitials that induce PIC nucleation.

Furthermore, it is hoped that results from this research, in conjunction with research of other dopants, can be used towards establishing a unified understanding of the dopant / defect interactions and the significant influences upon cluster formation.

APPENDIX A
ARRHENIUS BEHAVIOR

Thermodynamics provides the information about which processes may occur, however, it gives no information about the rate of the process. The science that deals with reaction rates is kinetics. Thermally activated reactions often follow an *Arrhenius* behavior having an exponential dependence on the reciprocal temperature. An analytic equation describing this behavior was formulated by the Englishman J. Hood, and is named after the Swedish chemist Svante Arrhenius. The *Arrhenius equation* is as follows:

$$R(T) = R_0 \exp^{\left(-E_A/kT\right)} \qquad \text{(A1)}$$

In this equation, $R(T)$ is the rate constant at temperature T (˚K), R_0 is the frequency factor (sometimes referred to as the pre-exponential factor), k is the Boltzmann constant (8.617x10-5 eV/˚K), and E_A is the activation energy (in eV). These types of reactions are very common in the study of materials, making the above equation very useful for modeling a wide variety of chemical and physical processes.

Several features of the Arrhenius equation are important. First, note that k is a universal constant. Second, T represents the absolute temperature of the system, usually in degrees Kelvin (˚K). Third, the pre-exponential term R_0 and the activation energy E_A are constants that are characteristic of any individual reaction, but their values change as the reaction changes (i.e. they are not universal constants). Fourth, the activation energy can be thought of as the amount of energy that must be supplied to the system for the

reaction to proceed. Fifth, the reaction rate and the pre-exponential must have the same dimensional units. The values of R_0 and E_A can often be used to gain insight into the physical or chemical mechanisms that impact the reaction kinetics of the process being investigated.

If the temperature dependence of a reaction rate displays Arrhenius behavior, it is valid to extract values of R_0 and E_A from the measured reaction rate data. To verify that the reaction rates follow the Arrhenius relationship, the rate constant for a particular reaction is measured at several different temperatures. The log of the measured rate constant are plotted against $1000/T$ (10^3/°K) as shown in the Figure 70. If the measured rate constant values fall along a straight line on this plot, it can be concluded that the reaction obeys the Arrhenius relationship. Otherwise, a more complex reaction is taking place than that described by the Arrhenius equation.

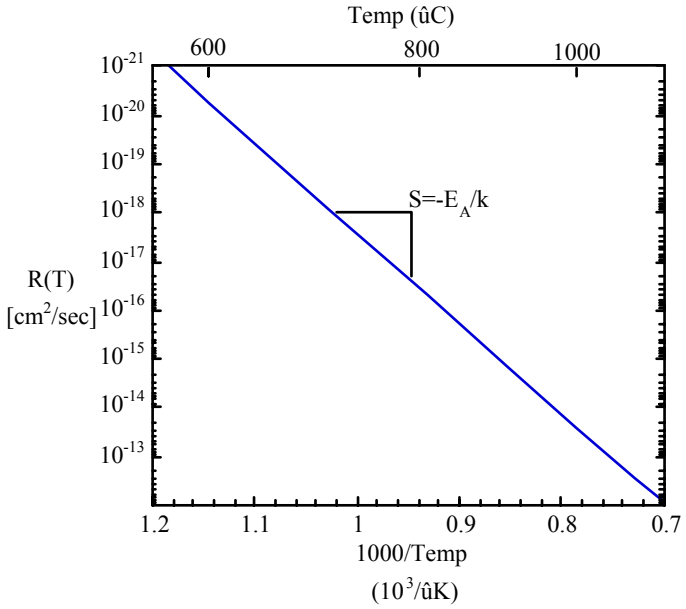

Figure 70. Example of Arrhenius temperature dependence.

The value of E_A can be extracted from the graphically determined slope of the plotted data, S=-E_A/k. The value of R_0 is then found by using this value of E_A, together with a value of $R(T)$ in the Arrhenius equation. A wider temperature range of data improves accuracy of the extracted values. Furthermore, if two processes display the same R_0 and E_A it is highly likely that they are attributable to the same reaction.

APPENDIX B
CHARACTERISTIC DIFFUSION DISTANCE

Gaussian curves can be used to analyze the diffusion enhancements observed in dopant marker layers. As an example, Figure 71 is a gaussian curve fit to the experimentally measured SIMS profile of a buried boron spike after near surface silicon implantation and annealing. The curve approximation is obtained using the gaussian formula

$$C(x) = \frac{Q}{\sqrt{\pi Dt}} e^{\frac{-(x-x_0)^2}{4Dt}} \qquad \text{(B1)}$$

where C is the concentration (cm^{-3}), Q is the dose (cm^{-2}), x is depth (cm), x_0 is the

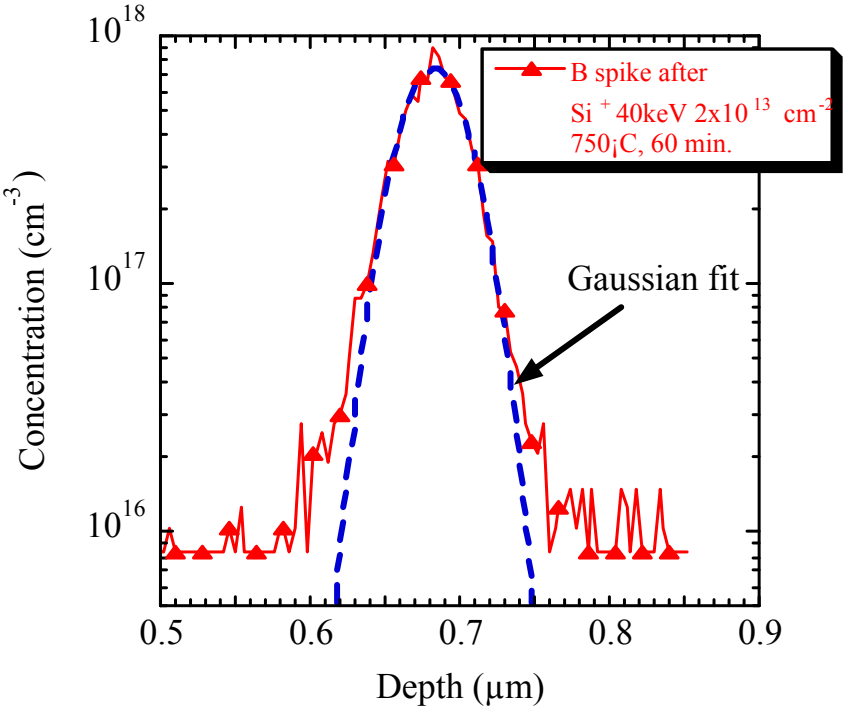

Figure 71. Gaussian curve fit to experimentally measured SIMS boron profile

centered depth (cm), and $\sqrt{Dt}$ is the characteristic diffusion distance (cm). The characteristic diffusion distance is a measure of the standard deviation of the gaussian. This is similar to a shift in junction depth.

From Figure 71 it is clear that the gaussian curve fits the experimental data relatively well. The fit accuracy has been determined to be within 95%, with broad profiles (longer anneal times) displaying better accuracy. After the SIMS profile is fit with a guassian, the extracted characteristic diffusion distance can be plotted as a function of time to observe the transient behavior.

LIST OF REFERENCES

Ang87 Angelucci, R., Cembali, F., Negrini, P., Servidori, M., & Solmi, S., J. Electrochem. Soc. 134, 3130 (1987).

Ant99 Antoniadis, D.A., Djomerhi, I.J., Jackson, K.M., & Miller, S., "Well-Tempered Bulk-Si NMOSFET Device Home Page (1999) {http://www-mtl.mit.edu:80/Well} accessed May, 2001.

Ash77 Ashburn, P., Bull, C., Nicholas, K.H., & Booker, G.R., Sol.-State Electr. 20, 731 (1977).

Bha97 Bharatan, S., Desroches, J., & Jones, K.S., in Materials and Process Characterization of Ion Implantation, (Ion Beam Press, Austin, 1997).

Boh13 Bohr, N., Phil. Mag. 25, 10 (1913).

Bou87 Bourret, A., Inst. of Physics Conf. Series 87, 39 (1987).

Bra94 Bracht, H., Stolwijk, N.A., & Mehrer, H., Mater. Sci. Forum 143-147, 785 (1994).

Bra95 Bracht, H. Stolwijk, N.A., & Mehrer, H., Phys. Rev. B 52, 16542 (1995).

Bri99 Brindos, R., Keys, P., Jones, K.S., & Law, M.E., Appl. Phys. Lett. 75, 229 (1999).

Buc72 Buck, T.M., Pickar, K.A., Poate, J.M., & Hsieh, C.M., Appl. Phys. Lett. 21, 485 (1972).

Bul79 Bull, C., Ashburn, P., Booker, G.R., & Nicholas, K.H., Sol.-State Electr. 22, 95 (1979).

Cat98 Caturla, M.J., Johnson, M.D., & de la Rubia, T.D., Appl. Phys. Lett. 72, 2736 (1998).

Cha96 Chao, H.S., Griffin, P.B., Plummer, J.D., & Rafferty, C.S., Appl. Phys. Lett. 69, 2113 (1996).

Cha00 Chau, R., Kavalieros, J., Roberds, B., Schenker, R., Lionberger, D., Barlage, D., Doyle, B., Arghavani, R., Murthy, A., & Dewey, G., Tech. Dig. Int. Electron Devices Meet. 00, (2001).

Cow90 Cowern, N.E.B., Janssen, K.T.F., & Jos, H.F.F., J. Appl. Phys. 68, 6191 (1990).

Cow94 Cowern, N.E.B., van de Walle, G.F.A., Zalm, P.C., & Vandenhout, D.W.E., Appl. Phys. Lett. 65, 2981 (1994).

Cow99 Cowern, N.E.B., Mannino, G., Stolk, P.A., Roozeboom, F., Huizing, H.G.A., & van Berkum, J.G.M., Phys. Rev. Lett. 82, 4460 (1999).

Cur00 Curie, M.P., Comptes Rendus 130, 76 (1900).

Dob71 Dobson, P.S., Phil. Mag. 24, 567 (1971).

Des97 Desroches, J.D., Master's Thesis, University of Florida, 1997.

Dun92 Dunham, S.T., J. Electrochem. Soc. 139, 2628 (1992).

Eag94 Eaglesham, D.J., Stolk, P.A., Gossmann, H.-J., & Poate, J.M., Appl. Phys. Lett. 65, 2305 (1994).

Eag95 Eaglesham, D.J., Stolk, P.A., Gossmann, H.-J., Haynes, T.E., & Poate, J.M., Nucl. Inst. & Meth. in Phys. Res. B 106, 191 (1995).

Fai77 Fair, R.B., & Tsai, C.C., J. Electrochem. Soc. 124, 1107 (1977).

Fai90 Fair, R.B., J. Electrochem. Soc. 137, 667 (1990).

Fra84 Frank, W., Gösele, U., Mehrer, & H., Seeger, A., in Diffusion in Crystalline Solids, (Academic Press, Orlando, 1984).

Gen97 Gencer, A.H. & Dunham, S.T., J. Appl. Phys. 81, 631 (1997).

Gil91 Giles, M.D., J. Electrochem. Soc. 138, 1160 (1991).

Gri93 Griffin, P.B., Lever, R.F., Huang, R.Y.S., Kennel, H.W., Packan, P.A., & Plummer, J.D., Tech. Dig.Int. Electron Devices Meet. 12, 295 (1993).

Gri95 Griffin, P.B., Crowder, S.W., & Knight, J.M., Appl. Phys. Lett. 67, 482 (1995).

Har83 Harris, R. M. & Antoniadis, D.A., Appl. Phys. Lett. 43, 937 (1983).

Hay96 Haynes, T.E., Eaglesham, D.J., Stolk, P.A., Gossmann, H.-J., Jacobson, D.C., & Poate, J.M., Appl. Phys. Lett. 69, 1376 (1996).

Hob99 Hobler, G. & Rafferty, C.S., Mat. Res. Soc. Symp. Proc. 568, 123 (1999).

Hu97 Hu, S.M., Mat. Sci. and Engr. R13, 105 (1997).

Jon88 Jones, K.S., Prussin, S., & Weber, E.R., Appl. Phys. A 45, 1 (1988).

Jon89 Jones, K.S., in The Encyclopedia of Advanced Materials, (Pergamon, 1989).

Kit76 Kittel, C., in Solid State Physics, 5th ed., pg. 100 (Wiley, New York, 1976).

Law96a Law, M.E., FLOOPS User's Manual, (University of Florida, Gainesville, FL, 1996).

Law96b Law, M.E. & Jones, K.S., Electrochem. Soc. Proc. 96-4, 374 (1996).

Len00 Lenosky, T.J., Sadigh, B., Theiss, S.K., Caturla, M.J., & de la Rubia, T.D., Appl. Phys. Lett. 77, 1834 (2000).

Li99 Li., J., Keys, P., Chen, J., Law, M.E., Jones, K.S., & Jasper, C., Mat. Res. Soc. Symp. Proc. 568, 175 (1999).

Lil97 Lilak, A.D., Earles, S.K., Jones, K.S., & Law, M.E., Tech. Dig.Int. Electron Devices Meet., 493 (1997).

Lin63 Lindhard, J., Scharff, M., & Schiott, H., Mat.-Fys. Med. Dan. Vid Selsk 33, 1 (1963).

Mas73 Masetti, G., Solmi, S., & Soncini, G., Solid-State Electron. 16, 1419 (1973).

Mas77 Masetti, G., Nobili, D., & Solmi, S., in Semiconductor Silicon 1977, pg. 647 (The Electrochemical Society Softbound Proceedings Series, Princeton, 1977).

Mat84 Mathiot, D. & Pfister, J.C., J. Appl. Phys. 55, 3518 (1984).

Mic89 Michel, A.E., Nucl. Inst. And Meth. in Phys. Res. B 37/38, 379 (1989).

Moo65 Moore, G.E., Electronics 38, 114 (1965).

Moo75 Moore, G.E., Tech. Dig. Int. Electron Devices Meet. 75, 11 (1975).

Mor54 Morin, F.J. & Maita, J.P., Phys. Rev. 96, 28 (1954).

Mor95 Morris, S.J., Yang, S.-H., Lim, D.H., Park, C., Klein, K.M., Manassian, M., & Tasch, A.F., IEEE Trans. Semicond. Manuf. 8, 408 (1995).

Nic89 Nichols, C.S., van de Walle, C.G., & Pantelides, S.T., Phys. Rev. B 40, 5484 (1989).

Nis86 Nishi, K. & Antoniadis, D.A., J. Appl. Phys. 59, 1117 (1986).

Nob82 Nobili, D., Armigliato, A., Finetti, M., & Solmi, S., J. Appl. Phys. 53, 1484 (1982).

Oeh84 Oehrlein, G.S., Cohen, S.A., & Sedgwick, T.O., Appl. Phys. Lett. 45, 417 (1984).

Ohl52 Ohl, R.S., Bell. Syst. Tech. J. 31, 104 (1952).

Pac90 Packan, P.A. & Plummer, J.D., Appl. Phys. Lett. 56, 1787 (1990).

Pac91 Packan, P.A., PhD Dissertation, Stanford University, 1991.

Pel97 Pelaz, L., Jaraiz, M., Gilmer, G.H., Gossmann, H.-J., Rafferty, C.S., Eaglesham, D.J., & Poate, J.M., Appl. Phys. Lett. 70, 2285 (1997).

Pel99 Pelaz, L., Gilmer, G.H., Gossmann, H.-J., & Rafferty, C.S., Appl. Phys. Lett. 74, 3657 (1999).

Raf96 Rafferty, C.S., Gilmer, G.H., Jaraiz, M., Eaglesham, D., & Gossmann, H.-J., Appl. Phys. Lett. 68, 2395 (1996).

Ram99 Raman, R., Law, M.E., Krishnamoorthy, V., & Jones, K.S., Appl. Phys. Lett. 74, 700 (1999).

Rut11 Rutherford, E., Phil. Mag. 21, 212 (1911).

Sal79 Salisbury, I.G. & Loretto, M.H., Phil. Mag. A, 39, 317 (1979).

Sat97 Sato, Y., Imai, K., & Yabumoto, N., J. Electrochem. Soc. 144, 2548 (1997).

Sat99 Sato, H., Yanagisawa, Y., Ogasawara, M., Kojima, H., Masuda, H., & Natsuaki, N., J. Electrochem. Soc. 146, 367 (1999).

Sch72 Schwettmann, F.N. & Kendall, D.L., Appl. Phys. Lett. 21, 2 (1972).

Sch99 Schroer, E. & Uematsu, M., Jpn. J. Appl. Phys. 38, 7 (1999).

Sho54 Shockley, W., Forming Semiconductor Devices by Ionic Bombardment (U.S. Patent 2,787,564 filed Oct. 28, 1954).

SIA00 S.I. Association, International Technology Roadmap for Semiconductors 2000 Update, Semiconductor Industry Association, San Jose, California, (2000) {http://www.public.itrs.net/} accessed May, 2001.

Sol98 Solmi, S. & Nobili, D., J. Appl. Phys. 83, 2484 (1998).

Sto95 Stolk, P.A., Gossmann, H.-J., Eaglesham, D.J., Jacobson, D.C., Luftman, H.S., & Poate, J.M., Mat. Res. Soc. Symp. Proc. 354, 307 (1995).

Sto97 Stolk, P.A., Gossmann, H.-J., Eaglesham, D.J., Jacobson, D.C., & Poate, J.M., J. Appl. Phys. 81, 6031 (1997).

Tak91 Takeda, S., Jpn. J. Appl. Phys. 30, L639 (1991).

Tam73 Tamura, M., Appl. Phys. Lett. 23, 651 (1973).

Tan81 Tan, T.Y., Phil. Mag. A 44, 101 (1981).

Tan85 Tan, T.Y. & Gösele, U., Appl. Phys. A 37, 1 (1985).

Tan99 Taniguchi, K., Saito, T., Xia, J., Kim, R., Aoki, T., Kobayashi, H., & Kamakura, Y., Mat. Res. Soc. Symp. Proc. 568, 155 (1999).

Tas89 Tasch, A.F., Park, C., Alvis, J., & Novak, S., J. Electrochem. Soc. 136, 810 (1989).

Tho12 Thompson, J.J., Phil. Mag. 6-23, 449 (1912).

Uem97 Uematsu, M., J. Appl. Phys. 82, 2228 (1997).

Uem98 Uematsu, M., J. Appl. Phys. 84, 4781 (1998).

Uem99 Uematsu, M., Jpn. J. Appl. Phys., 38, 6188 (1999).

Wat97 Watkins, G.D., Mat. Res. Soc. Symp. Proc. 469, 139 (1997).

Web69 Webber, R.F., Thorn, R.S., & Large, L.N., Int. J. of Electronics 26, 163 (1969).

Yos79 Yoshida, M., Jpn. J. Appl. Phys. 18, 479 (1979).

Zha95 Zhang, L.H., Jones, K.S., Chi, P.H., & Simmons, D.S., Appl. Phys. Lett. 67, 2025 (1995).

Zhu97 Zhu, J., Mat. Res. Soc. Symp. Proc. 469, 151 (1997).

BIOGRAPHICAL SKETCH

Patrick Keys was born in Ridgewood, NJ, on September 16, 1971. He received the B.S. degree in electronics engineering from the University of Scranton, PA, in 1993. He worked as a Product Safety Engineer for Sharp Electronics Corporation from 1993 to 1997 while continuing to pursue his graduate education. He received the M.S. degree in engineering sciences, specializing in electronic materials from New Jersey Institute of Technology, NJ, in 1997. Since returning to graduate school full-time in August, 1997, at the University of Florida, he has been working towards his Ph.D. degree in materials science and engineering, specializing in dopant-defect interactions resulting from ion implantation processing of semiconductors. During this time, he has interned at Lucent Technologies-Bell Labs, and Intel Corporation-TCAD Dept. His research interests include silicon process experimentation, modeling, and integration with emphasis on advanced process and device development. He is a member of the Institute of Electrical and Electronics Engineers (IEEE) and the Materials Research Society (MRS). On a good day, he can be found on the water drifting flies and setting hooks.

I certify that I have read this study and that in my opinion it conforms to acceptable standards of scholarly presentation and is fully adequate, in scope and quality, as a dissertation for the degree of Doctor of Philosophy.

_____

Kevin S. Jones, Chairman
Professor of Materials Science and Engineering

I certify that I have read this study and that in my opinion it conforms to acceptable standards of scholarly presentation and is fully adequate, in scope and quality, as a dissertation for the degree of Doctor of Philosophy.

_____

Mark E. Law, Cochairman
Professor of Electrical and Computer Engineering

I certify that I have read this study and that in my opinion it conforms to acceptable standards of scholarly presentation and is fully adequate, in scope and quality, as a dissertation for the degree of Doctor of Philosophy.

_____

Cammy R. Abernathy
Professor of Materials Science and Engineering

I certify that I have read this study and that in my opinion it conforms to acceptable standards of scholarly presentation and is fully adequate, in scope and quality, as a dissertation for the degree of Doctor of Philosophy.

_____

Robert T. DeHoff
Professor of Materials Science and Engineering

I certify that I have read this study and that in my opinion it conforms to acceptable standards of scholarly presentation and is fully adequate, in scope and quality, as a dissertation for the degree of Doctor of Philosophy.

_____

Toshikazu Nishida
Associate Professor of Electrical and Computer Engineering

This dissertation was submitted to the Graduate Faculty of the College of Engineering and to the Graduate School and was accepted as partial fulfillment of the requirements for the degree of Doctor of Philosophy.

May, 2001

_____

M. J. Ohanian
Dean, College of Engineering

_____

Winfred M. Phillips
Dean, Graduate School